NONEQUILIBRIUM HIDDEN STATES IN QUANTUM MATERIALS INVESTIGATED BY ULTRAFAST ELECTRON DIFFRACTION AND MICROSCOPY

By

Xiaoyi Sun

A DISSERTATION

Submitted to
Michigan State University
in partial fulfillment of the requirements
for the degree of

Physics – Doctor of Philosophy

2024

ABSTRACT

NONEQUILIBRIUM HIDDEN STATES IN QUANTUM MATERIALS INVESTIGATED BY ULTRAFAST ELECTRON DIFFRACTION AND MICROSCOPY

By

Xiaoyi Sun

This dissertation investigates the nonequilibrium physics of VO_2 phase transition using a dual-probe approach combining ultrafast electron diffraction (UED) and ultrafast optical differential transmittance measurements, enabled by advancements in RF compression techniques for ultrafast electron microscopy and diffraction. By simultaneously tracking the structural and electronic responses with enhanced momentum resolution, this work provides new insights into the cooperativity and competing mechanisms underlying the photoinduced phase transition (PIPT) in VO_2.

The development of a cascade RF control system, featuring a two-level PID feedback loop, significantly reduces noise and instabilities in the RF system. The experimental validation of this upgraded RF system demonstrates a temporal resolution of ≈50 fs (FWHM) and a spatial resolution of 10 femtometers, pushing the limits of ultrafast electron probe technology.

Leveraging these advancements, the dual-probe measurements reveal a multi-threshold nonequilibrium phenomenology in VO_2 that deviates from the behavior of thermally-induced phase transitions. A critical fluence threshold $Fc \approx 4.5$ mJ/cm^2 is identified for ultrafast insulator-to-metal transition (IMT) mediated by polaron formation localized to the V-V sublattice, establishing a transient monoclinic metallic (*mM*) state. This ultrafast IMT pathway is distinct from the thermally driven process and unaffected by lattice strain, indicating a different organizing principle at the initial stage.

However, at longer timescales, the system converges back to the thermal phases governed

by strong electron-phonon coupling, where IMT and structural phase transition (SPT) remain tightly coupled. The dual-probe measurements, supported by an effective medium theory, disentangle the competing effects of photoexcitation, polaron formation, and metallic domain growth, providing a unified picture connecting the nonequilibrium and equilibrium regimes. These findings advance the understanding of PIPT in VO_2 and highlight the power of combining UED and ultrafast optical probes for unraveling complex phase transition dynamics in strongly correlated materials.

To my wife, parents, and our eagerly awaited daughter

ACKNOWLEDGEMENTS

First and foremost, I would like to express my deepest gratitude to my advisor, Prof. Chong-Yu Ruan, for his unwavering support, boundless patience, and invaluable guidance throughout my doctoral journey. His mentorship has been instrumental in shaping my research skills and scientific perspective. Prof. Ruan's availability, even during the most challenging times, and his willingness to discuss ideas and provide constructive feedback have been crucial to my growth as a researcher. His dedication to his students' success and his passion for science have been truly inspiring. I am forever grateful for the opportunity to learn from and work with such an exceptional mentor.

I am incredibly thankful to Dr. Shuaishuai Sun for teaching me electron optics and to Joe Williams for his guidance in RF. Their expertise and willingness to share their knowledge have been vital to my growth as a researcher.

I would also like to extend my appreciation to my colleagues who I worked closely with: Dr. Yingjing Li, Faran Zhou, Daniel Bartles, Elliot Wozniak, Dr. Ming Zhang, Jacob Rancour, Himanshi, and Dr. Sachin Sharma. Their collaboration, insightful discussions, and camaraderie have made my time in the lab an enriching and enjoyable experience. I also thank my other teammates: Noah Chavez, Nandhalalan Saravanan, Yousuf Alishan, Sead Demirovic, and Alexander George for their support and friendship.

I would like to express my sincere gratitude to my committee members: Prof. Nelson Sepúlveda Alancastro, Prof. Tyler Cocker, Prof. Xianglin Ke, and Prof. Phillip Duxbury for their valuable insights and constructive feedback throughout my research. I also extend my thanks to Dr. Reza Lolloee, Dr. Baokang Bi, Dr. Xudong Fan, and Barry Tigner for their assistance, expertise, and support throughout my research. I am also grateful to the machine shop team: Tom Palazzolo, Tom Hudosn, Jim Muns, Rob Bennett, and Mike Schoen for their skilled craftsmanship and

support in building essential components for my experiments. I am thankful to the secretaries, Cathy Cords, Jessica Cords, and Kim Crosslan, for their administrative support and ensuring smooth operations in the department.

I would like to acknowledge the collaborative efforts of Prof. Peter Ostroumov, Dr. Dan Morris, Dr. Shen Zhao, and Shriraj Kunjir in building the RF control loop. Their contributions have been crucial to improving the resolution of the system I worked on. I appreciate the UEM beamline calculations performed by Prof. Phillip Duxbury, Dr. Brandon Zerbe, and Xukun Xiang. Their work has provided valuable insights for my research.

I am grateful for the collaborations on the VO_2 project, including the real-time time-dependent density functional theory calculations by Prof. Meng Sheng, sample preparation and temperature dependent measurements by Prof. Nelson Sepúlveda Alancastro, Ian Gonzalezafanador, and Gerardo Morales Torres, and the hole doping structure calculated by Prof. Bin Wang and Tien Li. I also thank Prof. Kai Rossnagel and Florian K. Diekmann for providing the $TaSe_2$ sample.

I would also like to acknowledge the contributions of Prof. Peng Zhang in plasma physics, Prof. Mohammad Maghrebi for his insights on phase transitions, and Prof. Mercouri Kanatzidis, Dr. Christos Malliakas, and Jin-Ke Bao for providing the TaS_2 and $CeTe_3$ samples.

I would like to express my heartfelt gratitude to my friends: Boyao Zhu, Huan Qi, Kairui Sun, Kang Yu, Shuyue Xue, Tianxudong Tang, Xinda Qi, Zhen Li, Zhite Yu, Zhouyou Fan, and many others for their unwavering support and encouragement throughout this journey. I am especially grateful to my dear friend Zhen Li, who has always been by my side, offering constant support and inspiration.

To my beloved family, my wife, our unborn daughter, and my parents, I am forever grateful for your unconditional love, patience, and unwavering support. Your presence in my life has been a constant source of strength and motivation. Without your support and encouragement, this achievement would not have been possible.

Xiaoyi Sun
孙潇逸
East Lansing, MI
2024

TABLE OF CONTENTS

LIST OF TABLES

LIST OF FIGURES

Chapter 1

Strongly Correlated Materials

Traditional band theory, rooted in the independent electron approximation typically referred to as single-electron picture, has served as a foundational framework for understanding the electronic structure and properties of solids. However, it encounters significant limitations when applied to strongly correlated materials[1], in which the interactions between electrons play a crucial role. In these materials, the electrons can no longer be treated as effectively non-interacting, and their behavior is substantially influenced by the presence of other electrons in the system. This strong correlation gives rise to intriguing phenomena, such as metal-insulator transitions, high-temperature superconductivity, and colossal magnetoresistance. To adequately describe the properties of strongly correlated materials, it is necessary to employ advanced theoretical tools, such as many-body techniques[2–4], which can properly account for the effects of electron-electron interactions.

A captivating phenomenon in strongly correlated materials is the occurrence of photo-induced phase transitions (PIPT), in which the absorption of photons by a material can trigger an avalanche of changes in its electronic or structural properties. These transitions often start at the ultrafast timescales and provide a means to study the dynamics of strongly correlated systems. Photo-induced phase transitions offer a unique opportunity to control the properties of strongly correlated materials using light and to investigate the interplays between electronic and structural degrees of freedom in these systems.

This chapter aims to provide a foundational review of the key concepts and phenomena related to strongly correlated materials, quantum phase transitions, and photo-induced phase

transitions. By establishing a good understanding of these topics, we set the stage for the case study of a specific strongly correlated material that will be presented in the subsequent chapters.

1.1 Single Electron Band Theory: Successes and Limitations

Band theory based on the independent electron approximation has long been a fundamental framework for understanding the electronic structure and properties of solids[5]. Here, electrons are treated as non-interacting particles moving in a periodic potential created by the atomic lattice. By solving the Schrödinger equation under these assumptions, one obtains energy bands that describe the allowed energy states for electrons in the solid. The electronic properties of the material, such as electrical conductivity and optical absorption, are determined by the characteristics of these energy bands, including their shape, width, and the presence of band gaps.

The single electron picture band theory has demonstrated remarkable success in explaining the behavior of a wide range of materials, particularly semiconductors and simple metals[67]. For instance, it accurately predicts the existence of band gaps in semiconductors, which are essential for their electronic properties. The size of the band gap determines whether a material is an insulator, a semiconductor, or a conductor. In semiconductors like silicon and germanium, the band gap is on the order of 1 eV, allowing for the control of electrical conductivity through doping and the creation of electronic devices such as diodes and transistors. Moreover, it also successfully describes the electronic structure of simple metals, such as alkali metals (e.g., sodium and potassium) and noble metals (e.g., copper and silver). In these materials, the conduction band is partially filled, leading to their high electrical conductivity.

However, despite its numerous successes, single-electron band theory encounters significant limitations when applied to strongly correlated materials[7–9]. In these materials, the interactions between electrons are so strong that the independent electron approximation breaks down. The behavior of electrons in strongly correlated materials is heavily influenced by the presence of other electrons in the system, leading to complex many-body phenomena that cannot be adequately described by single electron picture.

One prominent example of the limitations of single-electron band theory in strongly correlated materials is the case of transition metal oxides, such as nickel oxide (NiO)[9]. According to band theory, these materials should exhibit metallic behavior due to the partially filled d-bands of the transition metal ions. However, experimental observations reveal that they are insulators. This discrepancy arises from the strong Coulomb repulsion between electrons in the d-orbitals, which leads to the formation of a Mott insulating state. In this case, the calculation of electron bands must include the correlation effect by adding a “Hubbard Potential” term to considering the strong electron-electron correlation[10], where the independent electron approximation fails to capture.

Another example of the limitations of band theory is the case of heavy fermion materials[11], such as $CeCoIn_5$[12] and UPt_3[13]. These materials exhibit large effective electron masses, up to several hundred times the mass of a free electron, which cannot be explained by the band theory with independent electron approximation. The heavy fermion behavior arises from the interaction between the localized f-electrons and the conduction electrons, leading to the formation of a strongly correlated electron system. Treating electrons as independent particles fails to account for these complex interactions and the resulting heavy fermion properties.

Furthermore, the single-particle picture also fails to describe the phenomenon of high-temperature superconductivity, which is observed in certain strongly correlated materials, such as cuprates[14,15] (e.g., $YBa_2Cu_3O_7$) and iron-based superconductors[16] (e.g., LaFeAsO). In these materials, the superconducting transition temperature is much higher than what can be explained by conventional BCS theory, which is based on the electron-phonon interaction. The high-temperature superconductivity is believed to originate from strong electron-electron correlations[17], which are not captured by the independent electron approximation.

To accurately describe the behavior of strongly correlated materials, it is necessary to go beyond the independent electron approximation and employ advanced theoretical tools that can properly account for the complex many-body phenomena arising from electron correlations. These tools include the Hubbard model[18,19], dynamical mean-field theory (DMFT)[20], and the GW approximation[21], among others. By incorporating the effects of electron-electron interactions, these methods provide a more comprehensive understanding of the electronic structure and properties of strongly correlated materials, enabling the exploration of the exotic phenomena.

1.2 Photoinduced Emergent Phenomena in Strongly Correlated Materials

In the preceding section, we examined the advantages and shortcomings of single-electron band theory in characterizing the electronic structure and properties of materials, specifically in the realm of strongly correlated systems. With this groundwork laid, we now direct our attention to the phenomenon of photoinduced phase transitions and the revelation of hidden states within strongly correlated materials. The investigation of these transitions, initiated by ultrafast laser

pulses, affords unique opportunities to delve into the nonequilibrium dynamics and intricate energy landscape of these complex systems.

The laser's influence can be interpreted from two interconnected perspectives: on a local scale, the laser instigates photodoping[22–25] by promoting electrons from the valence band to the conduction band, leaving in its wake a sea of holes; on a global scale, the ultrafast nature of the laser pulse serves as a quench[26–29], reshaping the energy landscape of the system. These two effects, far from being distinct, are instead interwoven facets of the same overarching phenomenon. The photodoping process modifies the local electronic structure, while the ultrafast quench propels the system out of equilibrium, granting it the freedom to navigate previously unexplored regions of the phase space and unveil hidden states.

In the forthcoming sections of this chapter, we will give overview select paradigmatic examples that exemplify the potency of photoinduced phase transitions in uncovering hidden states within strongly correlated materials. Through examination of these case studies, this chapter aims to elucidate the tapestry of phenomena that can be accessed via the interplay of photodoping and ultrafast quenches, underscoring the potential of this approach in unraveling the multifaceted physics of strongly correlated systems under nonequilibrium conditions.

1.2.1 Laser Induced Metastable Hidden Quantum State

Transition metal dichalcogenides[30] (TMDCs) are a class of two-dimensional materials that have garnered significant attention in recent years due to their unique electronic, optical, and mechanical properties. TMDCs consist of a transition metal layer sandwiched between two layers of chalcogen atoms, forming a layered structure held together by weak van der Waals forces.

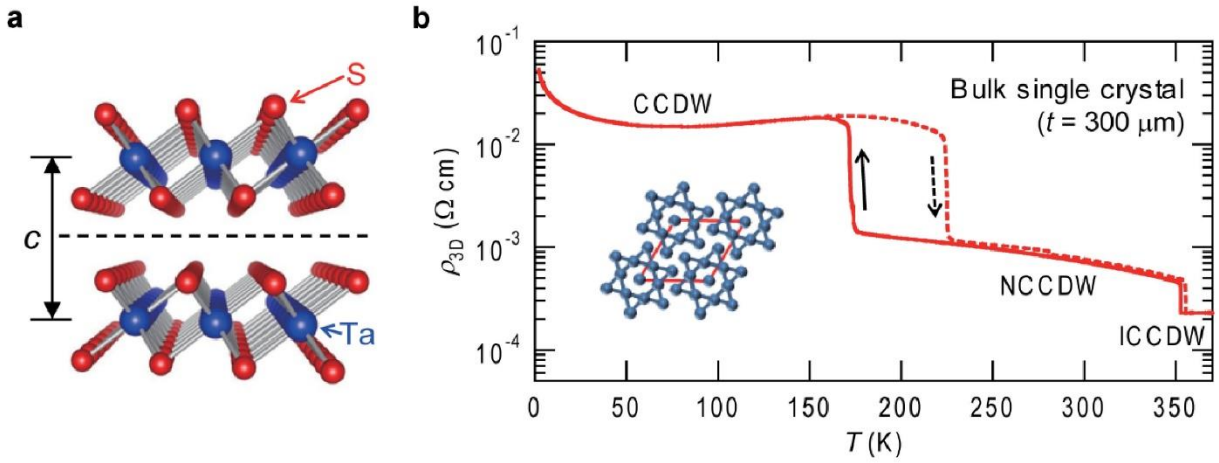

Figure 1.1. Property of 1T-TaS_2. a. Structure of 1T-TaS_2. **b.** The Resistivity change of TaS_2 across different CDW state. Adapted from Ref[31].

One prominent example is the 1T polymorph of tantalum disulfide (1T-TaS_2)[32], which undergoes a series of charge density wave (CDW) transitions as the temperature is varied[33]. At low temperatures, 1T-TaS_2 exists in a commensurate CDW (CCDW) state, where the CDW period locks into a specific ratio with the underlying lattice. Concurrently, 1T-TaS_2 becomes a Mott insulator, with strong electron-electron interactions leading to the localization of electrons and the opening of a Mott gap in the electronic structure. As the temperature increases, the material transitions to a nearly commensurate CDW (NCCDW) state. Upon further increasing the temperature to approximately 353 K, 1T-TaS_2 undergoes another phase transition to an incommensurate CDW (ICCDW) state. In this state, the CDW period no longer maintains a simple rational relationship with the lattice periodicity. Finally, when the temperature is raised above 543 K, the CDW order in 1T-TaS_2 melts completely, and the material returns to a normal metallic state without any periodic modulation of the electron density or lattice distortion. The

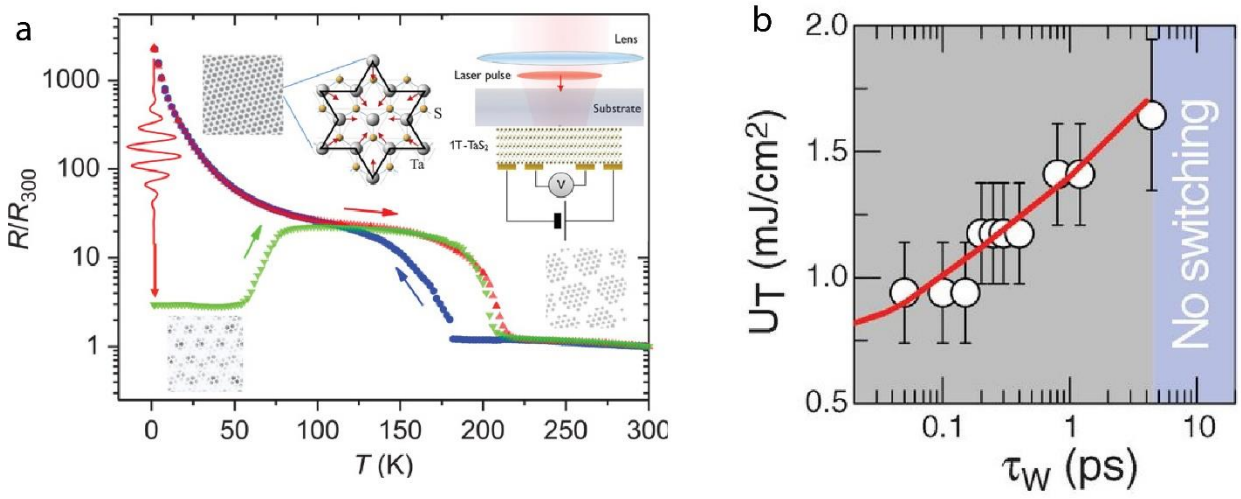

Figure. 1.2. Hidden state of 1T-TaS_2 after photoexcitation. a. The unperturbed resistance is shown in the C state on cooling (blue data points) and on heating (red data points). The green curve shows the resistance in the H state after switching by a single 35-fs optical pulse above threshold. A schematic representation of the ordered phases C and NC is shown, with an indicated tentative ordering for the H state. The inset shows a schematic description of the experimental setup. **b.** Switching threshold fluence as a function of pulse length measured. Panel **a** adapted from Ref [31], panel **b** adapted from Ref[23].

structure of 1T-TaS_2 is shown in Fig. 1a. The resistivity change across different CDW states is shown in Fig. 1b.

Stojchevska et al. excited the 1T-TaS_2 system at 1.5 K with a single pulse of 800 nm, 35 fs laser at a fluence of 1 mJ/cm^2. They found that the supposed Mott insulator state was driven into a hidden state with resistance near the NCCDW state[23]. Surprisingly, this hidden state is long-lived, and no observable decay has been observed, with the lifetime expected to be beyond days[31,34,35]. Upon further heating the sample, the resistivity curve merged with the 1T-TaS_2 resistivity curve at around 50 K, and the hidden state was thus erased. The system can return to the normal CCDW state upon cooling again. This process can only be triggered by an ultrafast laser pulse, and as the pulse width of the laser increases, the required fluence threshold increases accordingly, further indicating that the process is driven by the photodoping effect.

1.2.2 Laser Induced Spontaneous Symmetry Breaking into a Hidden Charge-Density Wave State

Rare-earth tellurides (RTe_3)[36] are a class of materials that provide an opportunity to investigate the interplay between electronic structure and electron-electron interactions in low-dimensional systems. These compounds possess a quasi-two-dimensional layered structure, which results in highly anisotropic electronic properties. The reduced dimensionality amplifies the effect of electron-electron coupling, leading to the manifestation of various phenomena, such as CDWs and unconventional superconductivity. The RTe_3 family has a slightly orthorhombic crystal structure, such that the a and c axes are not equivalent. The CDWs are formed in the R-Te layers, and for light rare-earth elements, only one CDW is observed along the c axis[37,38]. For heavier elements, the CDWs are observed to be bidirectional. The phase diagram is given in Fig. 3b.

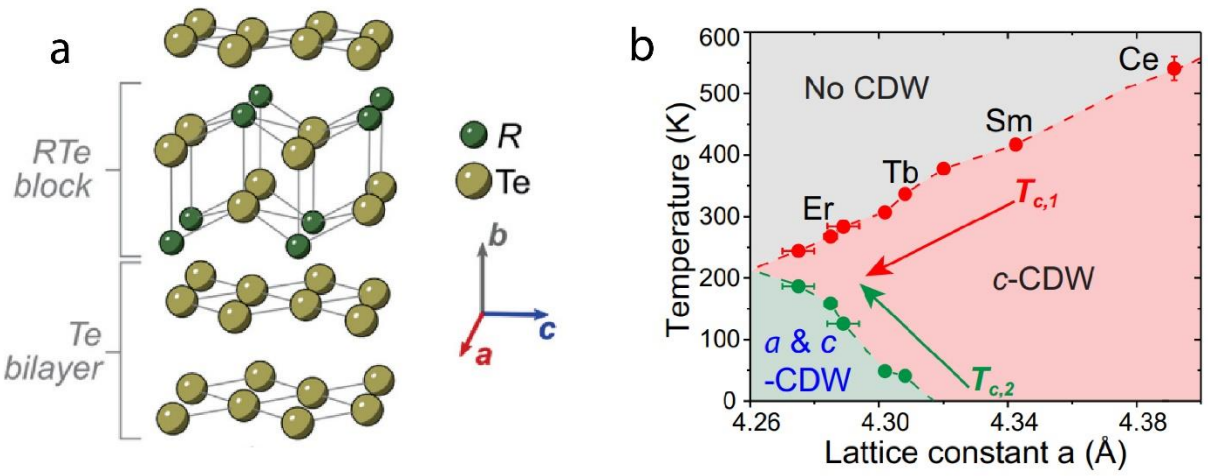

Figure 1.3. Property of RTe_3. a. Crystal and electronic structure of RTe_3, consists of RTe block and Te bilayer. **b.** The phase diagram of RTe_3. Panel **a** adapted from Ref[38], panel **b** adapted from Ref[29]

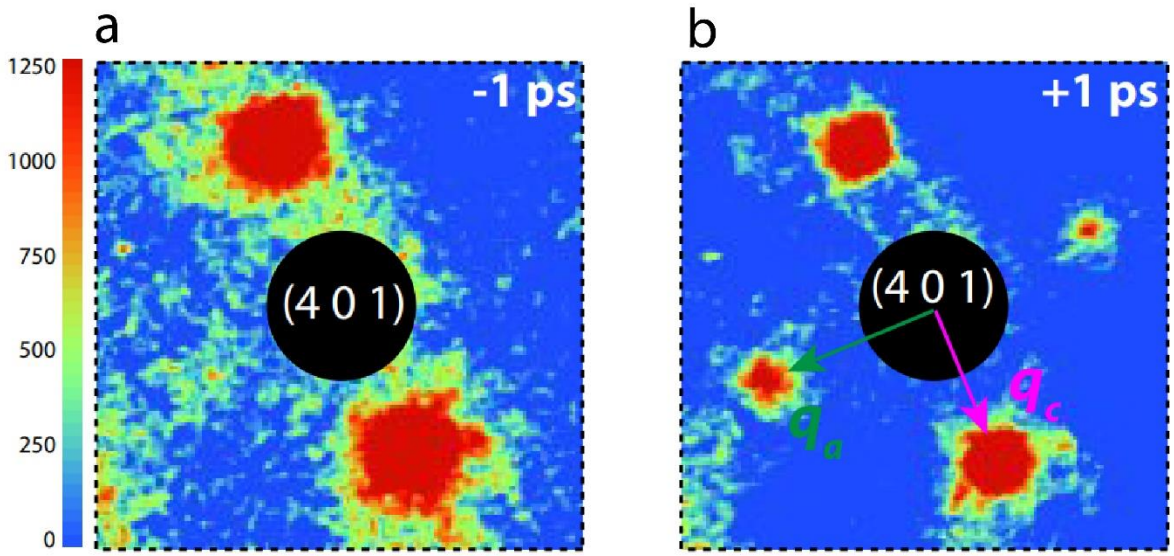

Figure 1.4. Emergency of a-CDW after photoexcitation. a. Diffraction pattern gathered before laser excitation, CDW order only observed in c direction. **b.** Diffraction pattern gathered 1ps after excitation, the CDW order is shown up in a direction too. Adapted from Ref[29]

Zhou et al. performed experiments using femtosecond near-infrared pulses to excite $CeTe_3$[29]. Under equilibrium conditions, $CeTe_3$ only exhibits a CDW along the c direction (c-CDW). However, after excitation, Zhou et al. observed the generation of a CDW along the a direction (a-CDW), which, according to the trend from the phase diagram, would require temperatures below 0 K to access this state under equilibrium conditions. Interestingly, the generation of the a-CDW does not require a full suppression of the c-CDW. The authors argue that the quench from the laser pulse accentuates the intrinsic bidirectional competitive energy landscape that governs both the thermal and nonthermal phase transitions.

1.2.3 Light-Induced Superconductivity

Cuprate superconductors[39] are a family of high-temperature superconducting materials made by doping the parent compound, an antiferromagnetic Mott insulator, with layers of copper oxides (CuO_2) alternating with layers of other metal oxides. At ambient pressure, the cuprate superconductor mercury barium calcium copper oxide ($HgBa_2Ca_2Cu_3O_8$) holds the highest known critical temperature at 133 K[40]. Although the exact mechanism for the superconducting state is still unknown, various experiments have confirmed that the pairing electrons are d-orbital electrons[41], leading to speculation that strong electronic correlations play a pivotal role in the superconductivity of cuprates.

An example of a parent compound is La_2CuO_4, which becomes superconducting when holes are doped by replacing La with Ba or Sr. Fausti et al. studied a photo-excited variation of Sr-doped La_2CuO_4 with the chemical formula $La_{1.675}Eu_{0.2}Sr_{0.125}CuO_4$ ($LESCO_{1/8}$)[42]. They set the base temperature of $LESCO_{1/8}$ to 10 K, at which the system is non-superconducting. They then excited the system with a 15 μm ultrafast laser pulse. After laser excitation, a plasma edge at 60

cm^{-1} was observed in the change of c-axis reflectivity, which is missing in the unexcited system. The plasma edge at 60 cm^{-1} is a characteristic of superconductivity in a similar system, $LSCO_{0.16}$. From this, the authors concluded that $LESCO_{1/8}$ as excited to a transient photoinduced superconducting state, similar to $LSCO_{0.16}$ in the low-temperature superconducting state. The reflectivity measurement is plotted in Fig. 3

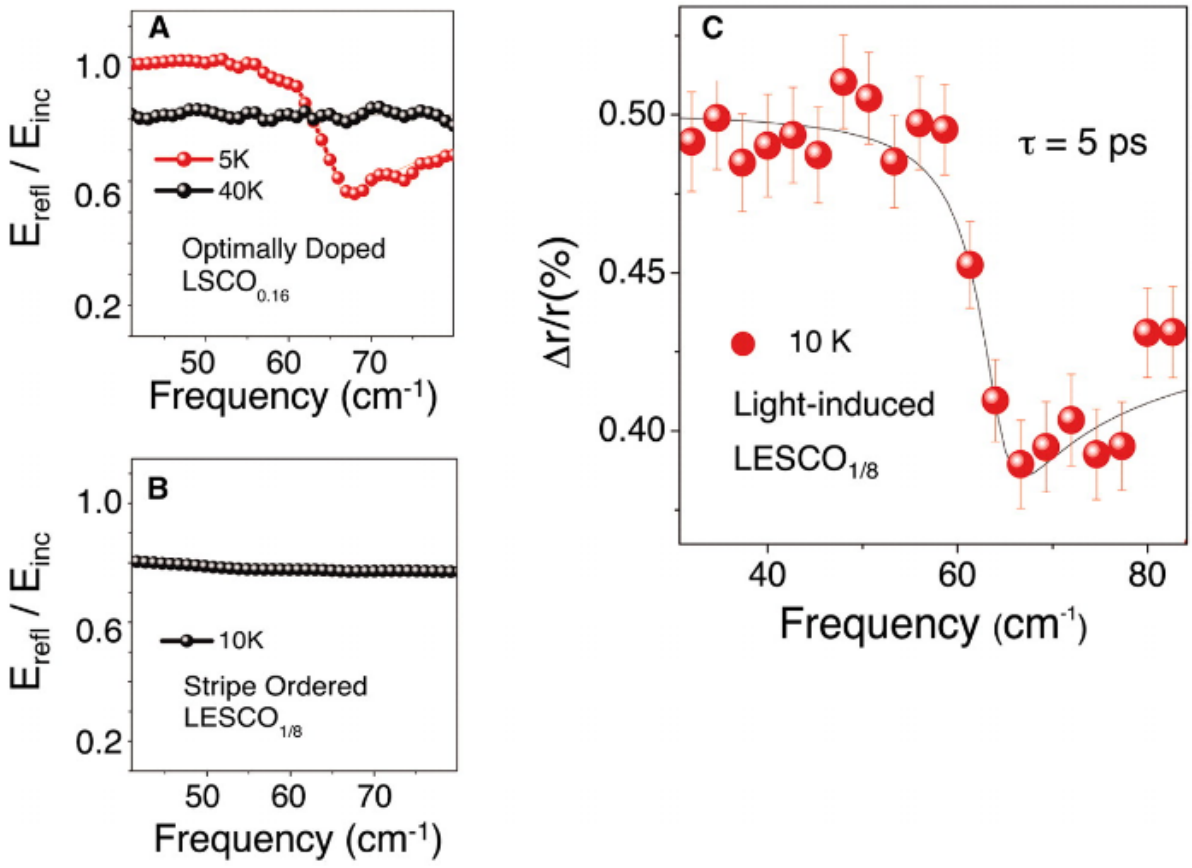

Figure 1.5. Light induced superconductivity of $LSCO_{0.16}$. a. Static c-axis electric field reflectance ($r = E_{refl}/E_{inc}$) of $LSCO_{0.16}$, measured at a 45° angle of incidence above (black dots) and below (red dots) Tc = 38 K. In the equilibrium low-temperature superconducting state, a Josephson plasma edge is clearly visible, reflecting the appearance of coherent transport. **b.** Static c-axis reflectance of $LESCO_{1/8}$ at 10 K. The optical properties are those of a no superconducting compound down to the lowest temperatures. **c.** Transient c-axis reflectance of LESCO1/8. Measurements are taken at 10 K, after excitation with IR pulses at 16 μm wavelength. The appearance of a plasma edge at 60 cm^{-1} demonstrates that the photoinduced state is superconducting. Adapted from Ref[42]

REFERENCES

REFERENCES

[1] G. Kotliar, and D. Vollhardt, “Strongly Correlated Materials: Insights From Dynamical Mean-Field Theory,” Phys Today **57**(3), 53–59 (2004).

[2] J. Harl, and G. Kresse, “Accurate Bulk Properties from Approximate Many-Body Techniques,” Phys Rev Lett **103**(5), 56401 (2009).

[3] D.S. Chemla, and J. Shah, “Many-body and correlation effects in semiconductors,” Nature **411**(6837), 549–557 (2001).

[4] E. Morosan, D. Natelson, A.H. Nevidomskyy, and Q. Si, “Strongly Correlated Materials,” Advanced Materials **24**(36), 4896–4923 (2012).

[5] N.W. Ashcroft, and N.D. Mermin, “Solid State Physics,” Thomson Learning Inc, (1976).

[6] J. Singleton, *Band Theory and Electronic Properties of Solids* (OUP Oxford, 2001).

[7] C. Kittel, and P. McEuen, *Introduction to Solid State Physics* (John Wiley & Sons, 2018).

[8] E. Dagotto, and Y. Tokura, “Strongly correlated electronic materials: present and future,” MRS Bull **33**(11), 1037–1045 (2008).

[9] N.F. Mott, “Metal-insulator transitions,” Contemp Phys **14**(5), 401–413 (1973).

[10] M. Imada, A. Fujimori, and Y. Tokura, “Metal-insulator transitions,” Rev Mod Phys **70**(4), 1039 (1998).

[11] S.G.R. Stewart, “Heavy-fermion systems,” Rev Mod Phys **56**(4), 755 (1984).

[12] C. Petrovic, P.G. Pagliuso, M.F. Hundley, R. Movshovich, J.L. Sarrao, J.D. Thompson, Z. Fisk, and P. Monthoux, “Heavy-fermion superconductivity in CeCoIn5 at 2.3 K,” Journal of Physics: Condensed Matter **13**(17), L337 (2001).

[13] L. Taillefer, and G.G. Lonzarich, “Heavy-fermion quasiparticles in UPt 3,” Phys Rev Lett **60**(15), 1570 (1988).

[14] N.P. Armitage, P. Fournier, and R.L. Greene, “Progress and perspectives on electron-doped cuprates,” Rev Mod Phys **82**(3), 2421 (2010).

[15] S. Chakravarty, R.B. Laughlin, D.K. Morr, and C. Nayak, “Hidden order in the cuprates,” Phys Rev B **63**(9), 094503 (2001).

[16] A. V Chubukov, D. V Efremov, and I. Eremin, “Magnetism, superconductivity, and pairing symmetry in iron-based superconductors,” Phys Rev B **78**(13), 134512 (2008).

[17] M. Capone, M. Fabrizio, C. Castellani, and E. Tosatti, “Strongly correlated superconductivity,” Science (1979) **296**(5577), 2364–2366 (2002).

[18] J. Hubbard, “Electron correlations in narrow energy bands,” Proc R Soc Lond A Math Phys Sci **276**(1365), 238–257 (1963).

[19] P.W. Anderson, “New approach to the theory of superexchange interactions,” Physical Review **115**(1), 2 (1959).

[20] A. Georges, G. Kotliar, W. Krauth, and M.J. Rozenberg, “Dynamical mean-field theory of strongly correlated fermion systems and the limit of infinite dimensions,” Rev Mod Phys **68**(1), 13 (1996).

[21] F. Aryasetiawan, and O. Gunnarsson, “The GW method,” Reports on Progress in Physics **61**(3), 237 (1998).

[22] C. Kübler, H. Ehrke, R. Huber, R. Lopez, A. Halabica, R.F. Haglund, and A. Leitenstorfer, “Coherent Structural Dynamics and Electronic Correlations during an Ultrafast Insulator-to-Metal Phase Transition in ${\mathrm{VO}}_{2}$,” Phys Rev Lett **99**(11), 116401 (2007).

[23] L. Stojchevska, I. Vaskivskyi, T. Mertelj, P. Kusar, D. Svetin, S. Brazovskii, and D. Mihailovic, “Ultrafast Switching to a Stable Hidden Quantum State in an Electronic Crystal,” Science (1979) **344**(6180), 177–180 (2014).

[24] A. Cavalleri, Th. Dekorsy, H.H.W. Chong, J.C. Kieffer, and R.W. Schoenlein, “Evidence for a structurally-driven insulator-to-metal transition in ${\mathrm{VO}}_{2}$: A view from the ultrafast timescale,” Phys Rev B **70**(16), 161102 (2004).

[25] Z. Tao, F. Zhou, T.R.T. Han, D. Torres, T. Wang, N. Sepulveda, K. Chang, M. Young, R.R. Lunt, and C.Y. Ruan, “The nature of photoinduced phase transition and metastable states in vanadium dioxide,” Sci Rep **6**, (2016).

[26] G.-J. Zhao, and K.-L. Han, “Ultrafast hydrogen bond strengthening of the photoexcited fluorenone in alcohols for facilitating the fluorescence quenching,” J Phys Chem A **111**(38), 9218–9223 (2007).

[27] L. Zhong, J. Wang, H. Sheng, Z. Zhang, and S.X. Mao, “Formation of monatomic metallic glasses through ultrafast liquid quenching,” Nature **512**(7513), 177–180 (2014).

[28] J.H. Mentink, and M. Eckstein, “Ultrafast Quenching of the Exchange Interaction in a Mott Insulator,” Phys Rev Lett **113**(5), 57201 (2014).

[29] F. Zhou, J. Williams, S. Sun, C.D. Malliakas, M.G. Kanatzidis, A.F. Kemper, and C.Y. Ruan, “Nonequilibrium dynamics of spontaneous symmetry breaking into a hidden state of charge-density wave,” Nat Commun **12**(1), (2021).

[30] S. Manzeli, D. Ovchinnikov, D. Pasquier, O. V Yazyev, and A. Kis, “2D transition metal dichalcogenides,” Nat Rev Mater **2**(8), 1–15 (2017).

[31] I. Vaskivskyi, J. Gospodaric, S. Brazovskii, D. Svetin, P. Sutar, E. Goreshnik, I.A. Mihailovic, T. Mertelj, and D. Mihailovic, “Controlling the metal-to-insulator relaxation of the metastable hidden quantum state in 1T-TaS_2,” Sci Adv **1**(6), e1500168 (2024).

[32] J.A. Wilson, F.J. Di Salvo, and S. Mahajan, “Charge-density waves and superlattices in the metallic layered transition metal dichalcogenides,” Adv Phys **24**(2), 117–201 (1975).

[33] A. Suzuki, M. Koizumi, and M. Doyama, “Thermal evidences for successive CDW phase transitions in 1T-TaS_2,” Solid State Commun **53**(2), 201–203 (1985).

[34] P.-A. Mante, C.S. Ong, D.F. Shapiro, A. Yartsev, O. Grånäs, and O. Eriksson, “Photo-induced Hidden Phase of 1T-TaS_2 with Tunable Lifetime,” ArXiv, (2022).

[35] J. Maklar, J. Sarkar, S. Dong, Y.A. Gerasimenko, T. Pincelli, S. Beaulieu, P.S. Kirchmann, J.A. Sobota, S. Yang, D. Leuenberger, R.G. Moore, Z.-X. Shen, M. Wolf, D. Mihailovic, R. Ernstorfer, and L. Rettig, “Coherent light control of a metastable hidden state,” Sci Adv **9**(47), eadi4661 (2024).

[36] K. Yumigeta, Y. Qin, H. Li, M. Blei, Y. Attarde, C. Kopas, and S. Tongay, “Advances in Rare-Earth Tritelluride Quantum Materials: Structure, Properties, and Synthesis,” Advanced Science **8**(12), 2004762 (2021).

[37] N. Ru, C.L. Condron, G.Y. Margulis, K.Y. Shin, J. Laverock, S.B. Dugdale, M.F. Toney, and I.R. Fisher, “Effect of chemical pressure on the charge density wave transition in rare-earth tritellurides R Te 3,” Phys Rev B **77**(3), 035114 (2008).

[38] K. Yumigeta, Y. Qin, H. Li, M. Blei, Y. Attarde, C. Kopas, and S. Tongay, “Advances in Rare-Earth Tritelluride Quantum Materials: Structure, Properties, and Synthesis,” Advanced Science **8**(12), 2004762 (2021).

[39] J.G. Bednorz, and K.A. Müller, “Possible high T c superconductivity in the Ba− La− Cu− O system,” Zeitschrift Für Physik B Condensed Matter **64**(2), 189–193 (1986).

[40] A. Schilling, M. Cantoni, J.D. Guo, and H.R. Ott, “Superconductivity above 130 k in the hg–ba–ca–cu–o system,” Nature **363**(6424), 56–58 (1993).

[41] G. Kotliar, and J. Liu, “Superexchange mechanism and d-wave superconductivity,” Phys Rev B **38**(7), 5142 (1988).

[42] D. Fausti, R.I. Tobey, N. Dean, S. Kaiser, A. Dienst, M.C. Hoffmann, S. Pyon, T. Takayama, H. Takagi, and A. Cavalleri, “Light-Induced Superconductivity in a Stripe-Ordered Cuprate,” Science (1979) **331**(6014), 189–191 (2011).

Chapter 2

Theory on Ultrafast Electron Diffraction

The integration of diffraction theory with ultrafast electron diffraction (UED) enables the mapping of dynamical order parameters in strongly correlated materials[1]. This process involves tracking changes in diffraction patterns over extremely short timescales, providing a detailed spatiotemporal picture of the evolving electronic and structural configurations. Mapping the dynamical order parameter with ultrafast scattering techniques becomes a powerful tool for uncovering the underlying mechanisms governing phase transitions and emergent phenomena in these materials. The synergy between UED and diffraction theory not only advances our understanding of ultrafast processes but also allows for the precise characterization of dynamic structural changes, opening avenues for targeted engineering of materials with tailored functionalities.

In the following chapter, the fundamentals of diffraction theory will be introduced. Subsequently, connections will be established between everyday observed processes in ultrafast scenarios, such as the Debye-Waller effect, and the foundational principles of diffraction theory. This approach aims to bridge the gap between theoretical concepts and practical applications, providing a framework for understanding how these principles manifest in the realm of ultrafast electron diffraction.

2.1 Fundamentals on Electron Diffraction

The interaction of electrons with crystalline materials gives rise to the phenomenon of electron diffraction, a powerful technique for probing the atomic structure of solids. To develop a rigorous understanding of electron diffraction, we must delve into the underlying mathematical framework that describes how electrons, as a wave, propagate through a periodic lattice

potential[2,3]. In this section, we will explore the key mathematical concepts and formalisms that form the bedrock of electron diffraction theory.

2.1.1 Diffracted Wavelets from Atoms

Electron diffraction capitalizes on the wave-particle duality inherent in electrons, as described by Louis de Broglie's theory. Electrons exhibit both particle-like and wave-like characteristics, with an associated wavelength tied to their motion. This wave nature becomes evident in experiments involving interactions with crystal lattices or barriers, where periodic structures generate interference patterns akin to those observed with light waves.

To understand the electron diffraction pattern, we start with the scenario with a single free electron scattering with a single atom as illustrated in Fig. 2.1. Obviously, the incident electron is a planewave, and the scattered electron is a spherical wave, they have form:

$$\Psi_{inc} = e^{i(\mathbf{k_0}\cdot\mathbf{r}' - \omega t)}, \tag{2.1}$$

$$\Psi_{scatt} = \frac{f(\mathbf{k_0},\mathbf{k})e^{ik|\mathbf{r}-\mathbf{r}'|}}{|\mathbf{r}-\mathbf{r}'|}, \tag{2.2}$$

Where $\mathbf{k_0}$ is the incident wave vector and $\mathbf{k}$ is the scattered wave vector. The $f(\mathbf{k_0}, \mathbf{k})$ is the atomic form factor, which can be solved by solving the Schrodinger equation:

$$-\frac{h^2}{2m}\nabla^2\Psi(\mathbf{r}') + \boldsymbol{V}(\mathbf{r}')\Psi(\mathbf{r}') = E\Psi(\boldsymbol{r}'). \tag{2.3}$$

The above Schrodinger equation can be solved via make use of Green's function and apply the first Born approximation, which assumes the wave is undiminished and scattered only once by the material. We have:

$$\Psi_{scatt}(\mathbf{s},\mathbf{r}) = \frac{e^{i\mathbf{k}\cdot\mathbf{r}}}{|\mathbf{r}|}f(\mathbf{s}), \tag{2.4}$$

$$f(\mathbf{s}) \equiv -\frac{m}{2\pi\hbar^2}\int V(\mathbf{r}')e^{-i\mathbf{s}\cdot\mathbf{r}'}d^3\mathbf{r}', \tag{2.5}$$

Where the momentum transfer $\mathbf{s} \equiv \mathbf{k} - \mathbf{k_0}$. It is important to notice that the atomic form factor is the Fourier transform of the of the potential of a single atoms $V(\mathbf{r}')$. Given the wave at large momentum transfer is from the atomic core, the atomic form factor approaches the Rutehrford scattering regime and thus drops as $\frac{1}{s^4}$.

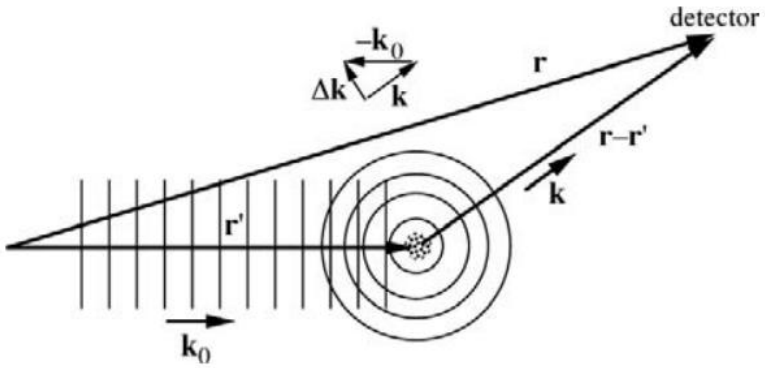

Figure 2.1. A single free electron scattered by a single atom at r'. Adapted from Ref.[3]

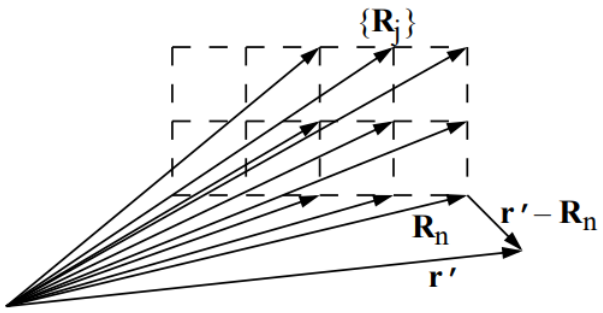

Figure 2.2. A single electron scattered by a crystal, where all atoms on the lattice contribute to the scattering effect. Adapted from Ref.[3]

For diffraction pattern gathered by a crystalline material, the electron is scattered by all the atoms in the lattice. To formulate the scattering by crystalline materials, we denote the position of atoms to be in the set

$\{\mathbf{R_j}\}$, and we replace the $V(\mathbf{r}')$ in Eq. 2.3 with a sum of potential go over all atoms at $\mathbf{R_j}$, $V(\mathbf{r}') = \sum_{\mathbf{R_j}} V_{at}(\mathbf{r}' - \mathbf{R}_j)$, and by a simple change of coordinates $\mathbf{r} = \mathbf{r}' - \mathbf{R_j}$, we have :

$$\Psi(\mathbf{s}) = \sum_{j=1}^{N} f(\mathbf{R_j}, \mathbf{s}) e^{-i\mathbf{s}\cdot\mathbf{R_j}}, \tag{2.6}$$

$$f(\mathbf{R_j}, \mathbf{s}) \equiv \frac{-m}{2\pi r\hbar^2} \int V_{at,R_j}(\boldsymbol{r})\, e^{-i\mathbf{s}\cdot\mathbf{r}} d^3\boldsymbol{r}. \tag{2.7}$$

Eq. 2.6 gives the wave function of an electron scattered by a set of atoms at location $\mathbf{R_j}$, which shows that the diffracted wave is a sum of a series of wavelet with amplitude $f(\mathbf{R_j}, \mathbf{s})$. The amplitude of scattered wave intensity is $I = \Psi^*_{scatt}(\mathbf{s}, \boldsymbol{r})\Psi_{scatt}(\mathbf{s}, \boldsymbol{r})$. The exponential term in $f(\mathbf{R_j}, \mathbf{s})$ gives the relative phase of each wavelet, which determines the diffraction pattern along $\mathbf{s}$ direction is constructive or destructive.

We now consider the atoms position $\mathbf{R_j}$ in a defect free crystal, where the atoms position is determined by a vector to the unit cell $\mathbf{r}_g$ and a vector to the atom's basis within the cell $\mathbf{r}_k$, such that;

$$\mathbf{R_j} = \mathbf{r}_g + \mathbf{r}_k, \tag{2.8}$$

Substitute Eq. (2.8) to Eq.(2.6), we have:

$$\Psi(\mathbf{s}) = \sum_{\boldsymbol{r}_g} e^{-i2\pi\mathbf{s}\cdot\mathbf{r_g}} \sum_{\boldsymbol{r}_k} f(\mathbf{r}_k) e^{-i2\pi\mathbf{s}\cdot\boldsymbol{r}_k}, \tag{2.9}$$

$$\Psi(\mathbf{s}) = S(\mathbf{s})F(\mathbf{s}), \tag{2.10}$$

and

$$S(\mathbf{s}) = \sum_{\mathbf{r}_g}^{lattice} e^{-i2\pi\mathbf{s}\cdot\mathbf{r_g}}, \tag{2.11}$$

$$F(\mathbf{s}) = \sum_{\mathbf{r}_k}^{basis} f(\mathbf{r}_k) e^{-i2\pi\mathbf{s}\cdot\mathbf{r}_k}, \tag{2.12}$$

where $S(\mathbf{s})$ is know as the "Shape Factor" and the $F(\mathbf{s})$ is know as the "Structure Factor". The importance of decomposing the diffracted wave into the shape factor and the structure factor lies in its similarity to the decomposition of the atomic positions in the crystal into a lattice and a basis.

The atomic form factor derived in Eq. 2.4 provides insights into the features of the diffractive wave but does not offer a direct means to calculate the numerical value unless the potential $V(\mathbf{R}_j)$ is known. To

calculate the diffraction pattern intensity in an experiment, the numerical value of the form factor for different atoms is required. This can be obtained using the Mott—Bethe equation[4]:

$$f(s) = \frac{me^2}{32\pi^3\hbar^2\epsilon_0}\frac{1}{s^2}(Z - f_x(s)), \tag{2.13}$$

$$f_x(s) = \sum_{i=1}^{4} a_i e^{(-b_i\frac{s}{4\pi})} + c, \tag{2.14}$$

where $f_x(s)$ is the atomic for factor for X-ray scattering[5], the numerical value of coefficient a_i, b_i, and c_i for different atoms can be find in Ref.[6].

2.1.2 Electron Diffraction with Crystal

In the previous section, the expression of the scattered wave was derived by solving the Schrödinger equation. From there, a generalized description of the intensity of the diffracted wave was deduced. In this section, the crystal structure will be taken into consideration to provide a comprehensive description of the relationship between the diffraction pattern and the properties of the crystal.

Consider a large crystal, the constructive diffraction can be tracked from the translational symmetry of unit cells. We start by considering a simple case, where only one atom is in a unit cell, in this case, the form factor *f*(**r**) is unchanged under any lattice translation: $f(\mathbf{r}) = F(r + \mathbf{R})$, From Eq. 2.6, we have:

$$\Psi_{max} \propto Max(\sum_{\boldsymbol{R}} e^{-i\mathbf{s}\cdot\mathbf{R}_j}). \tag{2.15}$$

We write the expression of $\mathbf{R}_j$ is the Bravia lattice of the crystal, we can explicitly express it as:

$$\mathbf{R}_j = m\mathbf{a_1} + n\mathbf{a_2} + o\mathbf{a_3}, \tag{2.16}$$

where $\mathbf{a_1}$, $\mathbf{a_2}$, $\mathbf{a_3}$ are the primitive vectors that span the $\{\mathbf{R}_j\}$ space. The maxima happens when the exponent term equals to 1, or:

$$\mathbf{s}\cdot(ma_1 + na_2 + oa_3) = 2\pi\cdot integer. \tag{2.17}$$

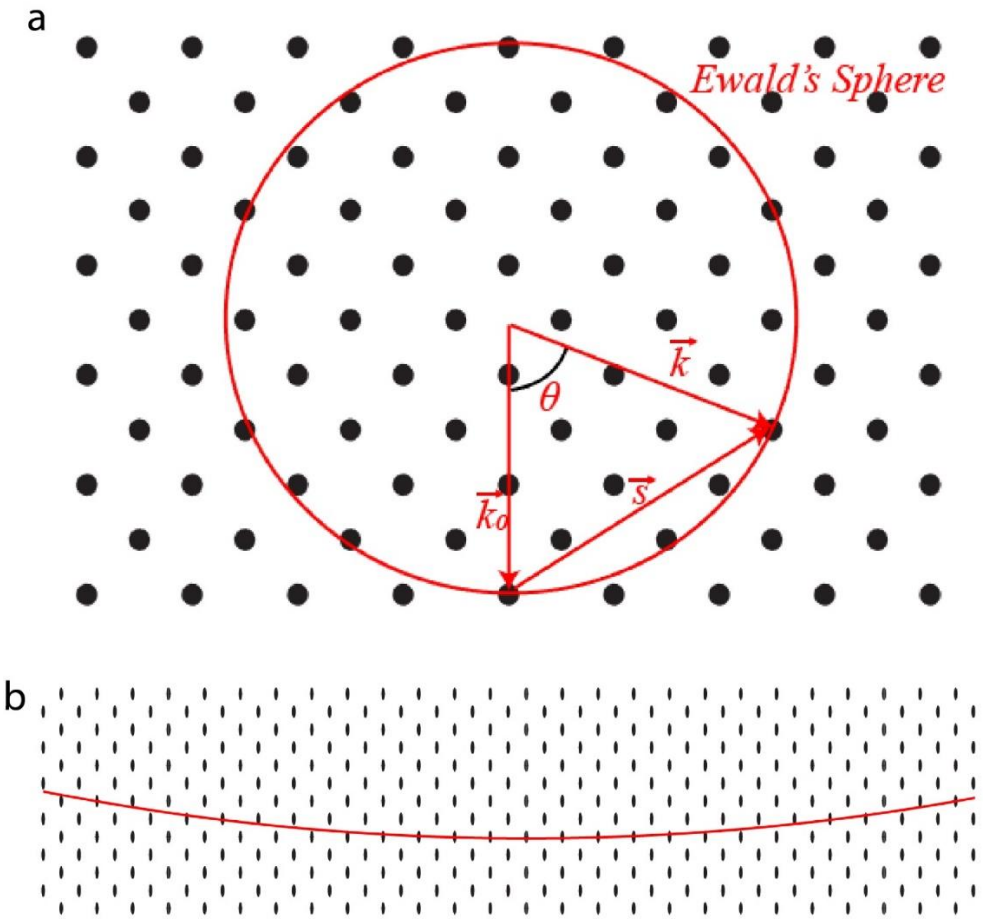

Figure 2.3. Ewald's Sphere cutting reciprocal lattice. a. Ewald's Sphere and Laue condition, s is the momentum transferred can be calculated via $\mathbf{s} = \mathbf{k} - \mathbf{k_0} = \frac{4\pi}{\lambda} \sin\left(\frac{\theta}{2}\right) \hat{s}$. **b.** More relativistic Laue condition for thin sample at UED. The electron wavelength is much larger than the spacing between reciprocal lattices. The reciprocal lattice is elongated along the direction of the electron beam due to sample's finite thickness.

Since $\boldsymbol{R_j}$, as well as its Fourier transform the reciprocal lattice **G** in reciprocal space, are complete sets, thus all possible **s** can be expressed as:

$$\mathrm{s} = \mathbf{G}_{hkl} = ha_1^* + ka_2^* + la_3^*, \tag{2.18}$$

$$a_i^* = 2\pi \frac{a_j \times a_k}{a_i \cdot a_j \times a_k}, \tag{2.19}$$

which gives us the Laue condition: *Diffraction occurs when **s** is a vector of the reciprocal lattice.* And we can construct an Ewald's sphere, which is a sphere in reciprocal space with length |**k**|, represents the set of all possible diffraction vectors satisfying the Laue conditions for a given incident beam direction.

In the above derivation, all scattered wavevector **k** can be treated equally. This is held true in the experiment due to the distance from detector to the crystal is much larger than the separation among different atoms in the crystal. On the other hand, if we draw out the reciprocal lattice, and draw the sphere with length of the incident wavevector, all reciprocal lattice that cut with the surface of the sphere will satisfy the Laue condition. It is worth noting that in the realistic case, the wavelength of electron beam is much smaller than the atom distance of crystals, thus the Ewald's sphere's radius will be much larger than the reciprocal lattice. Another factor to consider in electron diffraction is that the sample usually has small thickness, this is especially the case in UED experiments due to a small thickness is needed to maintain a homogeneous laser excitation profile across the whole thickness of sample, which makes the reciprocal space elongated.

An important observation from the Laue condition is that, for the general purpose, the crystal contains large amount of lattice and the momentum transfer ***s*** is perpendicular to the lattice vector (Eq. 2.17), thus the Shape factor given in Eq.2.11 equals 1. The diffraction's pattern and intensity are solely determined by the Structure factor in Eq. 2.12. For the diffraction at momentum space $\mathbf{s} = \mathbf{G}_{hkl} = h\mathbf{a_1^*} + k\mathbf{a_2^*} + l\mathbf{a_3^*}$

$$I_{hkl} \propto |F_{hkl}|^2 \tag{2.20}$$

and

$$F_{hkl} = \sum_{i=1}^{n} f_j e^{-2\pi i(hx_i+ky_i+lz_i)}, \quad (2.21)$$

where the i^{th} atmo has an atomic coordinate of (x_i, y_i, z_i).

2.2 Ultrafast Electron Diffraction

The previous section established the basic formalism of diffraction theory. In UED, the interactions between the laser and the material give rise to a wide array of dynamic processes[1]. To illustrate how the diffraction methodology enables the tracking of material dynamics on ultrafast timescales[7], some representative examples will be discussed in this section.

2.2.1 Detecting Order and Periodicity Change

The application of ultrafast laser pulses can induce various pathways of phase transitions in materials, many of which involve modifications to the original system's lattice, charge, or orbital order. Consequently, these alterations lead to changes in the set of reciprocal lattice vectors. When transformations alter the space group (symmetry), a distinct set of reciprocal lattice vectors emerges, resulting in the manifestation or disappearance of Bragg peaks within the diffraction pattern. Fig. 2.4 demonstrates the melting of a gold crystal into the liquid phase as detected by UED[8]. As the gold melts from its BCC solid phase into the liquid phase, all the sharp diffraction peaks are lost.

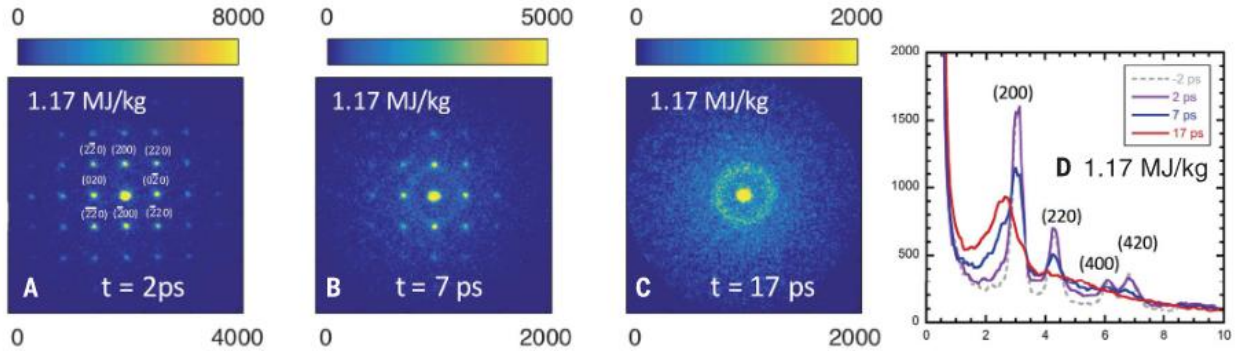

Figure 2.4. UED experiment on the ultrafast melting of gold crystal. Adapted from Ref.[8]

On the other hand, transformations that solely influence lattice constants (e.g., thermal expansion or strain) without affecting the space group or symmetry cause a rescaling of the existing reciprocal lattice vectors, leading to shifts in the positions of Bragg peaks rather than the emergence of new peaks. Fig 2.5 illustrates the lattice spacing change observed in PbSe quantum dots under laser excitation[9]. The diffraction peak position shift is caused by the increase in lattice temperature within approximately 10 ps, followed by a decrease back to the original value after about 40 ps.

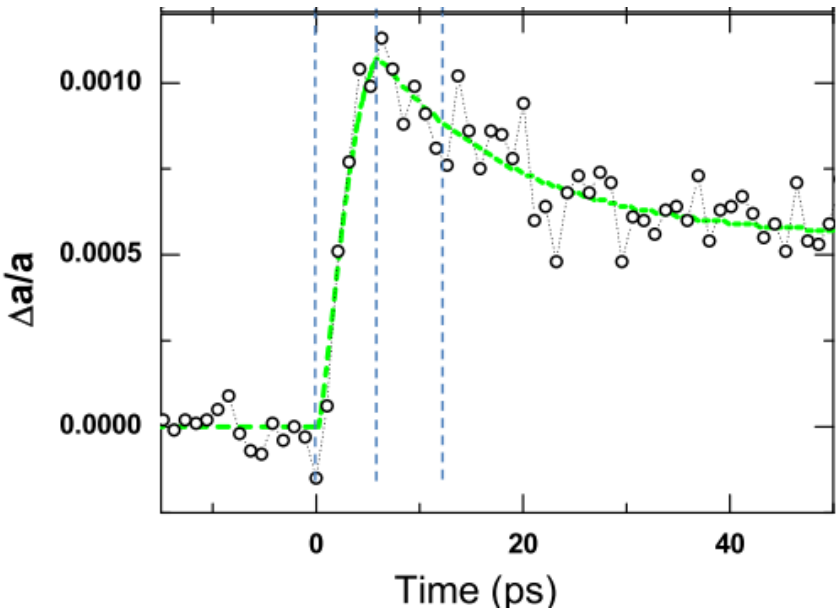

Figure 2.5. Relative lattice spacing change as a function of time for PbSe quantum dots after laser excitation. Adapted from Ref.[9]

Moreover, strain, which results in spatially varying lattice constants, can also be investigated through electron diffraction patterns by examining peak broadening and asymmetry. Figure 2.6 presents data obtained from MeV UED for SnSe[10], showing the difference between 1.7 ps and negative time. A clear broadening of the peak width along the Γ to Z direction is observed, with the schematic illustrating the generation of interlayer shear strain caused by lattice mismatch.

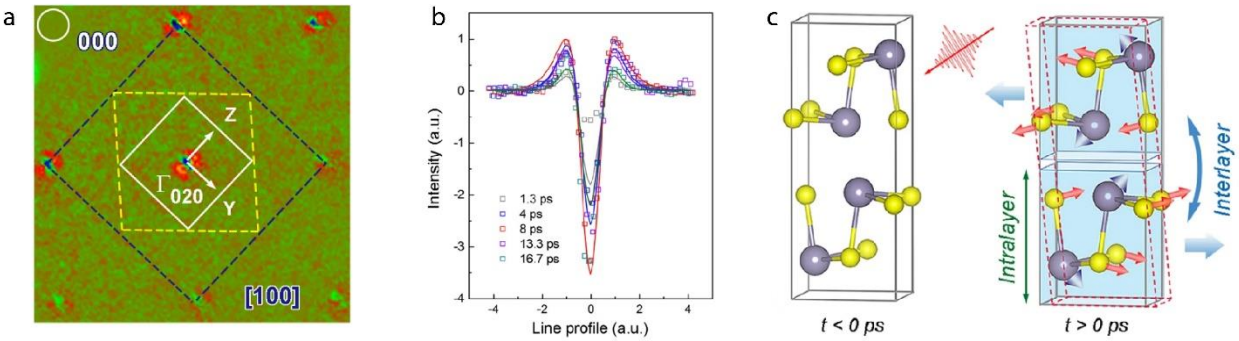

Figure 2.6. UED observed shear strain from lattice mismatch after photoexcitation. The Brillouin zones around the (020) Bragg peak (Γ point) with the 1st, 2nd, and 3rd Brillouin zone boundaries marked by white, yellow and black lines, respectively. The (000) beam position is indicated by the circle. **a.** Differential diffraction patterns at 1.7ps. **b.** Line profiles along Γ-Z direction of the Bragg peak in the UED intensity difference pattern as a function of time. The squares are experimental data, the solid lines are simulation result. **c.** Photoinduced atomic displacements and relaxation that can be attributed to the transverse optical Ag phonon modes. The Sn-Se movement increases the intralayer lattice symmetry, while induces interlayer shear strain along c axis, which yields lattice distortions and formation of domains. Adapted from Ref.[10]

2.2.2 Coherent motion

The coherent motion of atoms within a material can be induced by optical excitation, without altering the crystal's space group or symmetry. This motion may be associated with a coherently excited vibration (oscillation) or the structural pathway through which the material transitions between two phases. Such atomic motion modifies the atomic coordinates $\mathbf{r}$, which consequently modulate the interference condition in the structure factors $F(\mathbf{s})$. These changes in the structure factor, resulting from the atomic motion, are directly observable as variations in the intensity of Bragg peaks across the entire detector, in a manner characteristic of the motion. The effects are not limited to a single Bragg peak; instead, relevant information is distributed throughout the diffraction pattern.

As a result, a comprehensive characterization of the motion generally requires the time dependence of a sufficiently complete set of diffraction peaks, rather than one. For instance, a coherent optical phonon will modulate the $e^{-i(\mathbf{s}\cdot\mathbf{r})}$ phase term of the structure factor $F(\mathbf{s})$. This modulation will produce a characteristic intensity variation at the phonon frequency, but only in diffraction peaks associated with reciprocal lattice vectors having a nonzero projection onto the atomic motion $\boldsymbol{\mu}$, i.e., at the Bragg peak $\mathbf{G}_{hkl}$ such that $\mathbf{G}\cdot\boldsymbol{\mu} \neq 0$. Fig. 2.7 shows the coherent excitation of the transverse optical shearing mode in graphite[11]. The {100} family of peaks exhibit oscillatory dynamics, with the $(1\bar{1}0)$ peak oscillation out of phase by π with respect to the other peaks. The phase difference illustrates the different signs in the dot product between the different Bragg peaks and the phonon mode.

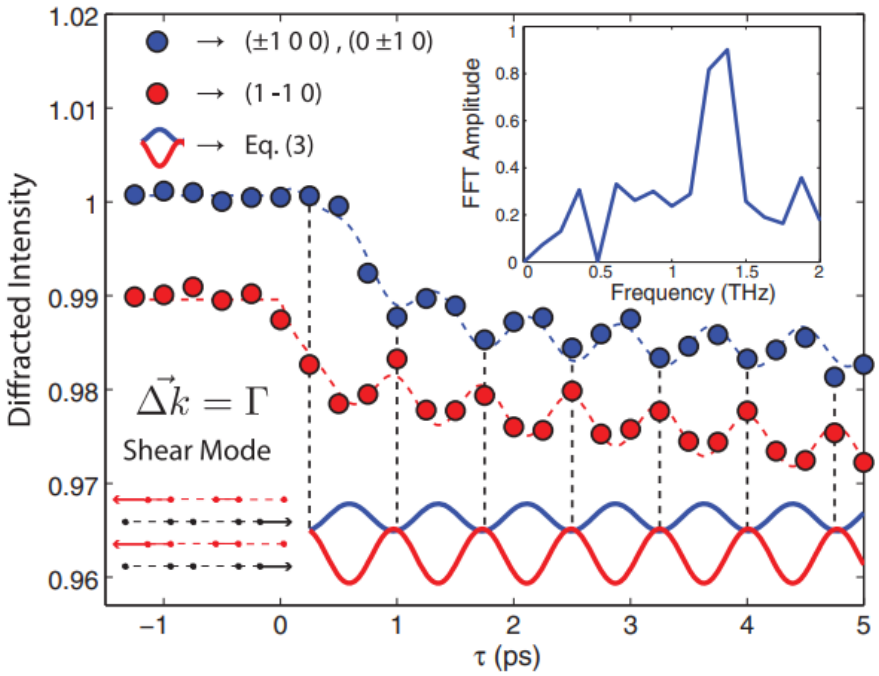

Figure 2.7 Coherent excitation of the transverse optical shearing mode observed in graphite after photoexcitation. The {1 0 0} family of peaks exhibit oscillatory dynamics, with the $(1\ \bar{1}\ 0)$ peak oscillation out of phase by π with respect to the other peaks. Adapted from Ref.[11]

2.2.3 Debye-Waller Factor

In laser-excited materials, it is generally believed that the laser directly transfers energy to electrons, increasing the electron temperature. The electron bath releases its energy through electron-phonon coupling, either coherently or incoherently. This electronic energy relaxation channel heats up the lattice and increases the vibration of the atoms, resulting in a decrease in Bragg peak intensity. This phenomenon is known as the Debye-Waller effect.

In the case of electron diffraction formed with crystalline material, without considering multiple scattering, Eq. 2.7 can be rewrite as:

$$f(s) = \sum_{\{\boldsymbol{G}\}} \delta(\mathbf{s} - \mathbf{G}_{hkl}) \sum_{\boldsymbol{j}} V_j(\mathbf{s}) e^{-i(\mathbf{s}\cdot\mathbf{R}_j)}. \tag{2.22}$$

Following the perturbative treatment[12], the electron scattering intensity can be expanded in a Taylor series $I(\boldsymbol{s}) \approx I_0(\boldsymbol{s}) + I_1(\boldsymbol{s}) + \cdots$ for the case considering small atomic displacements away from the position in the ideal crystal structure. Where the zero-other term[7] can be written out via Combining Eq.2.22, Eq. 2.21 and Eq. 2.20:

$$I_0(\mathbf{s}) \propto \delta(\mathbf{s}-\mathbf{G})\left|\sum_j f_j(\mathbf{s}) e^{-M_j(\mathbf{s})} e^{-i(\mathbf{s}\cdot\mathbf{r})}\right|^2, \tag{2.23}$$

where the delta function is imposed to satisfy the Laue condition, and the anisotropic Debye-Waller factor (DWF) $e^{-M_j(\mathbf{s})}$depends on the $M_j(\mathbf{s})$ for each basis atom, for the case the DWF is isotropic, we can write out $M_j(\mathbf{s})$ as:

$$M_j(\mathbf{s}) = 2\pi^2 < u_j^2 > s^2, \tag{2.24}$$

where u_j is the displacements away from the position in the ideal crystal structure. Thus we can connect the Bragg peak intensity change to the DWF at time t after pump arriving time t_0 is given by Eq. 2.24 and Eq. 2.23, we have:

$$-\ln\frac{I(\boldsymbol{s},t)}{I(\boldsymbol{s},t_0)} = 2\pi^2 < \Delta u(t)^2 > s^2. \tag{2.25}$$

Eq. 2.25 gives the Bragg-peak intensity change that converted to the change in the mean-square vibrational amplitude. Figure 2.8 shows the Bragg peak intensity change for copper after laser excitation[13]. The left panel depicts the dynamics for different Bragg peak intensity changes due to the Debye-Waller factor, which gives a lattice thermalization time of approximately 5 ps. In the right panel, a clear linear relationship between $\ln\frac{I(\boldsymbol{s},t)}{I(\boldsymbol{s},t_0)}$ and s^2.

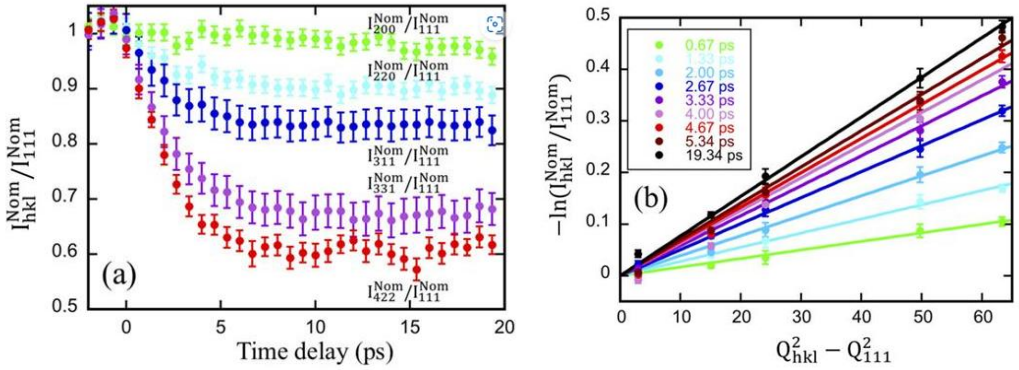

Figure 2.8. Debye-Waller effect observed in laser excited copper via UED. a. Temporal evolution of the normalized intensities of selective diffraction peaks (hkl) at an incident pump fluence of 10.1 mJ/cm^2. The normalization at each data point was performed relative to the intensity of diffraction peak (111) to minimize shot-to-shot fluctuation. **b.** The natural logarithm of normalized intensity change, shown by **a**, as a function of square of transferred momentum at selective pump-probe time delays. Solid lines represent the linear fits to the experimental data. Adapted from Ref.[13]

2.2.4 Phonon Mode Amplitude

The first-order term in the expansion of diffraction intensity[7] is called the phonon-diffuse scattering intensity and is given by:

$$I_1(\boldsymbol{s}) \propto \sum_j \frac{n_{j,\boldsymbol{s}-\boldsymbol{G}}+0.5}{\omega_{j,\boldsymbol{s}-\boldsymbol{G}}} \left|F_{1j}(\boldsymbol{s})\right|^2, \tag{2.26}$$

where the $n_{j,\mathbf{s}-\mathbf{G}}$ is the phono occupancy at $\mathbf{k} = \mathbf{s} - \mathbf{G}$, $\omega_{j,\mathbf{s}-\mathbf{G}}$ is the corresponding frequency, and their ratio $\frac{n_{j,\mathbf{s}-\mathbf{G}}+0.5}{\omega_{j,\mathbf{s}-\mathbf{G}}}$ gives the phonon mode amplitudes. $F_{1j}(\mathbf{s})$ is the one-phonon structure factor given by:

$$F_{1j}(\mathbf{s}) = \sum_\alpha \frac{f_\alpha(\mathbf{s})}{\sqrt{m_\alpha}} e^{-M_\alpha(\mathbf{s})\cdot(\mathbf{s}\cdot\hat{e}_{j,\alpha,\mathbf{s}-\mathbf{G}})}, \tag{2.27}$$

where $\hat{e}_{j,\alpha,\boldsymbol{s-G}}$ is the phonon eigenvectors, describes the direction of the phonon mode at frequency $\omega_{j,\boldsymbol{s-G}}$. Here, unlike the affect from DWF, $M_\alpha(\boldsymbol{s})$ is not isotropic and depends on the directionality of phonon mode, it can be written out as:

$$M_\alpha(\mathbf{s}) = \frac{1}{4m_\alpha}\int \frac{1}{8\pi^3}\sum_j \left|a_{j,\mathbf{k}}\right|^2 \left|s\cdot \hat{e}_{j,\alpha,\mathbf{k}}\right|^2. \tag{2.28}$$

For a typical response after laser excitation process the phonon frequency are usually unchanged, the change of intensity at $\mathbf{s}$ at time t after pump arriving time t_0 is then given by Eq. 2.26:

$$\Delta I_1(\boldsymbol{s},t) \propto \sum_j \frac{\Delta n_{j,\mathbf{k}}(t)}{\omega_{j,\mathbf{k}}(t_0)} |F_{1j}(\mathbf{s},t_0)|^2. \tag{2.29}$$

Eq. 2.29 gives diffraction intensity change at wave vector $\mathbf{k} = \mathbf{G} - \mathbf{s}$, which in data are illustrated as the change of diffusive scattering intensity near Bragg peak G. The alteration in diffusive intensity, when properly correlated with the phonon system, shall impart knowledge pertaining to the amplitude of the phonon mode at a specified wave vector. This, in turn, possesses the capacity to furnish insights into the dynamics of phonon modes and band structures, in a manner akin to the methodology employed by angle-resolved photoelectron spectroscopy, which facilitates the elucidation of the dynamics of electronic states and bands.

Fig. 2.9 presents an example of phonon modes observed by MeV UED after laser excitation of 1T-$TiSe_2$[14]. After excitation, an increase in diffusive scattering at different times is shown in panels a to d. In panels g and h, the diffusive scattering intensity contribution from different phonon modes is calculated. By integrating the diffusive scattering signal at different corresponding regions, the dynamics of the change in amplitude for each phonon mode can be extracted, as shown in panels i to k.

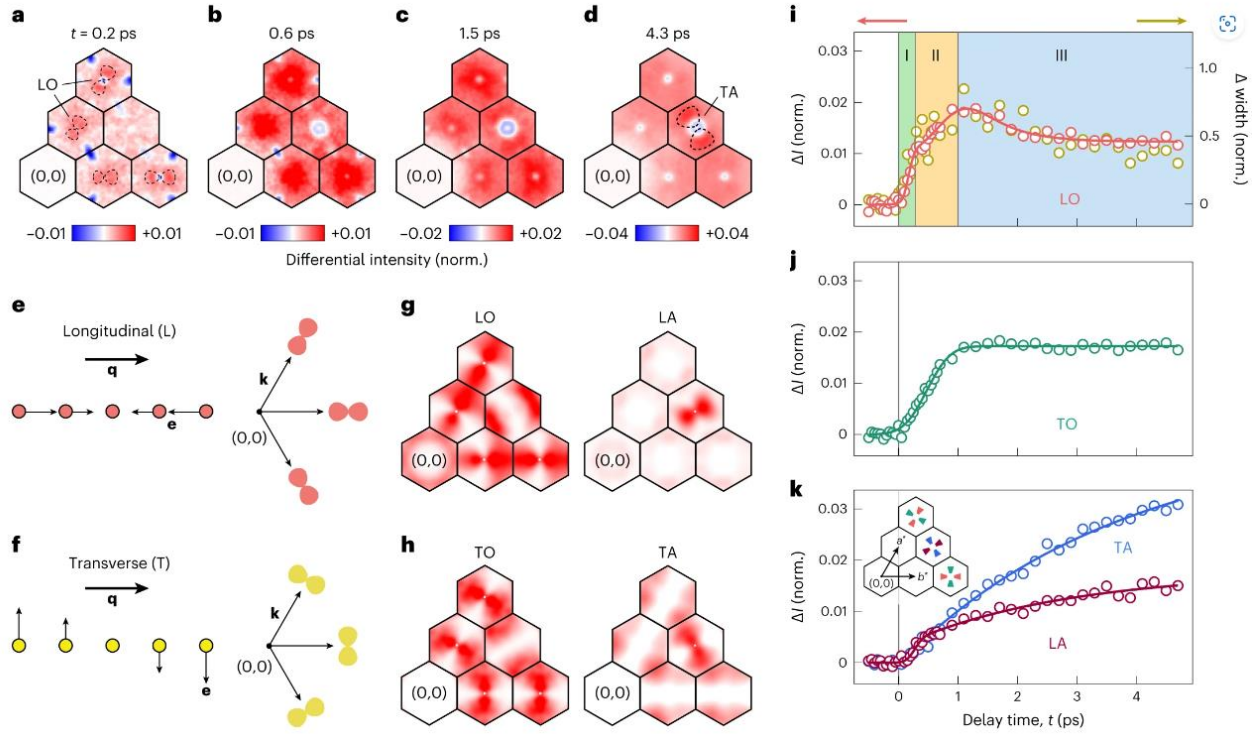

Figure 2.9. Phonon mode observed in diffusive scattering in UED signal. a. – d. Differential diffraction patterns zooming into the six Brillouin zones near the diffracted beam at (0, 0). Regions of interest marked by the dashed curves in a and d highlight the diffuse scatterings from LO phonons and TA phonons, respectively. **e, f.** Schematic of the atomic displacements (left) and diffuse scatterings (right) for longitudinal **e** and transverse **f** phonons for a given wavevector q, which is defined from the closest Γ point. **g, h.** Calculated one-phonon structure factor for longitudinal (L) and transverse (T) phonons from the optical (O) and acoustic (A) branches. Adapted from Ref.[14]

REFERENCES

REFERENCES

[1] A.H. Zewail, “Four-dimensional electron microscopy,” Science (1979) **328**(5975), 187–193 (2010).

[2] D.B. Williams, C.B. Carter, D.B. Williams, and C.B. Carter, *The Transmission Electron Microscope* (Springer, 1996).

[3] B. Fultz, and J.M. Howe, *Transmission Electron Microscopy and Diffractometry of Materials* (Springer Science & Business Media, 2012).

[4] H.A. BETHE, “Theory of Atomic Collisions,” Nature **167**(4240), 165 (1951).

[5] D. Rez, P. Rez, and I. Grant, “Dirac–Fock calculations of X-ray scattering factors and contributions to the mean inner potential for electron scattering,” Acta Crystallogr A **50**(4), 481–497 (1994).

[6] H. Fuess, M.G. Rossmann, E. Arnold, S. Hall, B. McMahon, T. Hahn, H. Wondratschek, U. Müller, U. Shmueli, and E. Prince, *Complete Online Set of International Tables for Crystallography* (2007).

[7] D. Filippetto, P. Musumeci, R.K. Li, B.J. Siwick, M.R. Otto, M. Centurion, and J.P.F. Nunes, “Ultrafast electron diffraction: Visualizing dynamic states of matter,” Rev Mod Phys **94**(4), 45004 (2022).

[8] M.Z. Mo, Z. Chen, R.K. Li, M. Dunning, B.B.L. Witte, J.K. Baldwin, L.B. Fletcher, J.B. Kim, A. Ng, and R. Redmer, “Heterogeneous to homogeneous melting transition visualized with ultrafast electron diffraction,” Science (1979) **360**(6396), 1451–1455 (2018).

[9] X. Wang, H. Rahmani, J. Zhou, M. Gorfien, J. Mendez Plaskus, D. Li, R. Voss, C.A. Nelson, K. Wai Lei, and A. Wolcott, “Ultrafast lattice dynamics in lead selenide quantum dot induced by laser excitation,” Appl Phys Lett **109**(15), (2016).

[10] W. Wang, L. Wu, J. Li, N. Aryal, X. Jin, Y. Liu, M. Fedurin, M. Babzien, R. Kupfer, M. Palmer, C. Petrovic, W. Yin, M.P.M. Dean, I.K. Robinson, J. Tao, and Y. Zhu, “Photoinduced anisotropic lattice dynamic response and domain formation in thermoelectric SnSe,” NPJ Quantum Mater **6**(1), 97 (2021).

[11] R.P. Chatelain, V.R. Morrison, B.L.M. Klarenaar, and B.J. Siwick, “Coherent and incoherent electron-phonon coupling in graphite observed with radio-frequency compressed ultrafast electron diffraction,” Phys Rev Lett **113**(23), 235502 (2014).

[12] R. Xu, and T.C. Chiang, “Determination of phonon dispersion relations by X-ray thermal diffuse scattering,” **220**(12), 1009–1016 (2005).

[13] M.Z. Mo, V. Becker, B.K. Ofori-Okai, X. Shen, Z. Chen, B. Witte, R. Redmer, R.K. Li, M. Dunning, and S.P. Weathersby, “Determination of the electron-lattice coupling strength of copper with ultrafast MeV electron diffraction,” Review of Scientific Instruments **89**(10), (2018).

[14] Y. Cheng, A. Zong, L. Wu, Q. Meng, W. Xia, F. Qi, P. Zhu, X. Zou, T. Jiang, and Y. Guo, "Ultrafast formation of topological defects in a two-dimensional charge density wave," Nat Phys, 1–7 (2024).

Chapter 3

Instrument Development

Having delved into the theoretical underpinnings of UED in the preceding chapter, we now shift our focus to the implementation of the experiments. This chapter serves as a gateway into the core elements of instrumentation development of the ultrafast electron microscopes (UEM), where we carry out the UED and ultrafast optical pump-probe measurements.The significance of the UED and UEM instrument[1] lies not only in its technical sophistication but also in its ability to bridge the theoretical insights with empirical observations over the different ultrafast processes at MSU. In this chapter, I aim to present a detailed account of the instrumental setup employed in our experiments, outlining the key components, their functionalities, and the design principle that serves our needs.

3.1 Framework of the UEM System

Ultrafast Electron Microscopy (UEM) systems can be designed through various approaches, including modifying[2–4] a transmission electron microscope (TEM) or constructing one from scratch[5]. Regardless of the design method, certain components are essential in all UEM setups[1].

Inherent to the name, UEM utilizes electrons for material observation, with the electron gun being a crucial element to generate and accelerate electrons toward the sample. This is achieved conventionally by modifying the emitter of (field emission or thermionic) TEM into a photo-emitter driven by a laser pulse. The "ultrafast" attribute is typically

achieved through a pump-probe setup involving an additional femtosecond laser pulse as the pump pulse initiating changes in the sample. The ultrashort electron pulse taken from photoemitter is timed to arrive at the sample with different delay time to capture the dynamics. This is accomplished by tuning the condenser lens systems to from the appropriate beam illumination at the specimen stage. The post specimen optical systems, considering objective lenses, intermedium lenses, and projective lenses, are adjusted to reflect the information via imaging, diffraction, or inelastic scattering. Recording information from the electrons necessitates a sensitive detection device, with a charge-coupled device (CCD) or direct electron (DE) cameras replacing phosphor screens.

Such conventional TEM modified system typically operates on a high pump-probe repetition rate (f_{rep}) with a small photoemitter is pioneered by A.H. Zewail at Caltech[6,7]. The effort at MSU is geared towards obtaining single-pulse high luminosity so material processes that cannot rapidly recover can still be investigated by a UEM. This new effort requires the TEM system to be re-designed around a new type of photo-electron gun. Fig. 3.1 shows the general schematic of UEM-II system at MSU, where the key components are depicted. The new key element is the RF cavity, serving as a longitudinal condenser lens to focus the electron pulse into a pancake beam, that maintains the coherent length while spatially compressed to achieve high time resolution. The details for this optical control will be given in chapter 4.

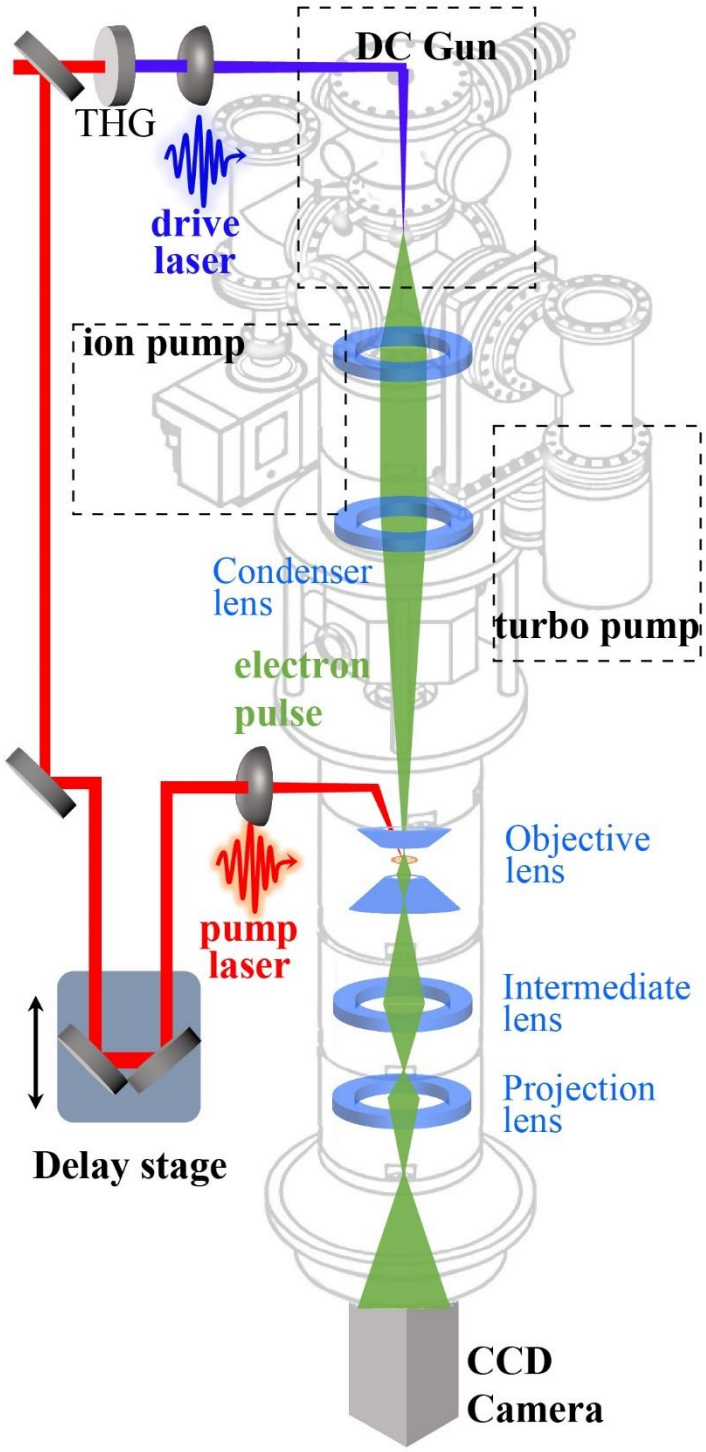

Figure 3.1. Schematic of 2nd generation UTEM in Ruan group. Adapted from Ref.[8]

The complex electron optics that were preserved during the UEM-II modification process provide multi-modality functionality[9]. In particular, a few techniques are shown in Fig. 3.2 and Fig. 3.3, where simplified beam paths are shown to provide a comparison between different modalities. Fig. 3.2 and Fig. 3.3(a) shows the (simplified) electron beam diagram for high resolution imaging mode, where no aperture beyond the sample is implemented. Fig. 3.3 (c) shows the electron beam diagram for selected area diffraction (SAD), in which by selecting a certain region on the image plane, it ensures that the diffraction pattern gathered comes from the exact same region. SAD combines both real-space imaging and reciprocal-space diffraction information, enabling the investigation of local structures via the diffraction method. Fig. 3.3 (b) shows the electron beam diagram for dark-field (DF) imaging, which is on the opposite side of the SAD approach. In the DF approach, an objective aperture is inserted at the focal plane, where a certain region in the reciprocal space is selected. Only the electron beam path through the aperture later forms an image. DF enables the study of real-space information on the selected reciprocal space, where an example is to study the domain growth of CDW material. In Fig. 3.3(b), the DF image gathered are from single NC-CDW diffraction peaks for 1T-TaS_2.

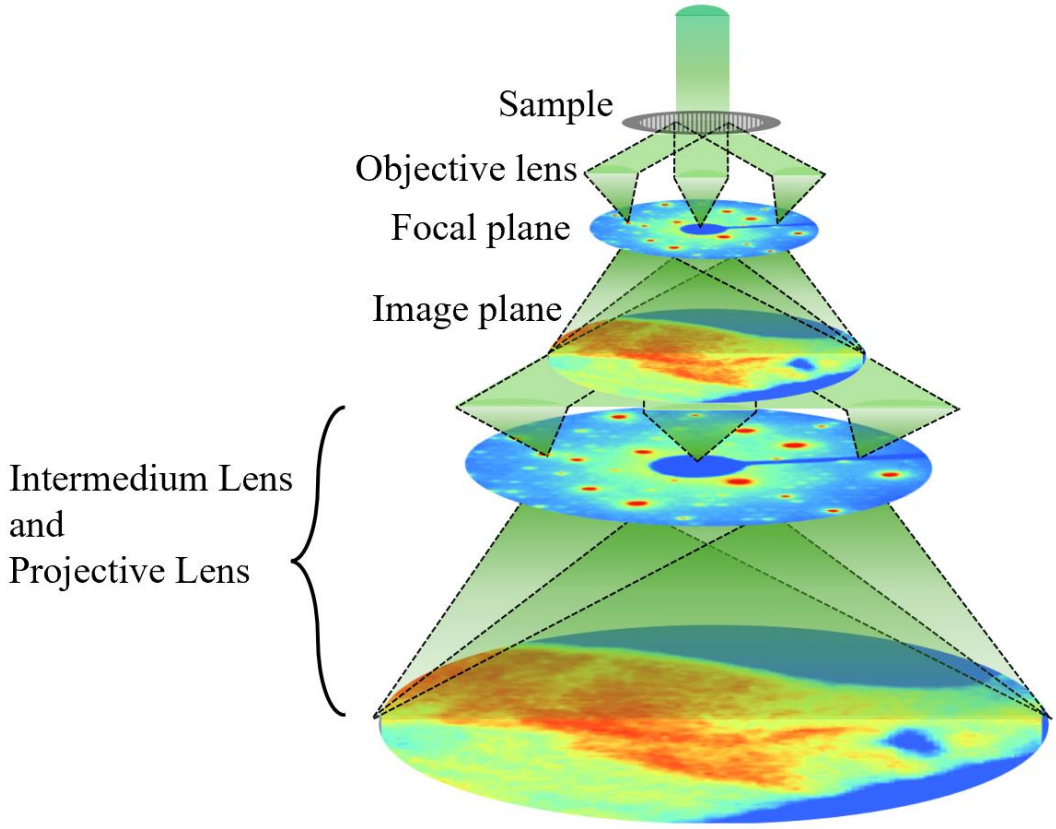

Figure 3.2 Electron beam path for bright field imaging mode.

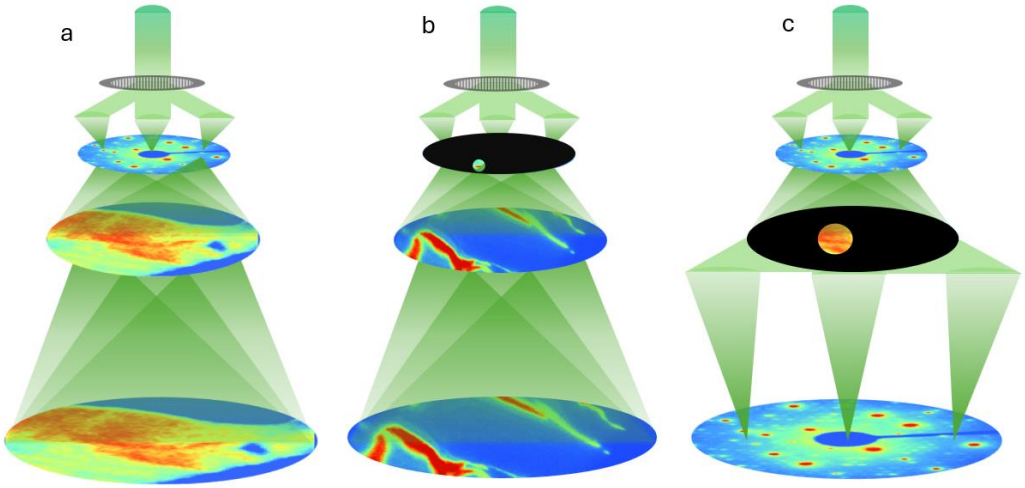

Figure 3.3 Simplified electron beam path. a. High resolution imaging mode. **b.** Dark field imaging mode. **c.** selected area diffraction mode. The crossover between intermedium lenses and projective lenses are omitted for simplicity.

3.2 The Upgrade of Ultrafast Electron Crystallography

During the early phase of my graduate study, I participated in the upgrade effort for the existing Ultrafast Electron Crystallography (UEC) system. The UEC is the first ultrafast electron diffractometer built in Ruan group. It utilizes a compact gun design[10] to minimize electron pulse elongation due to the space-charge effect. Previously, it achieved sub-picosecond (ps) resolution with 1000 electrons per pulse[11].

The laser system in UEC serves two purposes: driving the electron gun and exciting the sample to initiate change. The laser system starts with the output of a Ti:Sapphire femtosecond laser system that delivers 2.5 mJ/cm^2, 45 fs, 800 nm laser pulses at a 1 kHz repetition rate. The output pulses are split into two paths, pump and probe, by a beam splitter. The pump path can either pass through an optical parametric amplifier (OPA) that generates a broad range of selectable optical wavelengths, from 285 to 3300 nm, or be used as is to pump the sample with an 800 nm beam. The laser pulses along the probe path are frequency-tripled to 266 nm to drive the electron gun.

Immediately after the electrons are extracted from the anode, a gun lens is positioned to prevent the electrons from becoming too divergent. Two sets of deflector rods are attached to the gun lens to bend the beam such that the electron beam will hit the center of the camera. The sample is located 20 mm away from the gun lens; this short distance is chosen to reduce the pulse duration increase due to the space-charge effect. The camera assembly starts with a phosphor screen, which is coated with a 60 nm Al layer to block visible light while still allowing electrons to pass through and be converted to photons. These photons then enter a microchannel plate, where they can be amplified up to 1000

times. The amplified photons finally arrive at the CCD camera chip, and the diffraction pattern is recorded.

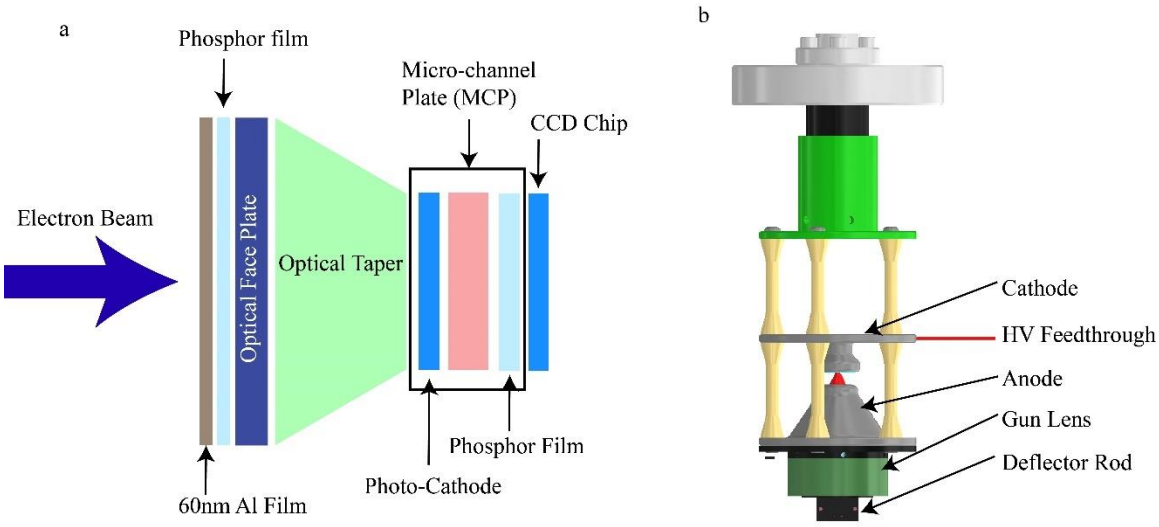

Figure 3.4. **a.** CCD camera assmebly. **b.** 30kV electron gun.

The upgrade performed during my PhD tenure was targeted to improving both temporal resolution and dosage by adding an RF cavity to compress the electron beam. The principles regarding how the RF cavity compresses the electron pulse are given in chapter 4. Fig 3.5 shows the schematic of UEC before and after the upgrade.

The insertion of the RF cavity brought about a few challenges. Firstly, the RF cavity's vacuum, made by many O-ring seals, has a poor vacuum at 5 x 10^{-5} torr. However, the electron gun, in this case with an extraction field of 7 MV/m, requires a vacuum better than 5 x 10^{-9} torr[12]. To achieve this, a 2-level differential pumping system was designed, as shown in Fig. 3.6. A total of three 2 mm apertures are used to limit the flow rate, and a final vacuum of 8 x 10^{-10} torr is achieved in the gun chamber.

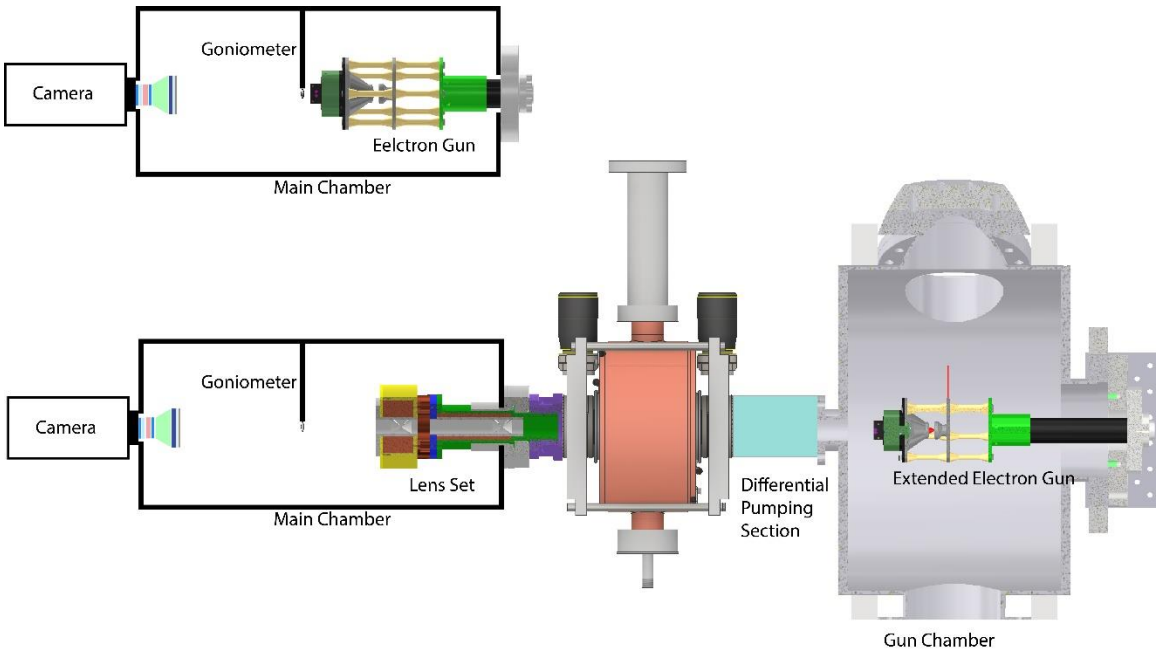

Figure 3.5. Comparison between UEC setup before and after upgrade. Top: UEC after upgrade. Bottom, UEC before upgrade. The main chamber contains a goniometer system, sample transfer, and cryocooling units under ultrahigh vacuum. The camera and the main chamber are not drawn to scale.

Another issue that needs to be addressed is the spot size of the electron beam. Prior to the upgrade, the distance between the electron gun lens and the sample was 20 mm[13]. After the upgrade, this distance increased to 750 mm. The 35-fold increase in distance reduced the minimum focused spot size of the electron beam by the same factor, giving the electron beam a size of $\delta = 500$ μm and making the dosage unacceptably low. To obtain a sufficient dose, the electron beam needs to be demagnified 10 times.

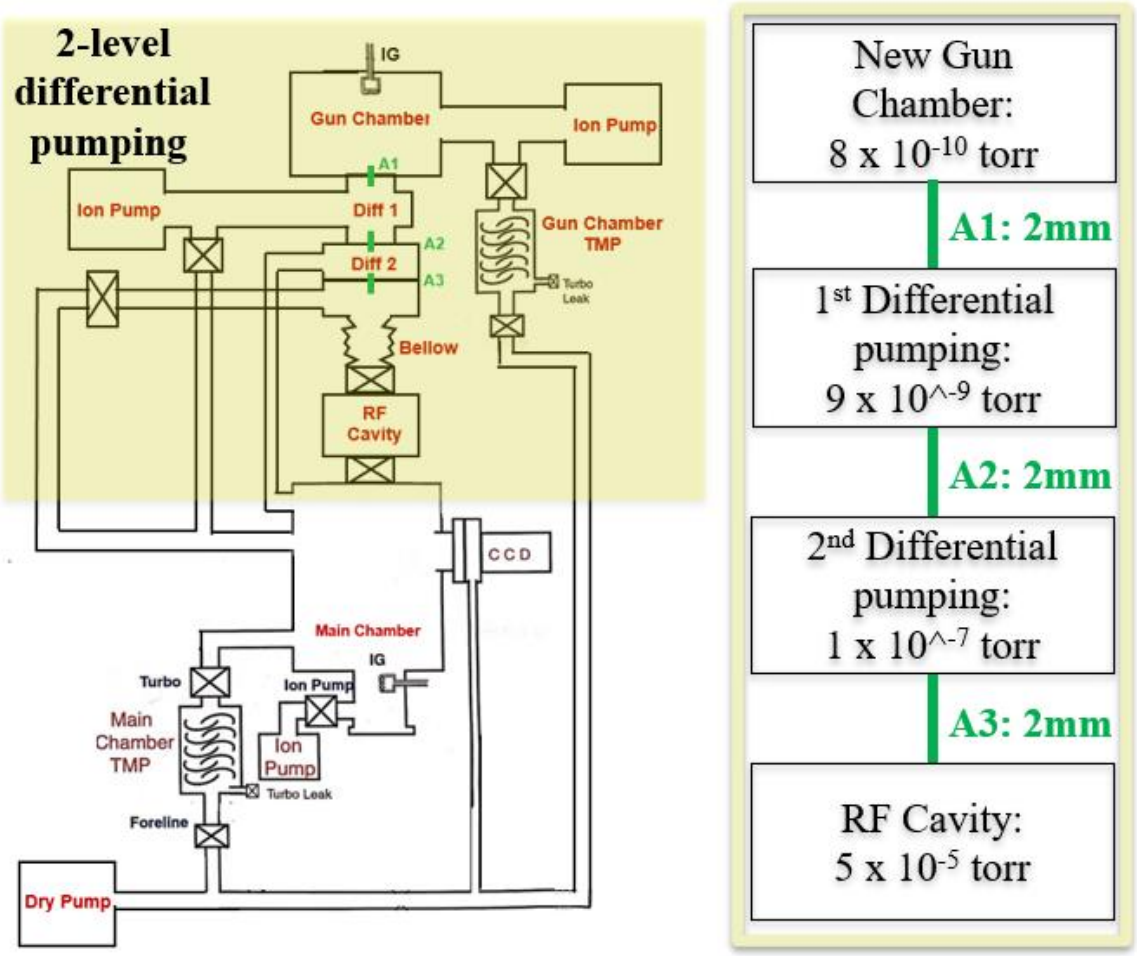

Figure 3.6 Vacuum diagram after UEC upgrade. The shaded area highlights the 2-level differential pumping design.

To achieve the desired beam size, a new lens pair was designed. For magnetic lenses with both upper and lower pole pieces, the focal length can be determined by the empirical electron lens making equation[14]:

$$\frac{f}{\sqrt{S^2+D^2}} = 31\frac{V}{(NI)^2} + 0.19 \tag{3.1}$$

where f is the focal length, S is the gap size between pole pieces, D is the diameter of pole pieces, V is the electron beam's accelerating voltage, I is the lens current, and N is the number of wire loops. To demagnify the beam by 10 times, the focal distances of the two lenses need to have a factor of 10. With this consideration, the lenses are designed with the parameters given in Table 3.1. A beam size of δ = 44 μm is achieved. The CAD model of the lens pair is shown in Fig. 3.7, and the comparison of beam size before and after the implementation of the lens pair is shown in Fig. 3.8.

	D(mm)	*S*(mm)	*N*	*I*(A)
Lens 1	1	1	200	0.85
Lens 2	1	1	500	1.15

Table 3.1 Parameter used in fabricating the lens pair system.

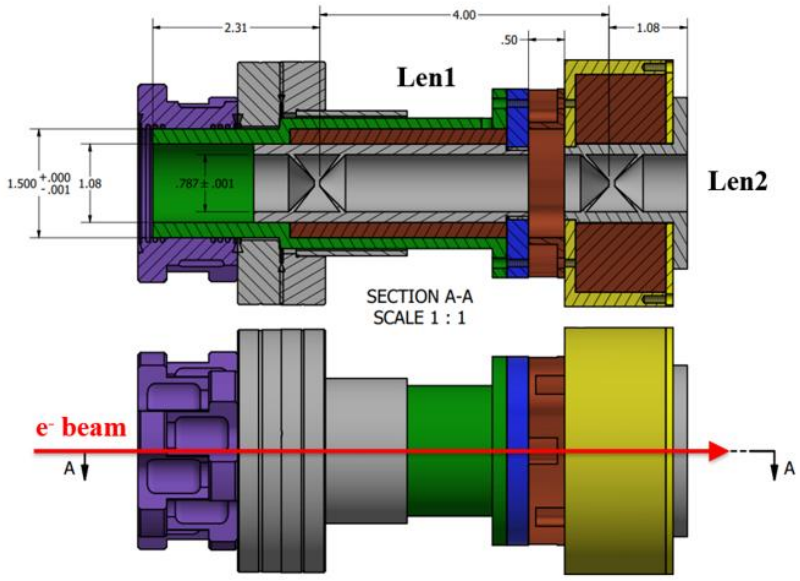

Figure 3.7 The Schematic of lens pair. Units are in inches.

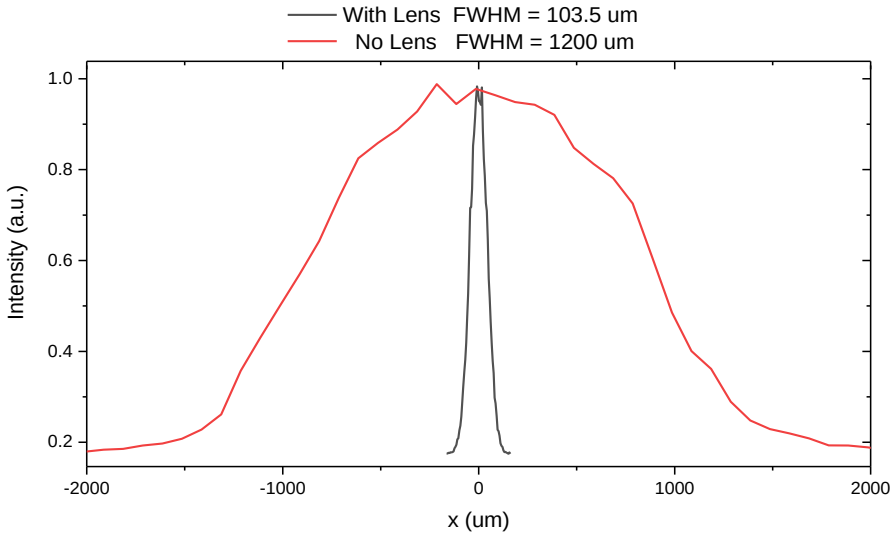

Figure 3.8 Beam profile at sample before and after turning on lenses. A reduction of 11.6 on electron beam size is achived.

After the upgrade, the temproal resolutoin of the UEC beamline is characterised via carring out the diffraction measurement for the suppression of NC-CDW in the TaS_2 system with 2 x 10^5 electron per pulse. The response curveds are obtained for different RF power to tune the system for best compression, which gives the response time of 250fs in sigma. Given the previous result from our group has shown the intrisic timescale for CDW suppression in TaS_2 is $\approx$ 300 – 400 fs(2σ), our measurement put the system's temporoal resolutoin to be $\leq$ 200fs in σ. We expect this result contains a sizable contribution from the RF noise in the compression optics, and the performace could be improved by implementing the new upgraded RF control system described in chapter 4.

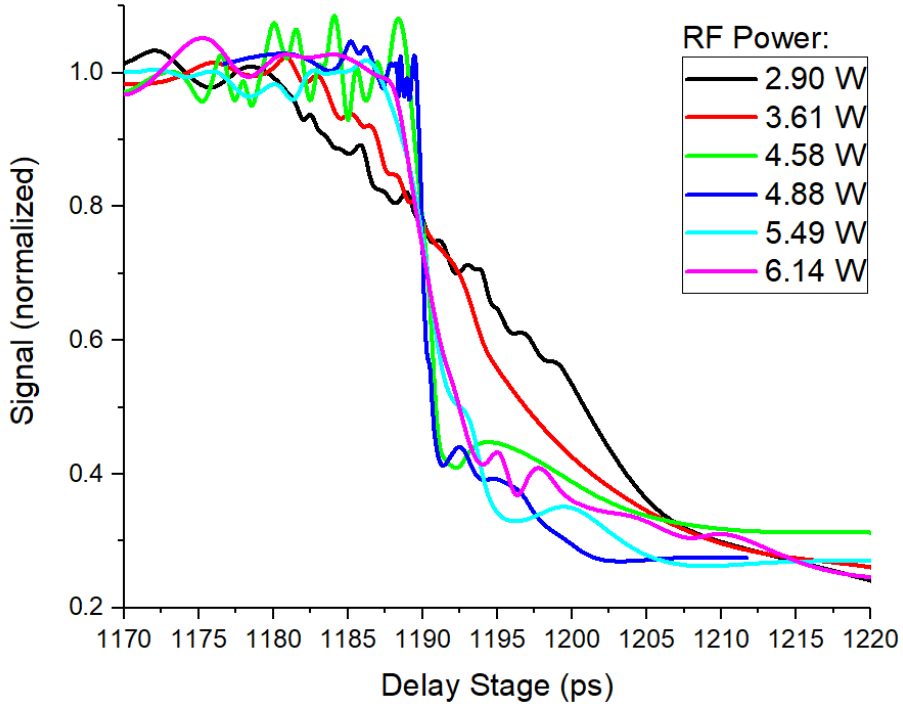

Figure 3.9. UEC's temprol resolution at different RF power. Measured dynamics of NC-CDW suppresion in TaS_2 system, best resolution is achived at RF power equal to 4.88W, where a temprol resolution σ = 200fs achieved.

3.3 Implementing the Dual Probe Setup in UEM System

Unlike the RF cavity, which was added later to the UEC system, the first-generation UEM (UEM-I) in Ruan group was initially built with the RF cavity and is the first RF-compressed UEM (RF-UEM). The overall design of the UEM-I beam delivery system includes the key components of the condenser system of a TEM, but adapted to accommodate the high-density beam delivery up to 10^7 electron per pulse generated from a Pierce-type photoemission gun; see Fig. 3.10.

Here the photocathode is driven by a front-illuminated 266 nm laser, and capable of a voltage bias up to -100 kV. The higher energy of the electrons results in a shorter wavelength, thus providing a higher penetration depth[9]. It also provides a larger (flatter) Ewald's sphere, which gives a better intersection with the reciprocal lattice of the material. The use of Pierce cathode[15] pushes the electric field between the cathode and anode focused toward the optical axis, providing a weakly converging electric equipotential to counter the beam divergence caused by space-charge effects. Similar to the UEC design, a gun lens (Lens 1) and a set of deflector rods are also attached to the gun.

Beyond the gun lens, two additional lenses are present in the system, where Lens 2 is before the RF cavity and Lens 3 is after the RF cavity and before the sample. The idea behind these two lenses is to demagnify the beam. Before the electrons enter Lens 3, an aperture assembly with three different sizes (50 μm, 100 μm, and 200 μm) is present. The choice of multiple aperture sizes allows us to select the low-dosage yet high-brightness

central part of the beam by using the smaller aperture or to obtain a higher dose at the sacrifice of brightness with a larger aperture . In addition to the deflector rod set next to the gun lens, a Helmholtz coil is placed immediately after it. The combination of the aforementioned deflector rod set and the Helmholtz coil ensures that the electron beam passes through the center of both Lens 2 and the RF cavity. Below the aperture assembly, a second set of deflector rods is present to ensure the electron beam passes through the center of Lens 3. After the beam passes through the sample, the data is collected by a camera assembly similar to the UEC setup. The setup of UEM-I is shown in Fig. 3.10.

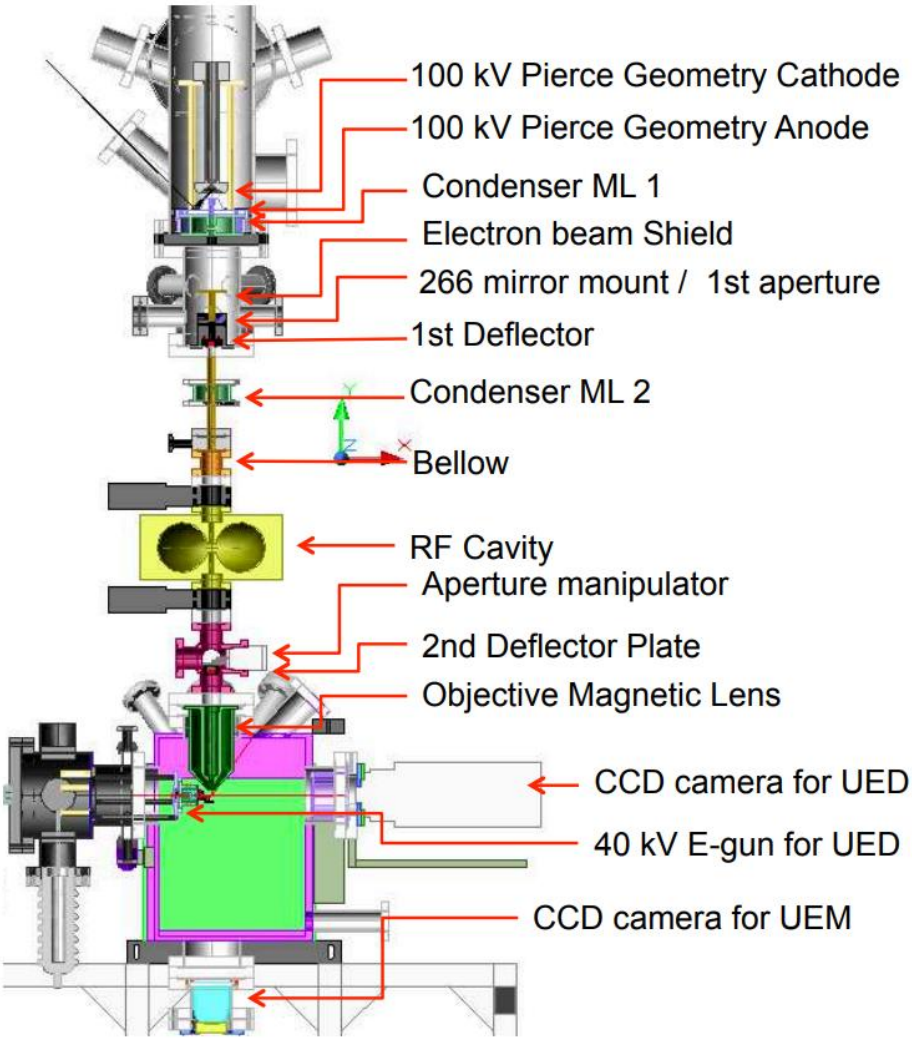

Figure 3.10. Schematic of 1st generation UTEM in Ruan group.

An upgrade was performed during my PhD tenure, where an 800 nm, 35 fs laser pulse was installed as a probe to track the probe optical transmittance change of the sample following the pump illumination. The optical signal was taken from the residue of the frequency tripler and passed through a delay stage such that the arrival time of the optical probe matched the arrival time of the electron probe within 100 fs. The optical probe then went through a 50/50 splitter, where the reflected beam served as a reference beam to track the intrinsic intensity fluctuations. Its signal was collected with a photodiode (Thorlabs DET10A) and then amplified by a boxcar (Stanford Research Systems SR250). The transmitted beam was sent to a telescope set, in which its size was expanded to $\sigma = 5$ mm. The expanded beam was then focused onto the sample inside the vacuum chamber with a size of $\sigma = 12.5$ μm. After the beam was transmitted through the sample, it was routed out to another photodiode (Thorlabs DET100A) and then followed by the same boxcar. The sample's transmittance change after photoexcitation was thus tracked by the signal change in boxcar output voltages: V(Boxcar #2) / V(Boxcar #1), as shown in Fig. 3.11.

The two photodiode-boxcar system served as a balanced detector, where their linearity between the input laser power versus the output voltage are first individually checked. In the balance detector setup, boxcar #1 served as the signal to track the laser induced transmittance change from sample, and boxcar #2 served as the reference to track the noise induced from laser power/position fluctuation. The linearity from the two photodiode-boxcar system guaranteed that any noise from laser is canceled by recording $\frac{V_{boxcarr\#1}}{V_{boxcarr\#2}}$. By implementing the balanced detector setup, the signal to noise ratio is improved by one order and a final signal to noise ratio better than 0.1% is achieved without the need of any average.

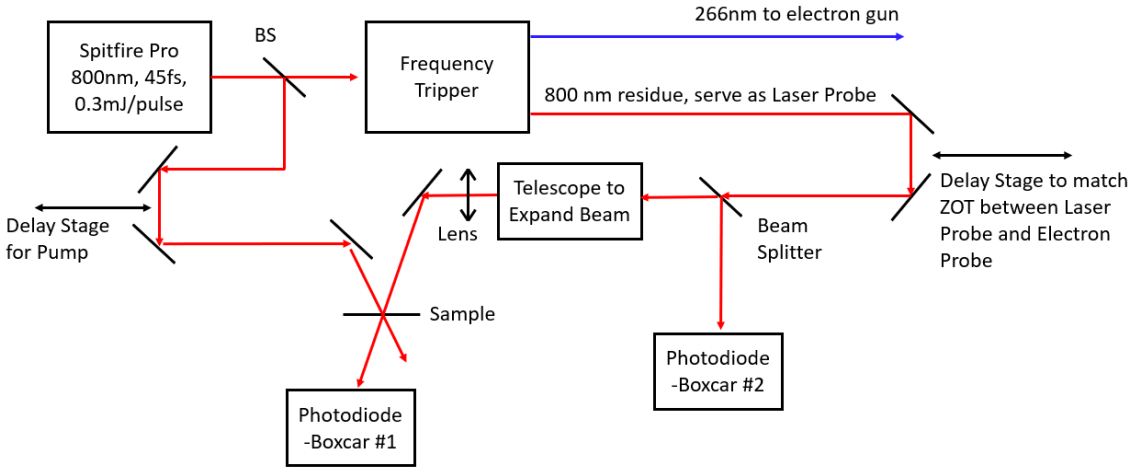

Figure 3.11 The setup of transmittance measurement. The optical probe is taken from the residue light of 800nm pulse after going through frequency tripler, the two photodiode-boxcar serve as a balance detector system to boost signal to noise ratio.

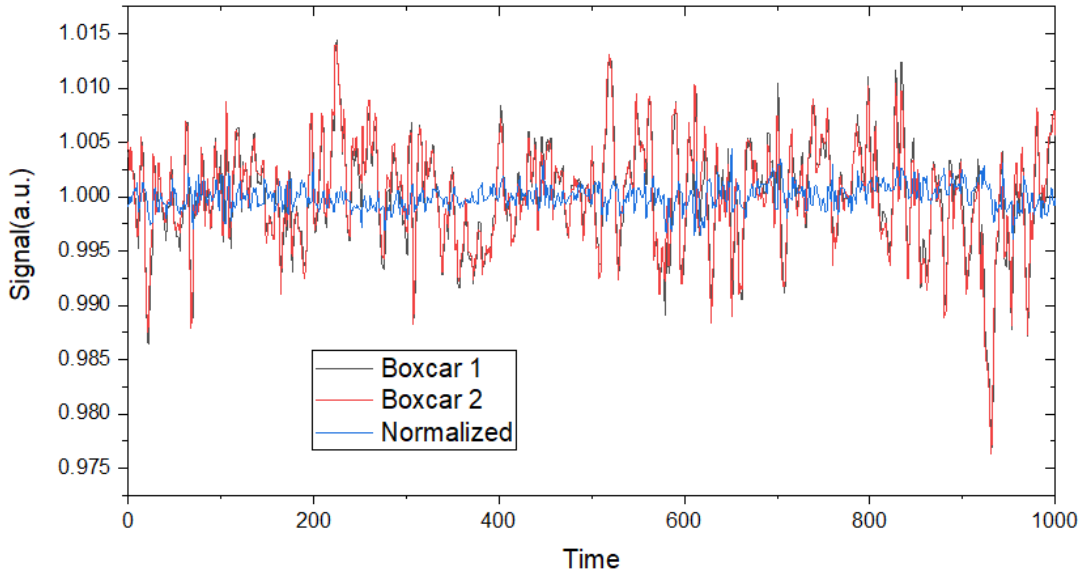

Figure 3.12 Balanced detector's performance. Black and red curved shows the raw recording from the two photodiode-boxcar system. The blue curve shows the normalized result, which is $\frac{V_{boxcarr\#1}}{V_{boxcarr\#2}}$. The signal to noise ratio increases by one order after normalization.

REFERENCES

REFERENCES

[1] A.H. Zewail, “Four-dimensional electron microscopy,” Science (1979) **328**(5975), 187–193 (2010).

[2] A. Feist, N. Bach, N.R. da Silva, T. Danz, M. Möller, K.E. Priebe, T. Domröse, J.G. Gatzmann, S. Rost, and J. Schauss, “Ultrafast transmission electron microscopy using a laser-driven field emitter: Femtosecond resolution with a high coherence electron beam,” Ultramicroscopy **176**, 63–73 (2017).

[3] S. Sun, X. Sun, J. Williams, and C.-Y. Ruan, “Development of RF-compressed high-throughput femtosecond electron microscope,” Microscopy and Microanalysis **26**(S2), 430–433 (2020).

[4] C. Zhu, D. Zheng, H. Wang, M. Zhang, Z. Li, S. Sun, P. Xu, H. Tian, Z. Li, and H. Yang, “Development of analytical ultrafast transmission electron microscopy based on laser-driven Schottky field emission,” Ultramicroscopy **209**, 112887 (2020).

[5] J. Williams, F. Zhou, T. Sun, Z. Tao, K. Chang, K. Makino, M. Berz, P.M. Duxbury, and C.-Y. Ruan, “Active control of bright electron beams with RF optics for femtosecond microscopy,” Structural Dynamics **4**(4), (2017).

[6] V.A. Lobastov, R. Srinivasan, and A.H. Zewail, “Four-dimensional ultrafast electron microscopy,” Proceedings of the National Academy of Sciences **102**(20), 7069–7073 (2005).

[7] A.H. Zewail, “Four-dimensional electron microscopy,” Science (1979) **328**(5975), 187–193 (2010).

[8] S. Sun, X. Sun, D. Bartles, E. Wozniak, J. Williams, P. Zhang, and C.-Y. Ruan, “Direct imaging of plasma waves using ultrafast electron microscopy,” Structural Dynamics **7**(6), (2020).

[9] D.B. Williams, C.B. Carter, D.B. Williams, and C.B. Carter, *The Transmission Electron Microscope* (Springer, 1996).

[10] C.-Y. Ruan, Y. Murooka, R.K. Raman, R.A. Murdick, R.J. Worhatch, and A. Pell, “The development and applications of ultrafast electron nanocrystallography,” Microscopy and Microanalysis **15**(4), 323–337 (2009).

[11] C.-Y. Ruan, Y. Murooka, R.K. Raman, and R.A. Murdick, “Dynamics of size-selected gold nanoparticles studied by ultrafast electron nanocrystallography,” Nano Lett **7**(5), 1290–1296 (2007).

[12] J.A. Berger, J.T. Hogan, M.J. Greco, W.A. Schroeder, A.W. Nicholls, and N.D. Browning, “DC photoelectron gun parameters for ultrafast electron microscopy,” Microscopy and Microanalysis **15**(4), 298–313 (2009).

[13] R.K. Raman, *Electronically Induced Structure Transformations in Graphite & Silver, Studied Using Ultrafast Electron Crystallography* (Michigan State University, 2010).

[14] A. El-Kareh, *Electron Beams, Lenses, and Optics* (Elsevier, 2012).

[15] J.R.M. Vaughan, "Synthesis of the Pierce gun," IEEE Trans Electron Devices **28**(1), 37–41 (1981).

Chapter 4

Radio-Frequency Electron Pulse Compression

In the realm of ultrafast measurements, the quest for higher temporal resolution is central. Unlike ultrafast optical techniques, where increasing the photon dose typically does not degrade the performance, electrons, being negatively charged, can adversely affect the measurement when packed at high densities. This phenomenon, known as the space-charge effect, occurs due to the particle-particle Coulomb repulsion, which can significantly impact the performance of ultrafast electron-based measurements[1–4].

Several strategies have been proposed to enhance temporal resolution. These include reducing the travel time of electrons by either escalating the accelerating voltage to the MeV[5–9] level or reducing the distance[10–12] between the cathode and the sample to centimeters range. However, designing electron optics for MeV electron beams presents a challenge, and a short distance between the cathode and the sample precludes the use of complex electron optics prior to the sample.

An alternative approach involves reducing the electron count to less than one electron per pulse[13–15]. Although this method effectively eliminates the space charge effect, it necessitates a high repetition rate (typically 1 – 100 MHz) to compensate for the loss of dosage, thereby limiting the scope of material process that can be studied to those fully reversible within the pump-probe period.

At MSU, we employ an RF cavity as a longitudinal lens to actively compress the beam pulse[3]. During my Ph.D., a new cascade RF control system is being developed. In this chapter, I will first introduce the principles behind RF compression, followed by a discussion on the

construction of the cascade RF control system, and finally, an examination of how the new RF system enhances temporal resolution.

4.1 Basic RF Field Compression Mechanism

In this section, I will introduce the formalism to consider the mechanism for adjusting the electron pulse phase space structure, leading to compress the pulse duration. To understand how RF field interacts with the electron pulse, we start by considering a single electron pulse in the RF field. The RF field and the change of momentum of the electron is given by:

$$E = E_0 * \sin(\omega t + \phi_0), \tag{4.1}$$

and

$$\Delta p = F\,\Delta t = -\int_{t1}^{t2} e\,E(t)\,dt, \tag{4.2}$$

where Δt is the time of electron interact with the RF field, determined by the gap, *d*, of the RF cavity. Take t = 0 when the electron passes through the center of the RF cavity, we have:

$$t1 = -\frac{d}{2v} \text{ and } t2 = -\frac{d}{2v}, \tag{4.3}$$

where v is the velocity of the electron. Eq 4.2 then can becomes:

$$\Delta p = -2\frac{e\,E_0}{\omega} * sin\left(\frac{\omega\,d}{2v}\right) sin\,\phi, \tag{4.4}$$

and the velocity change is:

$$\Delta v = \frac{\Delta p}{m\,\gamma^3} = -2\frac{e\,E_0}{m\,\gamma^3\,\pi\,f} * sin\left(\frac{\pi\,f\,d}{v}\right) sin\,\phi. \tag{4.5}$$

The arriving time jitter, caused by a noise RF source (i.e. ϕ_0 is not stable) is then:

$$dt = -\frac{L}{v^2}\,d(\Delta v) = -2\frac{\mathrm{e}\,E_0}{m\,\gamma^3\,\pi\,f} * \sin\left(\frac{\pi\,f\,d}{v}\right)\cos\phi\,d\phi. \tag{4.6}$$

Equation 4.2 gives us the relationship between the arriving time jitter and RF phase jitter, it is calculated without considering the internal charge distribution of the electron pulse. We can see that the time jitter is proportional to the phase jitter. Next, I will show how the RF filed compress the electron beam.

We begin by defining the velocity spread and position spread being δv and δz, before entering the RF cavity. The chirp of the pulse is then defined as:

$$a_0 = \frac{\delta v}{\delta z}. \tag{4.7}$$

There are two specific cases to be considered, the first case is when the pulse arrives at the sample, $\delta z' = 0$ such that the pulse has a shortest width, or best temporal resolution. The phase space chirp change is illustrated in Fig. 4.1. In order to have $\delta z' = 0$ at sample, we must have a negative chirp after the pulse get out of the RF cavity, satisfy the condition:

$$t = \frac{L}{v} = \frac{\delta z}{-\delta v'}, \tag{4.8}$$

which gives the chirp after RF field:

$$a' = \frac{\delta v'}{\delta z} = \frac{v}{L}, \tag{4.9}$$

only depends on the geometry of the instrument setting. To achieve a best imaging quality (for a lesser effect, also on a better diffraction quality), a minimized energy spread beam is desired, it is evident in that case, $a' = 0$.

We can write the change of RF phase due to the finite electron pulse width as:

$$\delta\phi = 2\,\pi\, f\, \tau = 2\,\pi\, f \frac{\delta z}{v}, \tag{4.10}$$

where τ is the pulse duration of electron beam, and f is the frequency of the RF wave. This gives us the change of chirp after electron beam passing through RF cavity as:

$$\Delta a = \frac{\delta \Delta v}{\delta z} = 2\,\pi\, f \frac{\delta \Delta v}{v\, \delta\phi}. \tag{4.11}$$

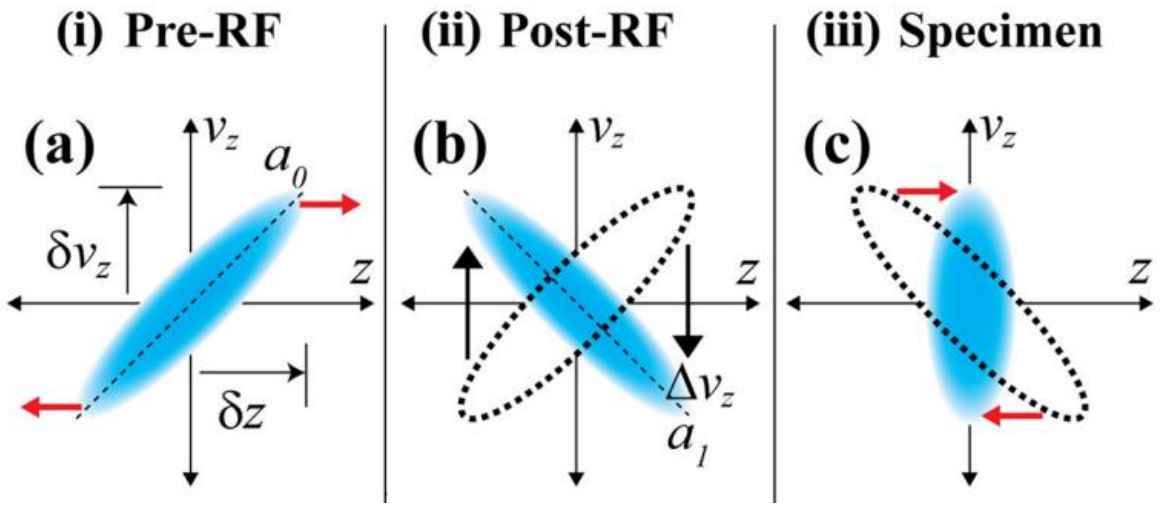

Figure 4.1. Phase space illustration of RF compression on electron beam. The electron beam's phase space **a.** before entering the RF cavity. **b.** after passing through the RF cavity, and **c.** at the sample. Adapted from Ref.[3]

We define focusing parameter η, defined by the beam velocity change $\delta\Delta$v observed under an RF phase tuning ($\delta\phi$):

$$\eta \equiv -\frac{1}{v}\frac{\delta \Delta v}{\delta \phi} = -\frac{1}{2\,\pi\, f}\,\Delta a, \tag{4.12}$$

with the help of Eq. 4.5, we have:

$$\eta = \frac{\mathrm{e}\,E_0}{m\,\gamma^3\,\pi\,f\,\mathrm{v}}\sin\left(\frac{\pi\, f\, d}{v}\right)\cos\phi, \tag{4.13}$$

and we can re-write Eq. 4.6 into:

$$dt = -\frac{L}{v}\,\eta\, d\phi. \tag{4.14}$$

Similarly, the beam energy change due to phase jitter can be re-write from eq.4.4:

$$dK = m\, v^2\, \gamma^3 \eta\, d\phi. \tag{4.15}$$

Eq. 4.12 and 4.13 give us the condition of how to best set the field to optimally compress the pulse. Fig. 4.2 show the RF field led to pulse compression over two different regimes of photo electron generation.

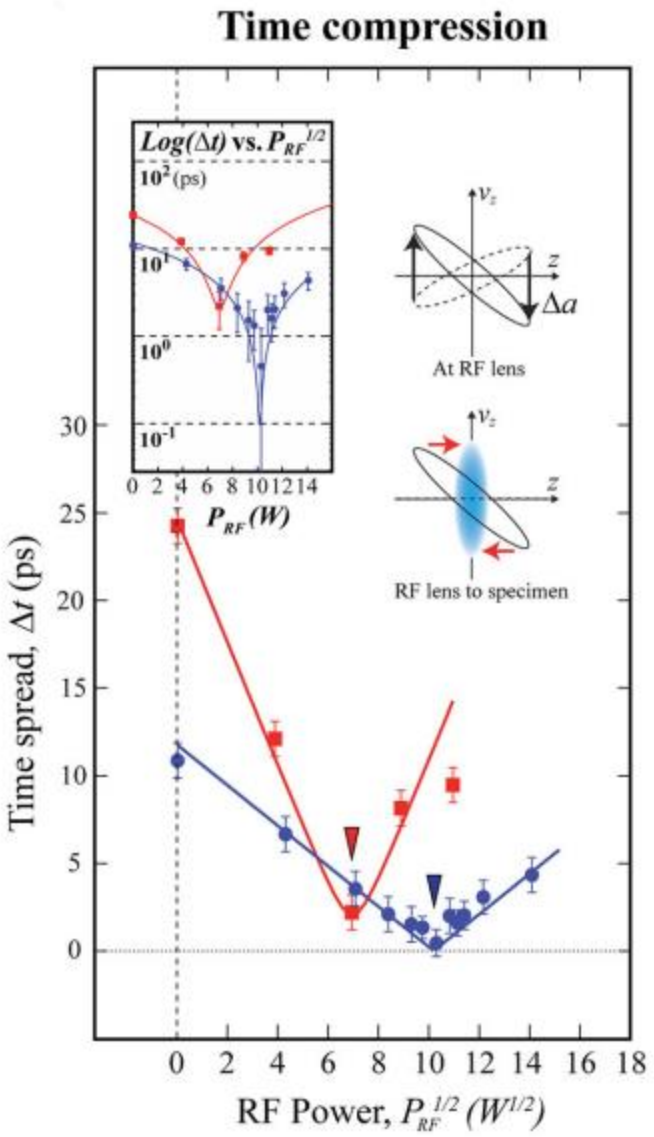

Fig. 4.2. Pulse duration change as a function of supplied RF power. The red data is gathered from 10nm cathode with 1.7 x 10^7 electron per pulse, which is beyond VCL. The blue data is gathered from 50nm thick cathode with 1 x 10^6 electron per pulse, which is below VCL. The difference between the two RF power required indicate a difference chirp before the electron pulse. The difference between the minimum possible compressed pulse width is due to the size difference of the phase space emittance. Adapted from Ref.[3]

The shortest pulse duration is reached when η ((experimentally usually measured as square root of the RF power) reached an optimal value where the chirp change Δa it introduces perfectly cancels our the initial chirp a_0. With the operating η determined by following Eq. 4.14, one can tune the pulse energy and arriving time by changing the RF phase and amplitude. thru perfection such RF control over delivered electron pulse, one can evaluate other limiting factors for the time resolution given under for a specific a beam does. The above discussion best applies to the case where the intrinsic area of phase space is zero. However, in practice, the phase space has a finite area, so-called emittance, as schematically drawn in the shape of a tilted eclipse in the Fig. 4.2 insert. One important factor that affects the emittance is the intensity of the drive laser. As the drive laser intensity increases, the emittance will increase, resulting in an upshift in the optimally compressed pulse width. On the other hand, the more favorable sublinear scaling in transverse emittance over Ne resulting an increase of brightness, which gives a better signal to noise ratio (S/N). It is previously found this favorable scaling holds true until the virtual cathode limit (VCL) is reached[16]. In experiment, the balance between short temporal and good S/N need to be carefully considered, which usually is chosen by placing the drive laser intensity just below the VCL. More detailed discussion can be found in Ref[3]and Ref[4].

4.2 RF Cavity as a Condenser Lens in UEM System

In the previous sections, I have shown that the RF field can effectively adjust the phase-space structure of the electron pulse to reach condition for either compress the pulse duration of energy spread. In the UEM system, those two configurations correspond to the case where the best temporal resolution and the best imaging resolution are accomplished. However, the lens employed in the UEM system is not perfect.

To evaluate the impact, we look at the coupling between the phase space (which is considered as a stochastically filled area) and the optical transfer function in the context of the objective aberration function. To illustrate the theoretical principles, we first ignore contributions from a noisy RF source. We trace the effects of a finite-sized electron bunch phase space on the TEM's resolution function. In this phase-space-

based picture, the beam's incoherent illumination causes information loss and degrades resolution, which can traced to two parts[17]: $E_S(k)$ from the special incoherence, and $E_T(k)$ from the energy incoherence. They are both expressed in the Fourier spatial frequency k. As part of the (objective) lens transfer function[18], these incoherence envelopes restrict the information at high k, given by:

$$t(k) = E_s(k)E_T(k)e^{i\chi(k)}, \tag{4.16}$$

where $\chi(k)$ gives the phase factor of the distorted wavefront. The envelope functions are given by:

$$E_s(k) = \exp\{-[\pi\sigma_s(C_S\lambda^2k^3)]^2\}, \tag{4.17}$$

$$E_s(k) = \exp\{-0.5[\pi\sigma_T(C_S\lambda k^2)]^2\}, \tag{4.18}$$

where λ is the electron de Broglie wavelength. The direct impact from the incoherence phase-space envelope is seen in the coupling between the exponent σ_s (the RMS of the beam convergence angle) and the spherical aberration coefficient C_S. This results in an expanded cone of incoherent illumination. Namely, a large transverse emittance size ε_x will propagate into a large transverse extremum size through focusability. The spatial resolution (R_0) or the coherence length (X_c) from the bunch illumination is thus expected to be limited. Meanwhile, taking the temporal incoherence envelope into consideration, σ_T is defined by:

$$\sigma_T = [(\frac{\sigma_E}{E_0})^2 + (2\frac{\sigma_I}{I_0})^2]^{1/2}, \tag{4.19}$$

where σ_E and σ_I are the RMS deviations of the beam energy (E_0) and objective lens current (I_0), respectively. These couple to the lens chromatic aberration coefficient C_c. The expanded σ_T limits the spatial resolution due to the cross-dimensional effect; namely, beam temporal incoherence causes imprecision in spatial focusing. It is easy to see that instability of the RF optics will couple to the lens optics through an increase in σ_T. Hence, an imprecise RF lens not only causes a loss in temporal resolution but also directly impacts the spatial resolution in an ultrafast electron microscope (UEM). The resolution loss is given by the complementarity (Fourier-pair) relation between the resolution function R(r) and the transfer function t(k)[19]:

$$R(r) = FFT[\![t(k)]\!]. \tag{4.20}$$

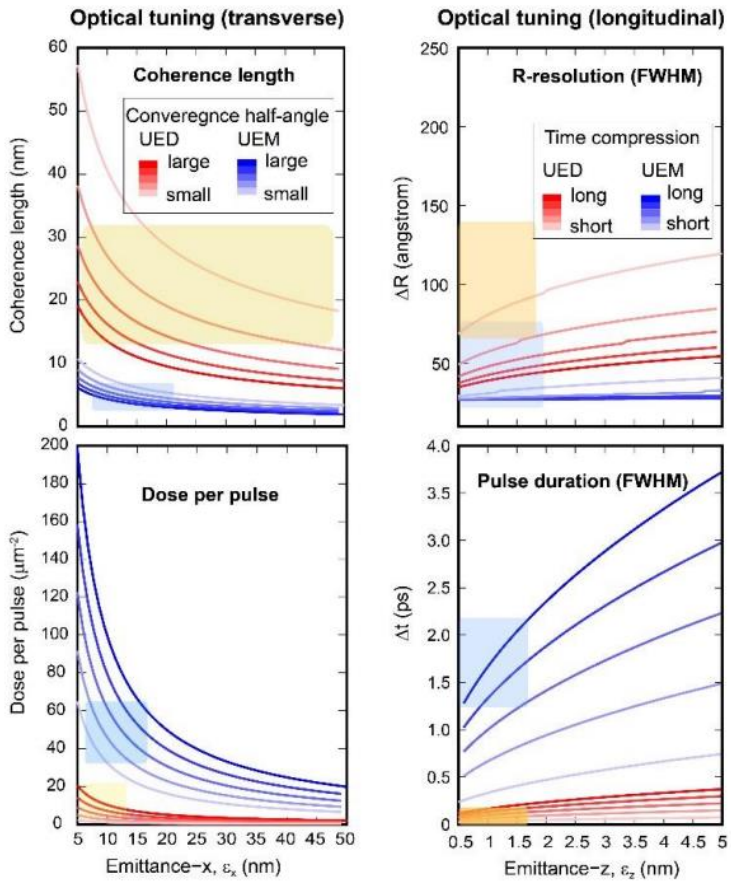

Figure 4.3. UEM and UED performance from tuning the condenser system. To evaluate the effect on the focusing property, the results are given for different transverse and longitudinal emittances. The model considers a beam energy of 60 keV with 10^5 electrons. The UED and UEM categories are classified based on the strength of RF filed applied, where a stronger RF field is applied to UED to prioritize the time resolution, while a weaker RF field is applied to UEM to prioritize the spatial resolution. The pulse duration Δt is set from 250 to 750 fs (FWHM) at low emittance for UEM. For UED, the Δt setting is smaller, ranging from 25 to 75 fs at low ε_z. For UEM, the convergence half-angle is varied from 0.6 to 3.5 milliradians, subject to the demagnification of the beam by the condensers acting as a virtual source at the front focal distance of the objective pre-field. This angle depends on the transverse emittance ε_x, the condenser settings, and the pre-field focal distance (which is 1.4 mm to match with experiment). For UED, this angle is smaller, ranging from 0.1 to 1.1 milliradians. The microscope resolution function from the derivation of ΔR is calculated using the lens aberration coefficients C_s = 1 mm and C_c = 1.9 mm. Adapted from Ref. [20]

Eq.4.19 gives TEM's resolution as a function of both the transverse and longitudinal phase space emittance. It is important to note that the energy spread (σ_E) is inverse related to the beam pulse width coupled via the RF compression. Similarly, the convergent angle (determines σ_s) is inverse related to the dosage coupled via the magnetic lens focusing. Thus, in experiment, one cannot simply set σ_E and $\sigma_s = 0$, in which will corresponding to a mono-kinetic electron beam but with a long pulse width, and a coherent parallel beam with weak intensity.

In Fig. 4.3, we present the modeled results UEM and UED modalities. The categorization of UED and UEM modalities is based on the starting values of the tuning parameters. As these parameters are varied, performance in ultrafast diffraction and imaging may be prioritized. However, regimes can be approached where UED and UEM experiments are carried out at similar optical settings - enabling a joint multi-modal scheme under the same beam illumination condition, but with some compromises in resolution from each channel.

For UEM modality, the primary goal is to optimize spatial resolution R. This involves setting a larger convergence half-angle to promote dose over coherence length and prioritizing high temporal coherence over temporal resolution to reach sub-10nm spatial resolution. For UED mode, the system prioritizes higher coherence length Xc and shorter pulse width. Consequently, the dose and direct-space resolution may suffer compared to UEM mode.

The divergent trends from these simulations over the emittance provide guidance, based on the desired UED and UEM performance, for setting bounds on the emittance size. The shaded areas represent previous experimental spans for operating the RF beamline under UED[21] and UEM[22,23] modalities (see Fig. 4.3). While only providing order-of-magnitude precision on beam emittance, the assigned characteristic emittance is consistent with the source emittance given by multi-level fast multipole method simulations optimized for the laminar flow regime.

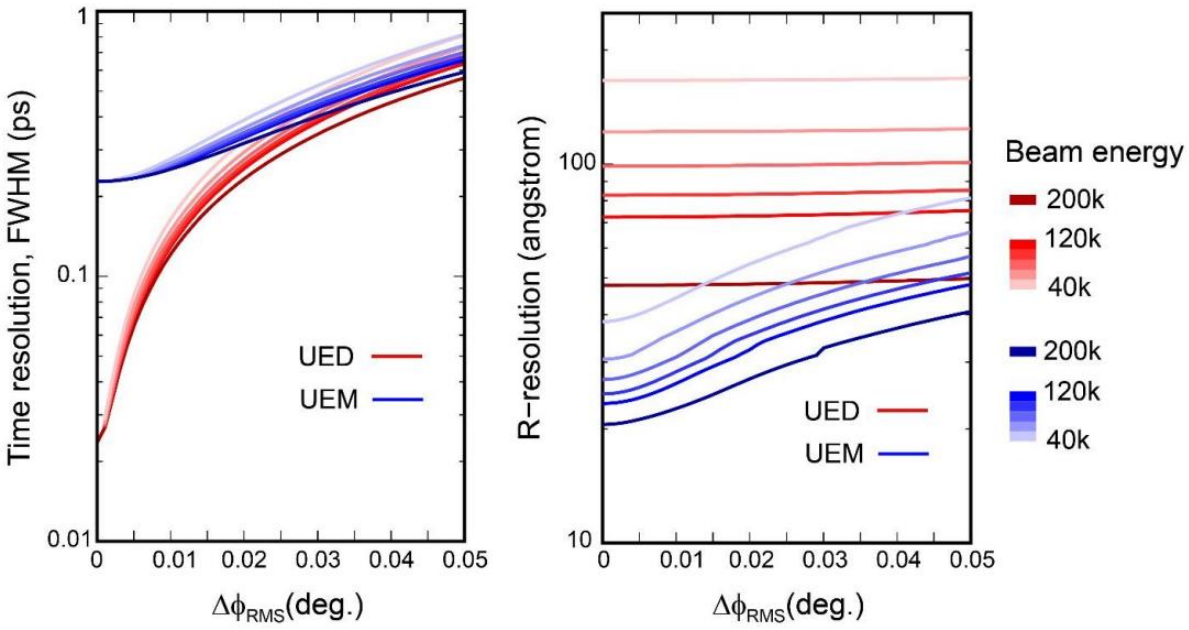

Figure 4.4. The impacts from the RF instabilities on the temporal and spatial resolutions. The left panel gives the temporal resolution for UEM and UED modalities modelled for the nominal values of ε_x =10 nm and ε_z =1 nm for Ne=10^5. The results are calculated for the beam energy varied from 40 to 120 keV and 200keV. The right panel gives the corresponding changes in the imaging resolution. The different RF optical settings for UED and UEM reflect different phase-space aspect ratio prioritized for either imaging or ultrafast diffraction. For imaging the energy spread is 0.3 eV to allow for sub-10 nm imaging resolution, while for UED it increases to 250 eV to give the best possible temporal resolution set by the emittance floor. The impact on temporal resolution is largest in UED mode due to strong focusing. Based on the simulation, it is possible to compress the bunch down to 22 fs FWHM, which only weakly depends on beam energy. This weak dependence can be seen in the time-to-phase ratio $k_{t\phi}$ = L/v. For our setups with L $\approx$ 0.4 m, $k_{t\phi}$ of 4 to 4.5 is estimated for beam energies from 40 to 100 keV. Meanwhile, the impact on UEM lies in the spatial resolution (right panel of Fig. 4.4). Adapted from Ref. [20]

We now add the effects of a noisy RF source feeding the RF cavity longitudinal lens on the resolution. The effect of RF jitter on beam energy change and arrival time change is given in equations 4.14 and 4.15. Based on the nominal emittance deduced for 10^5 electrons (Fig.4.3), and the RF lens settings where f = 1.013 GHz, d = 2.1 cm, the incoherence envelopes is then calculated.

The additional temporal incoherence from the RF cavity phase jitter $d\phi$ is convolved into the overall incoherence width by $\sigma_{T'} = (\sigma_T{}^2 + dK^2)^{1/2}$, from which we determine the spatial resolution. The results for different beam energies are presented in Fig. 4.4.

The high sensitivity to RF noise at the fs-nm scale measurements is quite noticeable, highlighting the importance of further improving the phase stability of the RF system. To test the emittance floor based on the given $k_{t\phi}$ in both scenarios, an RMS noise close to 0.005° would be required.

4.3 Upgrade of the RF Control System

While the core magnetic and RF condenser lens technologies promise to deliver a bright beam with sub-100 fs temporal resolution (e.g. the 22 fs FWHM simulation in Fig. 4.4), translating such short bunches to actual performance requires high stability and precision in the control system. For UEM systems, synchronization between the laser pump and the RF system seeding the RF cavity is achieved through a phase-locked loop (PLL) circuit (Fig. 4.5). This consists of a photodiode converting the laser oscillator light pulse to a multi-GHz frequency comb, with the RF cavity resonance at 1.013 GHz locked to an integer harmonic.

Over the extensive distances the signals travel, the success of the RF phase-locked loop depends on identifying and removing spurious noise sources, often involving proportional-integral-derivative (PID) feedback control loops over the appropriate experiment timescales. Effective feedback control strategies have been reported achieving ~80 fs temporal resolution for relativistic UEM[7,24,25] beams and ~100 fs for sub-relativistic UEM systems[3,26–29]. However, the actual performance deviates between systems due to

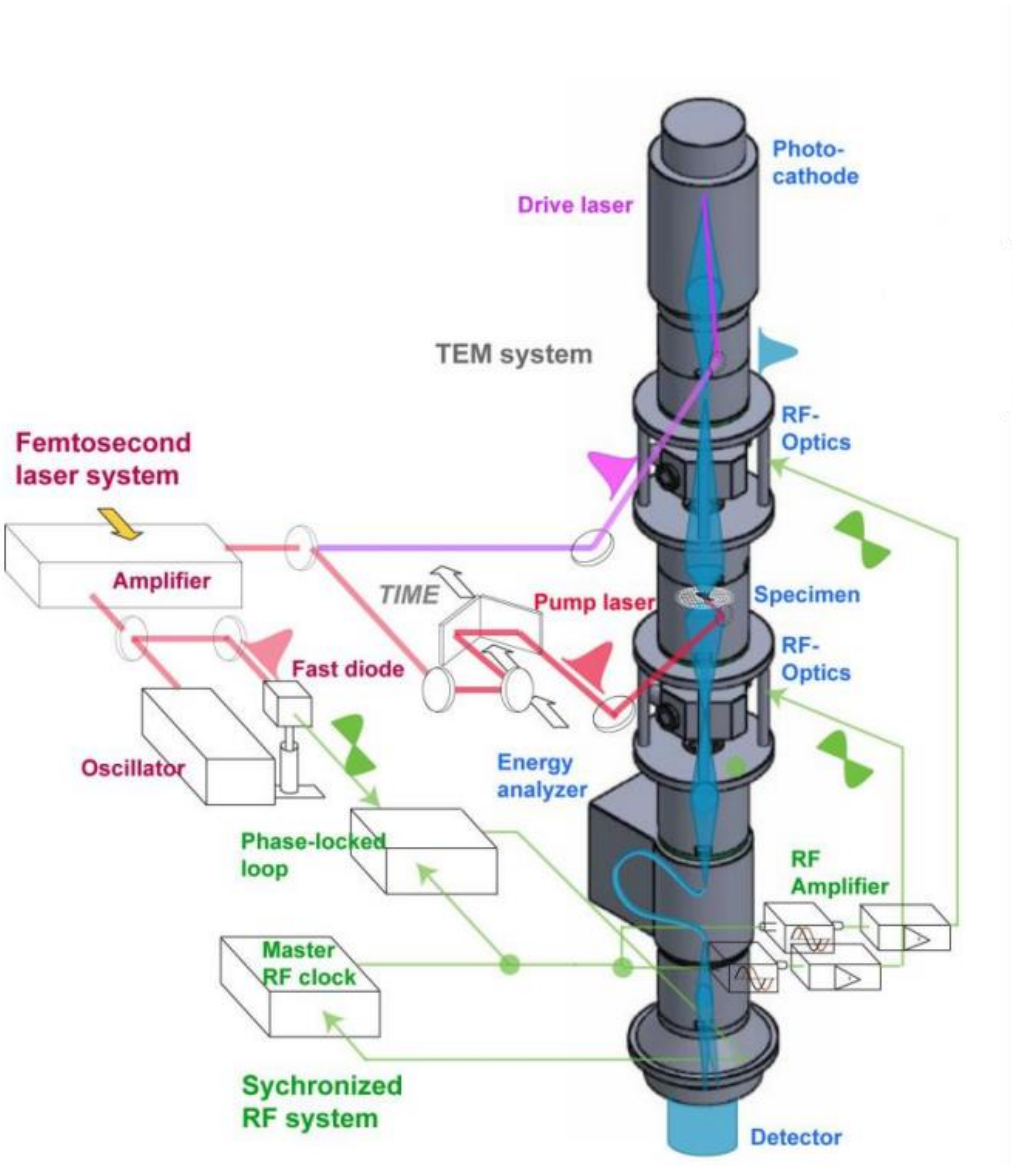

Fig. 4.5. A typical integration between Laser, RF system, and UEM electron optics. The fs laser system provides timing to pump pulse initiating material transformation as well as for seeding the RF signals sent to the RF cavity that delivers the short electron probe pulses. A PLL serves to ensure laser and RF are synchronized to each other. Adapted from Ref.[30]

varying beamline designs and specific noise sources present at each location. To deliver and uphold the ~22 fs FWHM bunch predicted by simulation, further improving on phase stability and precision control of the RF systems beyond what current design is needed.

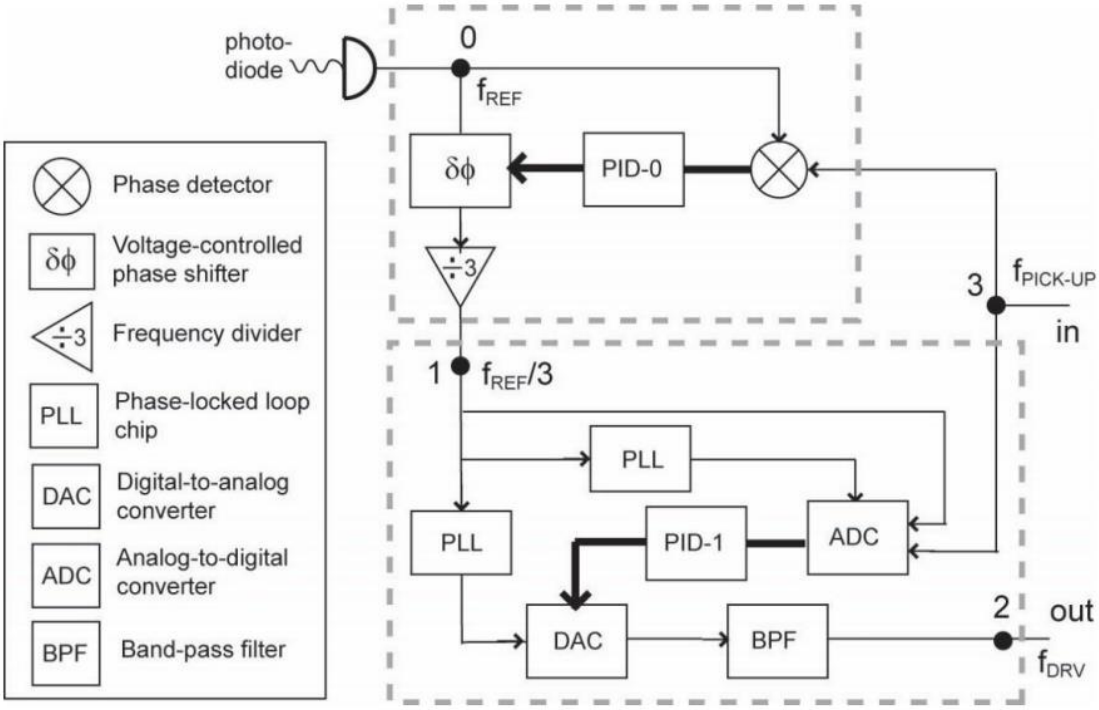

Figure 4.6. Circuit schematics for the two-level PID system for RF phase control and noise suppression. f_{REF} is the reference frequency selected from the frequency comb of the laser, used as the reference frequency for the RF system. f_{DRV} is the driving frequency sent to the RF cavity that compresses the electron beam. f_{REF} is the frequency of signals at the pickup port. Adapted from Ref. [20]

A cascade scheme RF control system is designed to reduce noise level to 0.005° RMS, providing sufficient precision for focusing the bunch down to the emittance floor. The new scheme features a two-level cascade design, as illustrated in Fig. 4.6. The master feedback loop, PID-0, oversees the entire length of the RF circuit, compensating for the phase difference, $\Delta\phi$, measured between the laser frontend and the

RF pickup port; its output for phase compensation is fed into the PID-1 subsystem. The PID-0 feedback control employs a 4 MHz digitizer, averaging over 1k samples to achieve the necessary phase detection precision for running the PID. With a sub-millisecond detection time, the system can detect noise spectrum beyond 1 kHz, yet it operates at 10 Hz to provide the overall phase stability required for long-term operation. The nested feedback loops detect and compensate for active noise sources over their respective detectable spectral ranges. Specifically, the PID-1 inner loop, which operates at a higher frequency and is proximity-coupled to the UEM column, employs a digital phase-locked loop (PLL) to address local phase noise. This noise is measured between the signal fed into the low-level RF (LLRF) controller and the signal at the cavity pickup port. The high-speed LLRF controller, designed and fabricated by the RF group at the Facility for Rare Isotope Beams (FRIB), supports the new 644 MHz superconducting cavity for the future FRIB400 upgrade and the 1.013 GHz room-temperature UEM cavity. A key feature of this LLRF controller is the System-on-Chip (SoC) field programmable gate array (FPGA) design, which incorporates fast data converters that allow direct sampling at 1.013 GHz and PLL chips with good phase noise performance up to 100 kHz. These PLL chips generate clocks for the data converters and FPGA. Consequently, the LLRF controller can effectively suppress any local phase noise within the cavity bandwidth, which is much greater than 0.1 MHz.

Importantly, the cascade loop design can synergistically reduce the noise floor while ensuring long-term stability through a shared responsibility spectrum region for joint optimization. This spectral region is allocated in the most active frequency domain, from 10 Hz to 1 kHz. To inspect this effect, noise spectrum analyses are first carried out at different levels of feedback controls by the two PID sub-systems. The results are presented in Fig. 4.7, first showing the scenario of open loops. In this free-running scenario, the intrinsic noise spectrum given by the PID-1 sub-loop carries an accumulated RMS noise of 0.013 from 1 Hz to 10^6 Hz (in green). Meanwhile, the phase noise detected in the master loop rises to 0.039 RMS from 10^{-6} Hz to 10 Hz (in pink). The corresponding noise power spectra are presented in the inset panels below, showing temporal correlations with the characteristics of a power-law distribution. The synergistic effect is then investigated by running the two PID control loops simultaneously, with the set parameters used in PID-0

optimized for overall performance improvement viewed from $\Delta\phi$, necessarily encompassing the increased noise from the active PID-1 sub-loop for reducing high-frequency noises. At this stage of implementation, only the PID-0 parameters are tuned.

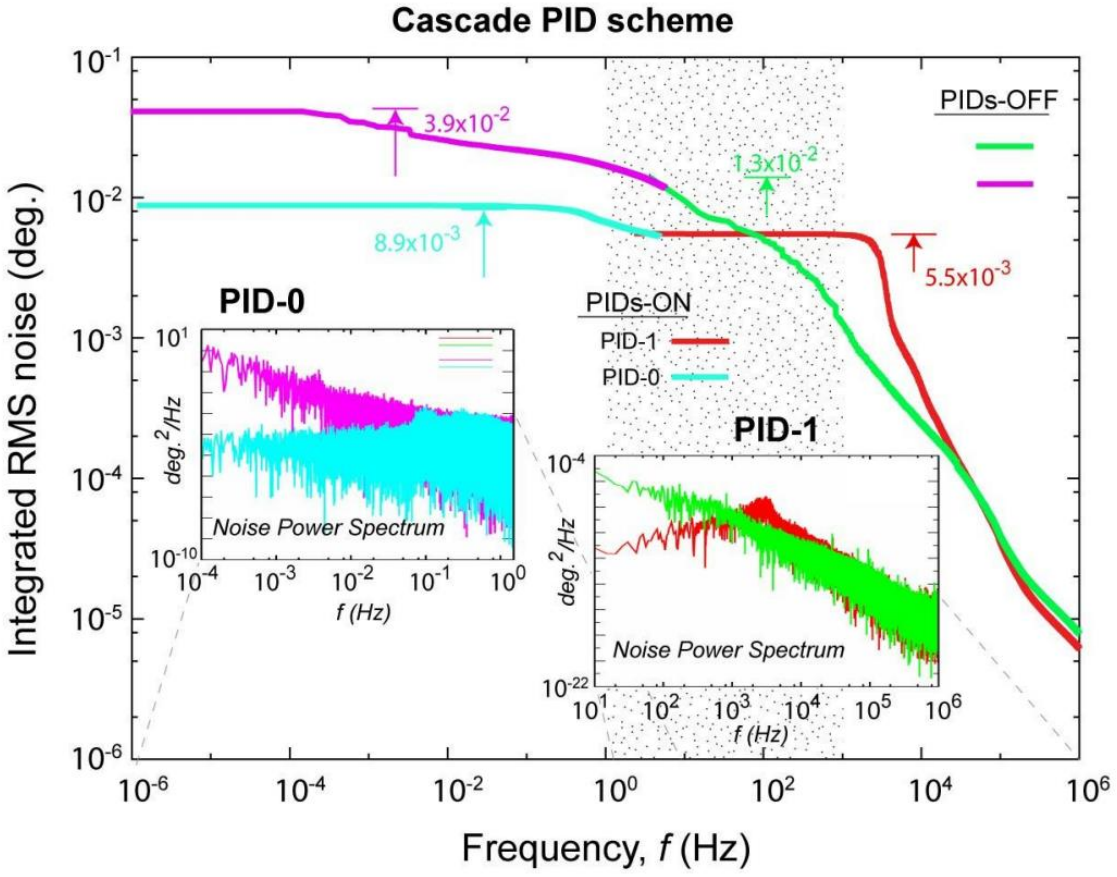

Figure 4.7. RF noise characterizations before and after applying PID feedback controls. The main panel shows the integrated RMS noise measured from PID-1 & PID-0 loops separately, the performance with active PID correct and without PID correct are compared. The inserts show the corresponding noise power spectrum plotted with the same color code. The dotted area represents the shared responsibility region for the two PID system. Adapted from Ref. [20]

With both PID loops activated, the noise levels significantly decrease. For the PID-1 subsystem, the integrated noise reaches the 0.0055 noise floor. In the PID-0 master loop, noises are added in the range above 10 kHz, resulting in an overall integrated RMS noise of 0.0089. By comparing the corresponding noise power spectra in the sub-panels below, it is evident that the improvements are achieved mainly by suppressing the diverging spectral power at lower frequencies. Respectively, the feedback action defines a corner frequency fc of 0.5 Hz and 3 kHz for effective noise suppression in the two loops. While setting the goal of reducing the integrated noise markedly reduces the noise below fc, a slight increase in noise power above fc may be observed because of active intervention.

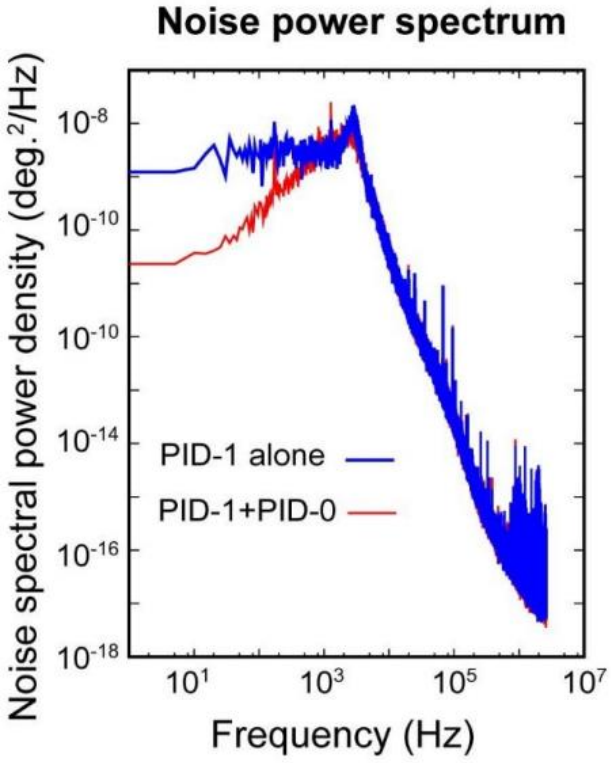

Figure 4.8. Interactions between the two PID control loops in the 10 Hz to 1 kHz range. Adapted from Ref. [20]

To study the interaction between the two control loops, we examine the time traces over different levels of PID controls. The blue curve in Fig. 4.8 shows the noise power spectrum from independently running the high-frequency feedback loop, where one can see the noise spectrum levels off at around 1 kHz. However, by turning on the PID-0 feedback control with the goal of reducing the overall integrated noise, the noise spectrum seen at frequencies below 1 kHz drops markedly. We view this synergistic effect also from the perspective of the PID-0 loop. The results are presented at different levels of feedback controls, first shown in the time traces in Fig. 4.9a over a span of 2000 seconds. As a reference, the top trace (in red) shows the free-running scenario. The trace below (in pink) gives the results from activating just the PID-1 feedback control. The noise level is reduced but not significantly. This surprising result is understood by closer examination of the noise fluctuations (inset panel), where a visible telegraph-like noise with switching behavior is shown. The switching frequency of this noise is below 0.1 Hz, thus undetected at the PID-1 level. Locally within each plateau, the noise level is significantly lower than the free-running case. From the histogram analysis, these noise features give a bi-modal distribution and carry a significant part of the integrated noise (see Fig. 4.9b). We also examine the case with activating just PID-0 (see Fig. 4.9a in green). In this case, the accumulated RMS noise reaches a level close to 0.01, better than the previous scenarios (see Fig. 4.9c). But the local noise is higher than the case with just turning on the PID-1 feedback control, albeit no signature of the telegraph noise can be traced here. We can thus conclude the presence of the telegraph noise to be a spill-over effect from active intervention in the higher frequencies – one that turning on PID-0 feedback control can help remediate. Indeed, by activating the two feedback loops simultaneously, both the local and integrated global noise are reduced.

We further consider the ramifications of the noise suppression protocols on actual experimental implementation where ultrafast diffraction or imaging carries the information frame-by-frame over the acquisition time of seconds. From this perspective, we examine the RF phase independently monitored at the UEM column while running the experiments shown in Fig. 4.10. By comparing the results between just activating PID-1 and joint feedback control (PID-0+PID-1), one can judge that the main improvement in integrated RMS phase noise comes from reducing the active period of the telegraph noise, and upon

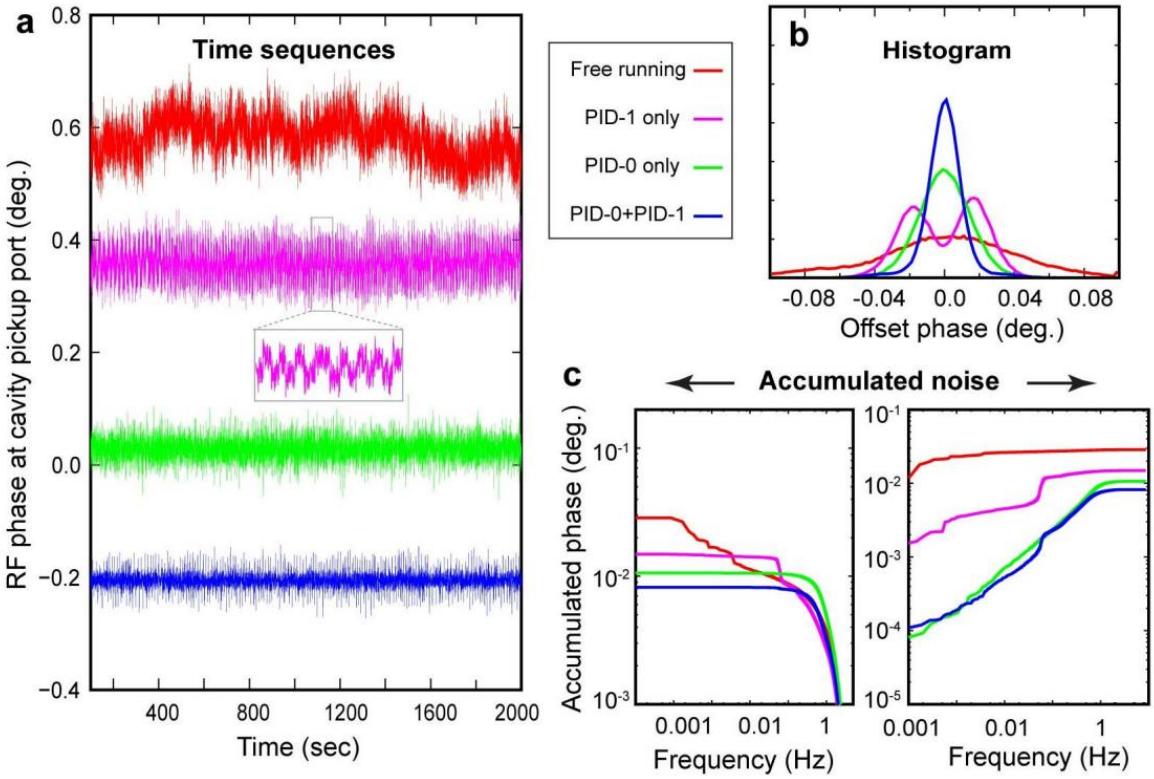

Figure 4.9. Noise characterization under different PID scenarios. a. The noise time sequences obtained by PID-0 phase detector with increasing levels of PID control; see the color-coded figure legend for the different PID settings. A pronounced source of noises is given at the level of PID-1 feedback control, where the uncompensated noises from PID-1 subsystem overflow into the master loop in telegraph noise-like steps at a relatively low frequency, ≈0.06 Hz; see the inset. b. The phase noise histograms obtained from corresponding time sequences in panel a. c. The accumulated RMS noises derived from integrating the noise power spectrum obtained from the time sequences. The left sub-panel shows the results with integration starting at the high frequency, whereas the right sub-panel gives the results with integration starting at the low frequency. Adapted from Ref. [20]

averaging, their contribution is minimized to a small pedestal region in the histogram representing the resolution function in the temporal response. Clearly, based on the Gaussian sigma value extracted from the histogram, the precision of the RF system has reached within 0.01° RMS. At this low level of jitters, it is essential to test the sampling error; currently, to be sensitive to noise from the higher frequency region for joint feedback control, the phase detector integration time is at 60 μs — which can clearly pick up the sharp rise of the telegraph noises (and hence correcting the effect in the feedback loop), but the short integration time may introduce a detector noise higher than the noise floor of the device. For this purpose, we deliberately raise the acquisition window to 350 μs (see Fig. 4.10 colored in green). At this acquisition time, the detector is still sensitive to kHz noises and can faithfully detect the residual noise spikes but long enough to reduce the sampling noises. The noise distribution, as given in the corresponding histogram, has a much-reduced Gaussian width of 0.0053°. Given our confidence that the noise spectrum above 1 kHz is effectively suppressed by the PID-1 feedback control (Fig. 4.7), we believe the measurement here does reflect the noise floor from the joint PID control loop.

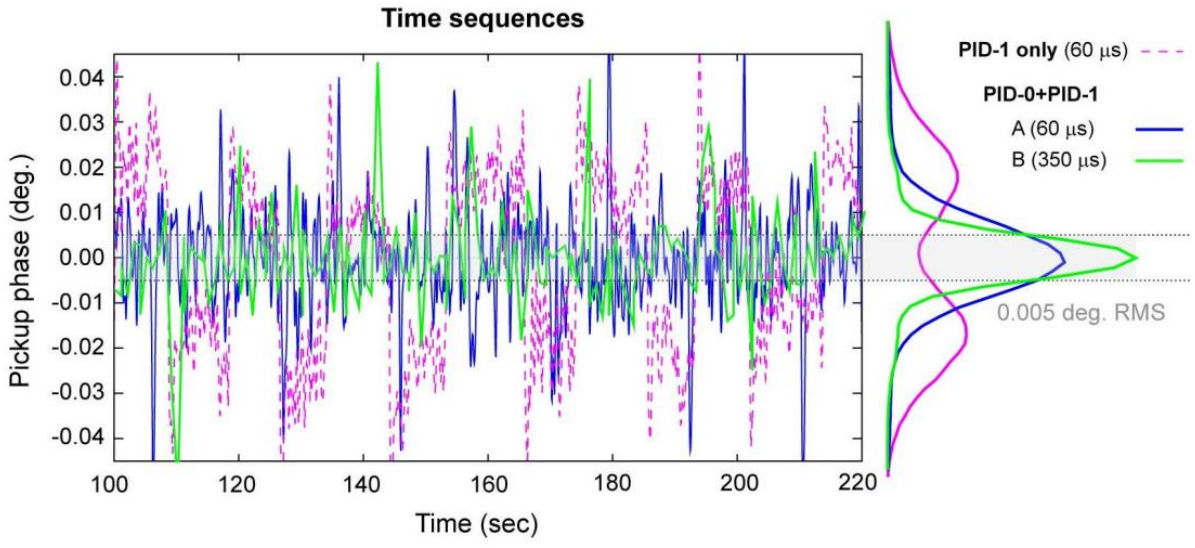

Figure 4.10. RF phase stabilities tracked by phase detector at the UEM station. Adapted from Ref. [20]

By recording the phase noise in real-time, one can adopt a strategy of rejecting the effects from spiky features by setting the acquisition primarily over low-noise regions. Keeping the acquisition time well below the timescale of the noise spikes allows for such discrimination. Meanwhile, any residual noise distributed over the acquisition time can be effectively compensated through data processing, using the recorded phase as the time stamp to shift the timing following Eq. 4.14. Judicious applications of these strategies will further reduce the noise floor for ultrafast measurements.

4.4 Experimental Validation of the Performance

To test the electron pulse width of the aforementioned cascade RF system, a beam test was conducted on mechanically exfoliated 30nm thick 1T-$TaSe_2$ flakes. The experiment was performed with 10^5 electrons per pulse, and the pump was set at 500 μJ/cm^2 to excite the longitudinal acoustic phonons at the K-edge[31]. The scattering data integration was carried out at a 5 kHz repetition rate over an 8-second acquisition period.

Fig. 4.11 gives the dynamical response for $TaSe_2$ after excitation. Basing off the obtained S/N and the ultrafast response extracted from the diffraction peaks, we evaluate the key performance figures of merit. First, regarding delivered beam transverse emittance, we determined the dose (D_e) and the beam coherence length (ξ_e) based of conducting the "atomic grating" approach[330]:

$$D_e = \frac{Ne}{2\ln(2)}\pi\sigma_x\sigma_y, \tag{4.21}$$

$$\xi_e = \lambda/2\pi\theta_s, \tag{4.22}$$

and the emittance is given by:

$$\varepsilon_x\varepsilon_y = \frac{N_e}{16\pi^3}\left(\frac{\beta\gamma\lambda}{lb(2)}\right)^2\frac{1}{D_e\xi_e}$$

where $\sigma_{x,y}$ is the transverse Gaussian beam width at the specimen, θ_s is the source angle defined by the stochastic velocity spread at the cathode, β and γ are relativistic factors. We obtained $De = 3e^-/um^2$ and

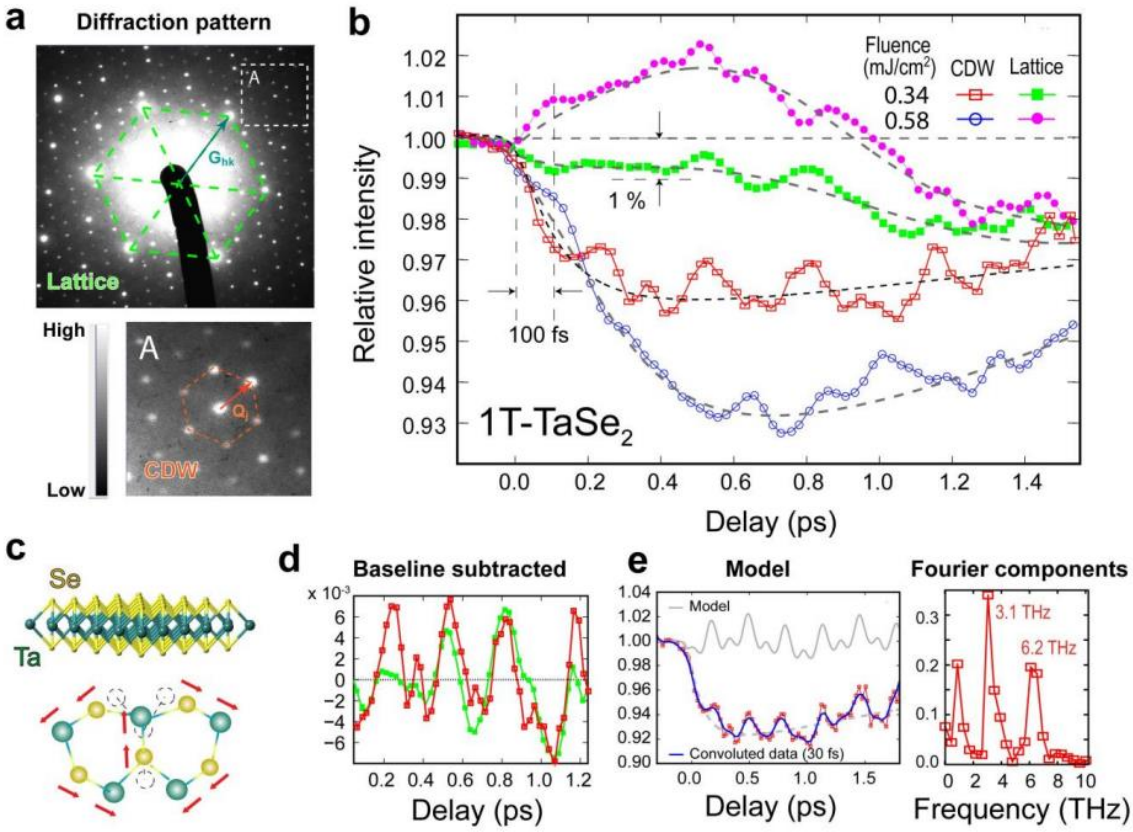

Figure 4.11. Coherent phonon dynamics probed by the ultrafast diffraction modality. a. The diffraction pattern from the exfoliated 1T-$TaSe_2$ sample, with dashed lines outlining the corresponding triangular lattice and charge density wave (CDW) supercell periodicities. **b.** Shows the intensity modulations registering coherent phonon dynamics, incoherent channels including thermal phonon signatures, and density-wave state evolutions. The coherent multiple-order nonlinear phonon excitation involving the zone-edge (K) acoustic phonon is visible as periodic high and low intensity modulations in the low fluence data set. **c.** Schematically reproduces the modal structure of the K-edge phonon from a previous study. **d.** Presents the baseline-subtracted transients from the main and superlattice structure factors, indicating phase-locking. **e.** Shows the Fourier analyses conducted to retrieve the coherent phonon frequencies. Adapted from Ref. [20]

$\xi e = 5nm$, which gives a transverse emittance of 5.7nm. This result agrees well with the value predicted by the theoretical simulation at the limit $N_e = 10^5$ per pulse. Accordingly, the simulation also gives the longitudinal emittance of 5 nm^3, which will allow the temporal resolution follow RF-optics compression well into sub-50fs. It is instrumental to point out the low-emittance pulse achieved at a high packing density here give a very high beam brightness at a single pulse level. The increased electron pulse brightness leads to better capability in discerning the structure dynamics over ultrafast timescale. To evaluate the corresponding boost in S/N to extract structure dynamics, we evaluate the signal floor presented in the diffraction contrast, we found the nominal noise level of 0.1% over the intensity of the charge density wave superstructure peak can be established to allow distinction of the multiple-order oscillations[32]. By applying the Overhauser's formula[33] for CDW structure factor $S_Q \sim |J_1(Qa)|^2$, the amplitude corresponding to this minimum distinguishing scale is estimated to be 10 femto-meter. For the temporal resolution, the RF compressed electron pulse has clearly reached the sub-100 fs resolution judging from the initial response time in the UED signatures. The phonon oscillation is shown in Fig. 4.11 d after baseline subtraction. On the other hand, Fig. 4.11e shows a minimum level convolution at ≈30 fs RMS to smear out the high harmonic signatures, which give a temporal resolution of ≈50 fs (FWHM).

4.5 Summary

In this chapter, we have explored the principles and advancements in RF compression techniques for ultrafast electron microscopy and diffraction. We began by introducing the basic mechanism of RF field compression and its role as a condenser lens in UEM systems. The impact of RF instabilities on temporal and spatial resolutions was investigated through simulations, highlighting the importance of precision control over the RF system.

To address the challenges posed by RF noise and instabilities, we presented the development of a cascade RF control system. This two-level PID feedback control scheme synergistically reduces the noise

floor while ensuring long-term stability. The master feedback loop (PID-0) compensates for phase differences over the entire RF circuit, while the nested feedback loop (PID-1) employs a digital phase-locked loop to suppress local phase noise. Through noise spectrum analyses and time trace examinations, we demonstrated the effectiveness of this cascade design in reducing the integrated RMS noise to an unprecedented level of 0.0053°.

The performance of the upgraded RF control system was validated through experimental studies on mechanically exfoliated 1T-$TaSe_2$ flakes. By evaluating the transverse and longitudinal emittances, we confirmed the delivery of high-brightness electron beams with a temporal resolution of $\approx$50 fs (FWHM) and a spatial resolution of 10 femtometers. The increased electron pulse brightness enabled the distinction of multiple-order oscillations in the diffraction contrast, showcasing the enhanced capability to discern structural dynamics over ultrafast timescales. The achieved 50 fs temporal resolution and improved spatial resolution is expected to open up new possibilities for investigating dynamic processes in materials at previously unavailable time and length scales. The enhanced precision and stability of the RF system, combined with the increased beam brightness, pave the way for more in-depth studies of ultrafast phenomena in a wide range of scientific fields.

REFERENCES

REFERENCES

[1] P.M. Lapostolle, T.P. Wangler, and A.M. Lombardi, *A Model of Non-Linear Space-Charge Forces in a Charged Particle Beam* (CM-P00059509, 1993).

[2] Z. Tao, H. Zhang, P.M. Duxbury, M. Berz, and C.-Y. Ruan, "Space charge effects in ultrafast electron diffraction and imaging," J Appl Phys **111**(4), (2012).

[3] J. Williams, F. Zhou, T. Sun, Z. Tao, K. Chang, K. Makino, M. Berz, P.M. Duxbury, and C.-Y. Ruan, "Active control of bright electron beams with RF optics for femtosecond microscopy," Structural Dynamics **4**(4), (2017).

[4] X. Xiang, P.M. Duxbury, and B. Zerbe, "Longitudinal crossover and the dynamics of uniform electron ellipsoids focused by a linear chirp," Phys Rev E **103**(2), 023202 (2021).

[5] P. Zhu, Y. Zhu, Y. Hidaka, L. Wu, J. Cao, H. Berger, J. Geck, R. Kraus, S. Pjerov, and Y. Shen, "Femtosecond time-resolved MeV electron diffraction," New J Phys **17**(6), 063004 (2015).

[6] S.P. Weathersby, G. Brown, M. Centurion, T.F. Chase, R. Coffee, J. Corbett, J.P. Eichner, J.C. Frisch, A.R. Fry, and M. Gühr, "Mega-electron-volt ultrafast electron diffraction at SLAC National Accelerator Laboratory," Review of Scientific Instruments **86**(7), (2015).

[7] J. Wu, M. Tang, L. Zhao, P. Zhu, T. Jiang, X. Zou, L. Hong, S.-N. Luo, D. Xiang, and J. Zhang, "Ultrafast atomic view of laser-induced melting and breathing motion of metallic liquid clusters with MeV ultrafast electron diffraction," Proceedings of the National Academy of Sciences **119**(4), e2111949119 (2022).

[8] Y. Murooka, N. Naruse, S. Sakakihara, M. Ishimaru, J. Yang, and K. Tanimura, "Transmission-electron diffraction by MeV electron pulses," Appl Phys Lett **98**(25), (2011).

[9] S. Manz, A. Casandruc, D. Zhang, Y. Zhong, R.A. Loch, A. Marx, T. Hasegawa, L.C. Liu, S. Bayesteh, and H. Delsim-Hashemi, "Mapping atomic motions with ultrabright electrons: towards fundamental limits in space-time resolution," Faraday Discuss **177**, 467–491 (2015).

[10] C.-Y. Ruan, F. Vigliotti, V.A. Lobastov, S. Chen, and A.H. Zewail, "Ultrafast electron crystallography: Transient structures of molecules, surfaces, and phase transitions," Proceedings of the National Academy of Sciences **101**(5), 1123–1128 (2004).

[11] C.-Y. Ruan, Y. Murooka, R.K. Raman, and R.A. Murdick, "Dynamics of size-selected gold nanoparticles studied by ultrafast electron nanocrystallography," Nano Lett **7**(5), 1290–1296 (2007).

[12] L. Genberg, L. Richard, G. McLendon, and R.J.D. Miller, "Direct observation of global protein motion in hemoglobin and myoglobin on picosecond time scales," Science (1979) **251**(4997), 1051–1054 (1991).

[13] A.H. Zewail, "Four-dimensional electron microscopy," Science (1979) **328**(5975), 187–193 (2010).

[14] A. Feist, N. Bach, N.R. da Silva, T. Danz, M. Möller, K.E. Priebe, T. Domröse, J.G. Gatzmann, S. Rost, and J. Schauss, "Ultrafast transmission electron microscopy using a laser-driven field emitter: Femtosecond resolution with a high coherence electron beam," Ultramicroscopy **176**, 63–73 (2017).

[15] S. Sun, L. Wei, Z. Li, G. Cao, Y. Liu, W.J. Lu, Y.P. Sun, H. Tian, H. Yang, and J. Li, "Direct observation of an optically induced charge density wave transition in 1 T− TaSe 2," Phys Rev B **92**(22), 224303 (2015).

[16] J. Portman, H. Zhang, K. Makino, C.Y. Ruan, M. Berz, and P.M. Duxbury, "Untangling the contributions of image charge and laser profile for optimal photoemission of high-brightness electron beams," J Appl Phys **116**(17), (2014).

[17] J. Frank, "The envelope of electron microscopic transfer functions for partially coherent illumination," in *Single-Particle Cryo-Electron Microscopy: The Path Toward Atomic Resolution: Selected Papers of Joachim Frank with Commentaries*, (World Scientific, 2018), pp. 51–68.

[18] P. Buseck, J. Cowley, and L. Eyring, *High-Resolution Transmission Electron Microscopy: And Associated Techniques* (Oxford University Press, 1989).

[19] K. Amini, A. Rouzée, and M.J.J. Vrakking, *Structural Dynamics with X-Ray and Electron Scattering* (Royal Society of Chemistry, 2023).

[20] X. Sun, J. Williams, S. Sharma, S. Kunjir, D. Morris, S. Zhao, and C.-Y. Ruan, "Precision-controlled ultrafast electron microscope platforms. A case study: Multiple-order coherent phonon dynamics in 1T-$TaSe_2$ probed at 50 fs–10 fm scales," Structural Dynamics **11**(2), 024305 (2024).

[21] F. Zhou, J. Williams, S. Sun, C.D. Malliakas, M.G. Kanatzidis, A.F. Kemper, and C.-Y. Ruan, "Nonequilibrium dynamics of spontaneous symmetry breaking into a hidden state of charge-density wave," Nat Commun **12**(1), 566 (2021).

[22] S. Sun, X. Sun, J. Williams, and C.-Y. Ruan, "Development of RF-compressed high-throughput femtosecond electron microscope," Microscopy and Microanalysis **26**(S2), 430–433 (2020).

[23] S. Sun, X. Sun, D. Bartles, E. Wozniak, J. Williams, P. Zhang, and C.-Y. Ruan, "Direct imaging of plasma waves using ultrafast electron microscopy," Structural Dynamics **7**(6), (2020).

[24] H. Yang, B. Han, J. Shin, D. Hou, H. Chung, I.H. Baek, Y.U. Jeong, and J. Kim, "10-fs-level synchronization of photocathode laser with RF-oscillator for ultrafast electron and X-ray sources," Sci Rep **7**(1), 39966 (2017).

[25] R. Li, C. Tang, Y. Du, W. Huang, Q. Du, J. Shi, L. Yan, and X. Wang, "Experimental demonstration of high quality MeV ultrafast electron diffraction," Review of Scientific Instruments **80**(8), (2009).

[26] O. Zandi, K.J. Wilkin, Y. Xiong, and M. Centurion, "High current table-top setup for femtosecond gas electron diffraction," Structural Dynamics **4**(4), (2017).

[27] M. Gao, Y. Jiang, G.H. Kassier, and R.J. Dwayne Miller, "Single shot time stamping of ultrabright radio frequency compressed electron pulses," Appl Phys Lett **103**(3), (2013).

[28] T. Van Oudheusden, P. Pasmans, S.B. Van Der Geer, M.J. De Loos, M.J. Van Der Wiel, and O.J. Luiten, "Compression of subrelativistic space-charge-dominated electron bunches for single-shot femtosecond electron diffraction," Phys Rev Lett **105**(26), 264801 (2010).

[29] R.P. Chatelain, V.R. Morrison, C. Godbout, and B.J. Siwick, "Ultrafast electron diffraction with radio-frequency compressed electron pulses," Appl Phys Lett **101**(8), (2012).

[30] C.-Y. Ruan, "The Many Facets of Ultrafast Electron Diffraction and Microscopy: Development and Applications," (2023).

[31] S. Bae, K. Matsumoto, H. Raebiger, K. Shudo, Y.-H. Kim, Ø.S. Handegård, T. Nagao, M. Kitajima, Y. Sakai, and X. Zhang, "K-point longitudinal acoustic phonons are responsible for ultrafast intervalley scattering in monolayer MoSe2," Nat Commun **13**(1), 4279 (2022).

[32] G.F. Giuliani, and A.W. Overhauser, "Structure factor of a charge-density wave," Phys Rev B **23**(8), 3737 (1981).

[33] G.F. Giuliani, and A.W. Overhauser, "Structure factor of a charge-density wave," Phys Rev B **23**(8), 3737 (1981).

Chapter 5

Physics of Vanadium Dioxide Phase Transition

5.1 Introduction

Vanadium dioxide (VO_2) has emerged as a prototypical functional material[1–4] exhibiting a remarkable photoinduced phase transition linked to its structure phase transition (SPT) and insulator-metal (IMT). At elevated temperatures, VO_2 undergoes a first-order phase transformation from an insulating monoclinic to a metallic rutile phase, accompanied by changes in optical[5], electrical[6], and magnetic properties[7]. The ability to induce this phase transition optically adds versatility to VO_2. The photoinduced transition[8–20] allows selective manipulation of VO_2's properties, opening avenues for novel optoelectronic devices and advanced functionalities. This phenomenon has sparked research efforts to unravel underlying mechanisms and explore applications. In this chapter, the photoinduced phase transition (PIPT) in VO_2 is studied via ultrafast electron diffraction (UED) and ultrafast differential optical transmittance (OP-TR) measurements, with a goal to provide information on the underlying mechanisms underpinning this cooperative phenomenon.

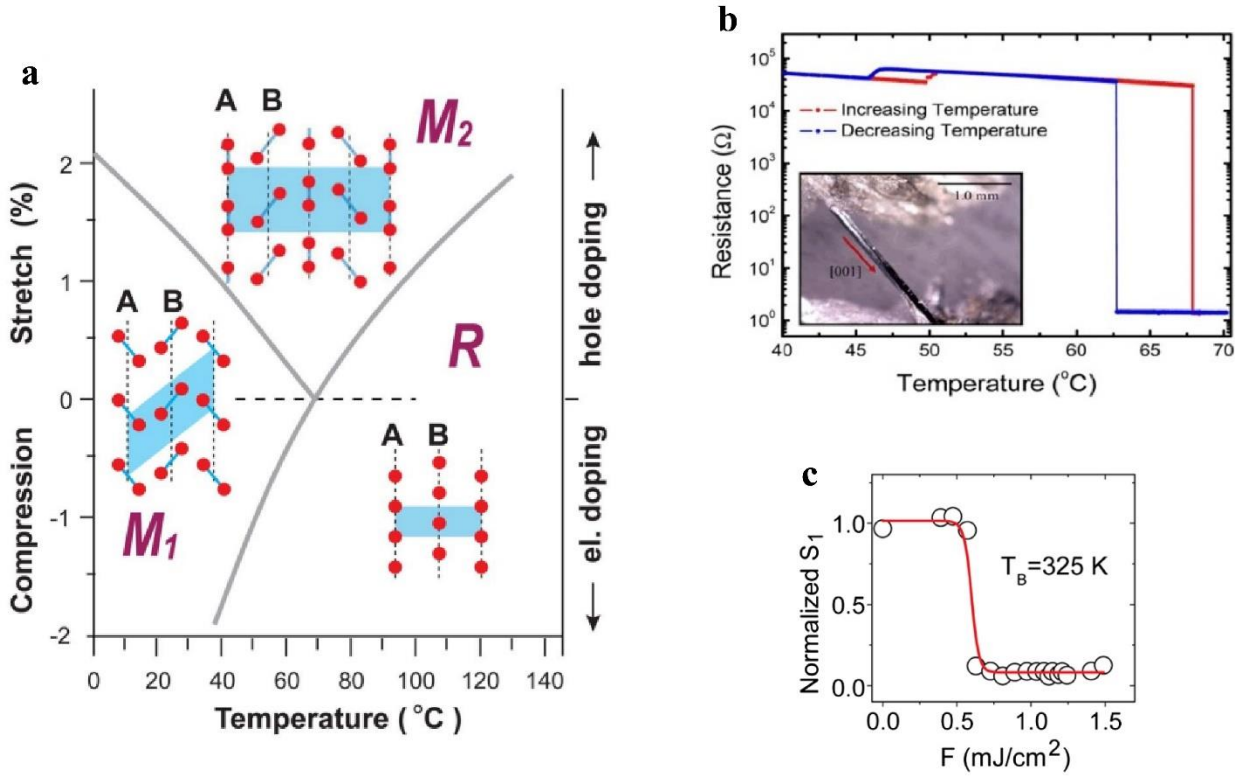

Figure 5.1. VO_2 phase transitions. a. The schematic phase diagram of VO_2. The layout of the structures highlights the vanadium atom distortions in the A and B sublattice chains (oxygen atoms are omitted) at different structural phases near room temperature: Monoclinic insulating M1 and M2 phases, and the metallic rutile (R) phase. **b**. At 68C, a sharp change in resistance is observed, together with the hysteresis indicating a first order phase transition in the free-standing nanobeam sample. **c**. A first-order photo-induced phase transition occurring at a sharp fluence threshold determined via the electron diffraction monitoring the dimerized superlattice reflection (S1) for the single crystal free standing VO_2 nanobeam upon illuminating with a near-infrared pulses. Panel **a** adapted from Ref[21]. Panel **b** adapted from Ref[22]. Panel **c** adapted from Ref[23].

5.1.1 Equilibrium Properties of VO_2.

VO_2 belongs to a class of highly versatile phase-change transition metal oxide (TMO) that exhibits complex phase diagram under a variety of controls, including varying temperature, pressure, chemical substitution, as well externally applied electric or magnetic fields[24–26]. A particularly noteworthy characteristic of VO_2 lies in its transition threshold (T_{th} ~68°C) being very close to the room temperature, hence prone to a variety of practical applications. A recent striking display of the precision in the property tuning is demonstrated in transition over the *free-standing* single-crystal VO_2 nanobeams both upon varying the specimen temperature[22] and illuminating with laser pulses[23]; see Fig. 5.1b and Fig. 5.1c. By avoiding the phase coexistence under strain[27], IMT within 0.1-Kelvin precision for an upshoot of conductivity by 5 orders of magnitude has been demonstrated[28,29]. In the high-temperature state, the conducting VO_2 has the rutile (R) crystalline lattice belonging to the space group P42/mnm, with the unit cell lattice constants $a_R = b_R = 4.554$ Å, and $c_R = 2.851$ Å[30]; see Fig. 5.2a. On the other hand, in the low-temperature state below 68°C, VO_2 switches into the insulating monoclinic structure (M1) characterized by the space group P21/c. Here, along with the crystalline motif changes, within the unit cell the vanadium atoms undergo two types of antiferroic structural distortion along $\mathbf{c}_R 31$ with longitudinal V shift (~ 0.14 Å) forming V-V pairs and transverse V shift (~ 0.18 Å) twisting the V atom along the V-O bond (away from $\mathbf{c}_R 32$), which is either along the $(110)_R$ or $(1\text{-}10)_R$ directions in the two sub-lattice chains; see Fig. 5.2b. These local distortion results in a doubling of the unit cell, with $a_{M1} = 5.752$ Å (the direction of c_R), $b_{M1} = 4.538$ Å, $c_{M1} = 5.383$ Å, and a unit cell canting angle of 122.65°[33]; see Fig. 5.2a.

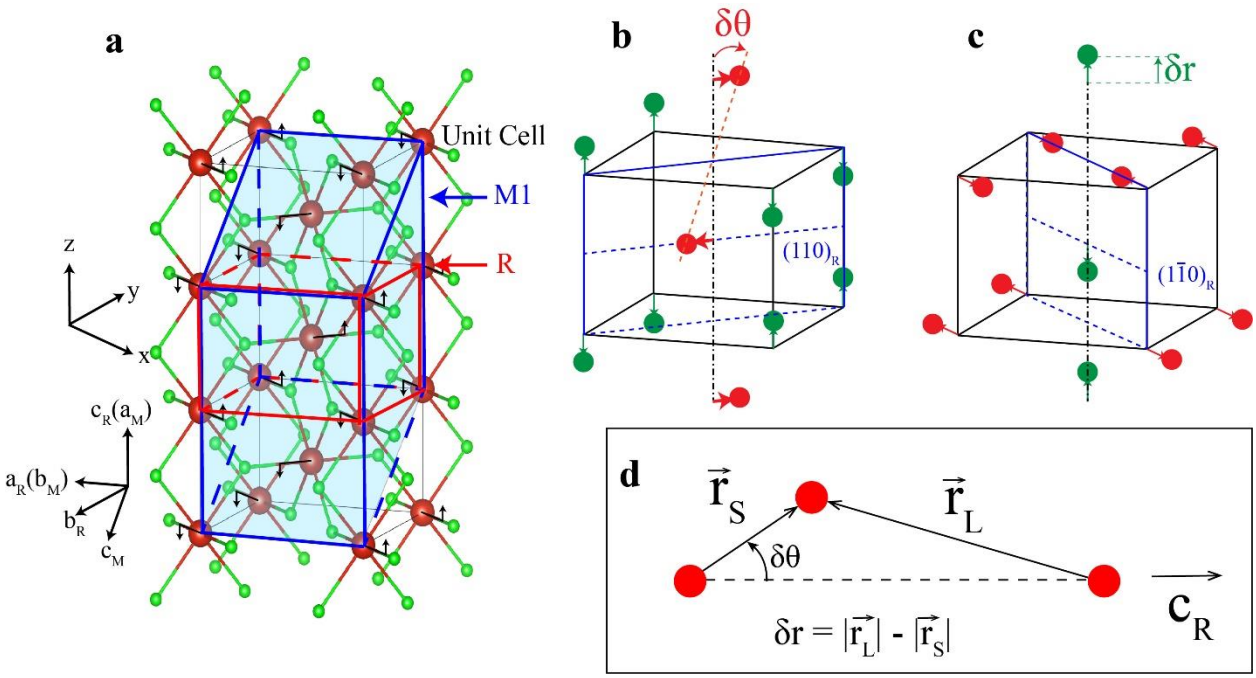

Figure 5.2. The crystalline structure motifs of VO_2. **a**. The VO_2 structure in the R state. The arrows indicate the direction of movement of V^{4+} ions in M1 state compared to those in R state. The blue shaded area indicates the conventional M1 unite cell, which is double the size of the unit cell in R state. Panels **b** and **c** show the two simultaneously running periodic distortion waves, the superposition of the two gives the M1 structure. **d.** A schematic plot depicts three V^{4+} ions' positions along the $\mathbf{c}_R$ direction, where the two order parameters $\delta r = |r_l| - |r_s|$ and $\delta\theta$ are defined based on the pairing distance and the twisting angle between the short and long V-V bonds.

5.2. Single-particle Band Diagram and Discontents

The band structure of VO_2 has been theoretically calculated by considering the crystal symmetry[34–36]. In the R phase, the coupling between vanadium atoms and their surrounding oxygen octahedra causes the splitting of V 3d orbitals into two bands. The lower band comprises the triply degenerate t_{2g} orbitals (d_{xy}, d_{yz}, and d_{xz}), while the higher band consists of the e_g orbitals (d_{z^2} and $d_{x^2-y^2}$). The e_g orbital, pointing towards the oxygen ions, experiences a strong splitting into bonding and antibonding states due to the covalent interaction. Furthermore, owing to the edge-sharing arrangement of octahedra along the c_R axis, the t_{2g} orbitals undergo an additional splitting, resulting in two π bonding and antibonding states (d_{xz} and d_{yz}) with a larger energy separation, and a non-bonding a_{1g} (also called $d_{//}$) orbital for d_{xy}. In the rutile structure, both the π^* and $d_{//}$ bands lie at the Fermi level, leading to the generic metallic behavior in VO_2. However, within the band picture the quasi-1D V-V sublattice chains are subject to Fermi-surface instabilities derived from degenerate structures leading to spontaneous symmetry breaking. The low-temperature band structure, elucidating the insulating nature, was initially proposed by Goodenough[34] based on such lattice symmetry considerations, where the M1 phase of VO_2 was described as a Peierls insulator. Upon cooling to the M1 phase, the dimerization of vanadium atoms increases the overlap of the $d_{//}$ orbitals, splitting them into bonding and antibonding states. Moreover, the twisting of vanadium atoms towards the oxygen ions enhances the overlap between the t_{2g} orbitals and the O-2p orbital, thereby raising the energy of the π^* band. The splitting of the $d_{//}$ orbitals and the upward shift of the π^* band collectively open a gap at the Fermi level, resulting in the insulating behavior observed in the M1 phase. This proposed band energy diagram is depicted in Fig. 5.3.

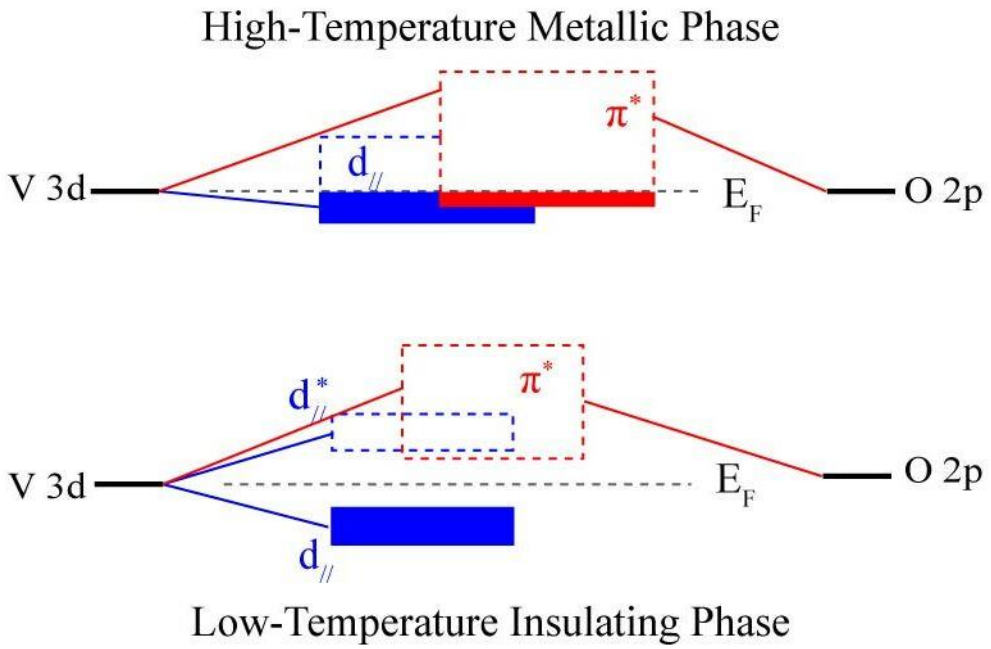

Figure 5.3. Molecular orbital energy diagram of VO_2. The diagrams depict the orbital state level spitting going from the high temperature metallic phase (bottom) to the low temperature insulating phase of VO_2 (top).

There have been substantive debates over whether the Peierls distortion alone might be responsible for the IMT by gauging the later-on established relatively large gap size (~ 0.7 eV) which is substantively larger than the expected value based on the electron-phonon coupling in the single-electron picture[37]. Many-body effects, including considering on-site Coulomb repulsion energy, is shown as essential, and by coupling the two effects the large gap size in $d_{//}$ bands might be accounted for [38–40]. Alternatively, the strong electron-phonon coupling as derived by the *d*-band physics as a general argument for the strong cooperativity between SPT and IMT shown at the thermally induced phase transition as initially suggested by Paul and Hearn[41,42]. The strong *d*-electron-phonon interactions alter the total d-electron energy in both phases. However, it will have

a greater effect in the metallic phase because of the greater state degeneracy at the Fermi level, and as a result, the more important consequence of softening the mode[41]. As such, it may be said that the greater entropy of the metallic phase, which then lowers the free energy at IMT, resulting in a stabilization of rutile, as the key elements that drives the transition[42]. The recent inelastic X-ray scattering study indeed show that nearly the entire phonon band soften at monoclinic to rutile phase transition[43]. This excess in phonon entropy effect may be the clearest evidence to support the cooperativity and the sharp 1st order transition nature of VO_2 near room temperature. However, this macroscopic thermodynamic transition which necessitates long-range ordering, also clouds the microscopic picture of the *d*-band physics (Mott Hubble) and the relevant exchange interactions, which play a role in the large gap size.

5.3 Many-body Effects in Insulator-metal Transition (IMT)

Mott and Zylbersztejn proposed an alternative explanation based on electron-electron correlations in the $d_{//}$ states[31]. In the Mott picture, the strong interaction between electrons in the *d* orbitals is considered, where electrons need to overcome a strong on-site Coulomb potential to hop between sites[44]. If the kinetic energy of the electrons is less than this potential, they will be localized. In this case, the on-site Coulomb repulsion acts as an energy penalty for double occupancy of a site by two electrons with opposite spins, splitting the initially single $d_{//}$ band into two sub-bands, known as the lower and upper Hubbard bands. When the reduction in Coulomb repulsion by localizing electrons to avoid double occupancy on vanadium sites outweighs the decrease in kinetic energy from delocalization, the system exhibits insulating behavior due to the gap that opens between the occupied lower Hubbard band (LHB) and the unoccupied upper Hubbard band

(UHB)[31]. According to the Mott's model, in the rutile phase, the uncorrelated π^* band effectively screen the electrons in the $d_{//}$ band, leading to metallic properties. However, the upshift of the π^* band and splitting of the $d_{//}$ band that occur during the SPT to the M1 phase remove this screening in the now filled lower $d_{//}$ band, opening the Mott-Hubbard gap and inducing insulating behavior. However, since there is one electron per site in Mott insulator, it is energetically favorable for the neighboring electrons to have opposite spins, thus forming an anti-ferromagnetic ordering, which is not observed in M1 structure VO_2.

Direct evidence indicating the M1-insulating ground states hosting strongly interacting electrons are from tuning Mott-Hubbard gap through doping and applying pressure to carry out bandwidth control[45]. Doping VO_2 with higher valence cations, such as tungsten (W^{6+})[46] or molybdenum (Mo^{6+})[47], has been found to suppress the metal-insulator transition temperature and stabilize the metallic rutile phase down to lower temperatures. This is attributed to the increased electronic bandwidth from hole doping, which weakens the electron-electron correlations responsible for the Mott insulating state. Conversely, doping with lower valence cations like chromium (Cr^{3+})[48] or aluminum (Al^{3+})[49] tends to induce insulating behavior and increase the transition temperature by reducing the electronic bandwidth and enhancing correlations. Similarly, application of external pressure has also been demonstrated to significantly impact the phase transition in VO_2. High pressures favor the higher-density metallic rutile phase, progressively suppressing the metal-insulator transition temperature[50]. This pressure-induced metallization is proposed to arise from the increased bandwidth and screening of the Coulomb interactions, destabilizing the Mott insulating state.

5.4 Photo-induced Phase Transition

The photoinduced phase transition (PIPT) in VO_2 has been a subject of investigation since 1994, when Becker et al. employed a 780 nm laser to measure the optical transmission and reflection change following the phase transition[51]. Despite extensive research efforts, the PIPT process in VO_2 remains not fully understood, sparking numerous debates within the scientific community. One central open question regarding PIPT is whether the light induced VO_2 phases maintain the same electronic and structure identities as those in a thermodynamic phase transition. A hallmark of the equilibrium transition as outlined in Fig. 5.1a is the simultaneous electronic and structural changes under chemical doping or by applying stress and varying temperature. While most arguments put forth about such *cooperative* IMT and SPT tie the insulating state with the M1 crystalline motif, the Mott insulating ground state is found under a closely related monoclinic (M2) crystalline motif as well. Similarly, one could argue that within the rutile motif, excessively doping the system or imparting disorder, insulting property could emerge. In the various arguments for the interaction-mediated IMT[45], it is the local V-V and V-O distances and structure distortion over the vanadium sub-lattices that provide the incentive for the spontaneous gap opening, rather than the crystalline lattices. These local perspectives prompt the possibility of observing a metallic state under a different crystalline motif other than the rutile structure. In other words, the cooperativity between the IMT and SPT might be broken in the nonequilibrium regimes.

A recent attempt to carry out comparison between IMT and SPT using the same sample was carried out by Morrison et al. by UED measurements combined with separate optical transmittance measurements[16]. Based on the different transition thresholds determined for the two separate measurements, the authors concluded the existence of a metallic monoclinic (*mM*) phase

during the PIPT process in polycrystalline VO_2 samples. Specially, in their experiments, the metallic phase as identified by the optical probe emerged when the fluence level just surpasses the 25% of the threshold fluence set by the UED measurements (defined here as a 50% change in the detected structure order parameter). The utilization of percentage to describe the fluence is to ensure consistency across different measurements. The *mM* phase is characterized by a fully altered transmittance change accompanied by a low-level diffraction change, which lasts hundreds of picoseconds. In a separate work with THz probe to monitor the electronic phase transition[17], a discrepancy in the speed among different diffraction peaks and various regions of the THz spectrum was observed, which the authors attributed to the rapid melting of the M1 structure and slower charge re-organization processes. This work has garnered attention in the scientific community, as the X-ray spectroscopy study indicates that the energy region at 530.5 eV, sensitive to structural changes, and the energy region at 529 eV, sensitive to conductivity changes, actually share the same fluence threshold[52] at 400 ps, casting into doubt whether there is actually a decoupling between the IMT an SPT observed in the various PIPT experiments.

There are a couple of reasons why it is very difficult to judicate the "cooperativity question" from comparing experiments obtained from different techniques or under different specimen settings. VO_2, characterized by its first-order phase transition nature, exhibits a distinct transition threshold once the PIPT process is fully developed. However, due to the inhomogeneous distribution of lattice strain, a finite broadening in the transition threshold was often observed in the studies of single-crystal bulk specimens and polycrystalline thin film alike[53], except for free-standing nanobeams experiments[8]. The fluence threshold, defined here as a 50% change in the detected order parameter, has been reported to vary significantly across different measurements, leading to confusion. For instance, Morrison et al.[16] investigated the PIPT process of 70 nm VO_2

using transmission UED mode and observed the transition threshold based on *superlattice* peaks associated with the M1 state at fluence 25mJ/cm^2, while Tao et al.[23] studied a 31 nm sample and reported a 50% suppression of the same peak at a fluence of 7mJ/cm^2. Without accounting for the thickness difference, this disparity in fluence amounts to 250%. However, when the thickness is taken into consideration, the difference based on considering absorbed energy density is reduced to 58%, which can be attributed to the geometry effect on the absorption coefficient, interference effect, inhomogeneous distribution of energy density, and thermal dissipation coefficient.

It is important to note that the effective thickness is also significantly impacted by the probing angle. In the case of perpendicular probing (i.e., transmission mode UED), the sample thickness can be treated as the effective thickness, provided that the penetration depth for both pump and probe is sufficiently large. Conversely, for reflective measurements, even though the probe typically only interrogates the first few nm of the sample, the small incident angle results in a much larger effective traveling distance for both pump and probe, necessitating careful consideration of the effective thickness in this scenario.

Moreover, it has been demonstrated that the critical fluence of VO_2 is strongly influenced by the sample's temperature; the required fluence decreases with increasing sample temperature[9,18,20,52]. This bring forth the debate about whether IMT thresholds reported by the ultrafast optical techniques, which typically employed higher repetition rates, to be generally smaller than thresholds reported from ultrafast structure probes carried out under a lower repetition rate to be caused by this effect[52].

5.5 Effective Medium Theory (EMT) for PIPT at Equilibrium Limit

Our research effort is designed to clarify some of the compounding issues in VO_2 PIPT research by carrying out the simultaneous characterizations of IMT and SPT using the ultrafast electron microscope platform, incorporated with an *in-situ* capability of ultrafast optical probe as described in Chapter 3 and Chapter 4. However, before going into the details of such measurements it is instrumental to discuss our methodology designed to isolate the effects from the specimen temperature, pump repetition rates and the impact from the varying strains posed by different specimen settings. For isolating the active fraction of the specimen undergoing PIPT, we developed a dual control parameter effective medium theory (EMT) to treat the data obtained under the general experimental conditions where the specimen temperature and the applied fluence (F_{app}) were varied as control parameters to investigate the various regimes of PIPT.

5.5.1 Formalism of EMT.

I will first introduce this effective medium theory by considering a single-crystal system not under active stress, such as nanometer scale single-crystal beams or small crystals, in which the transition thresholds under temperature (T_{th}) and optical pumping (F_{th}) are well defined. As the EMT is not expected to apply over the short time, we consider the case at the long time where the system fully thermalizes as in the equilibrium scenario. As the photoexcitation eventually turns into joule heating of the specimen, we can unite the effects from varying temperature and laser fluence to describe the M1 to R transition, governed by the transition curve:

$$\Im(T_i, F_{app}) = \Theta(T_i - T_{th}^0, F_{app} - F_{th}^0), \tag{5.1}$$

where Θ is the 2D step function, and T_{th}^0 and F_{th}^0 are the respective transition thresholds obtained in thermal induced and photo-induced phase transition experiments carried out with just a singular control parameter.

Under the circumstance where the late stage PIPT turns into a thermally induced phase transition, one can turn Eqn. 5.1 into a simple equation with the identify where the energy deposited by the laser pulses E_{abs} becomes the source of heating that leads to a temperature increase by the amount E_{abs}/C_v, where C_v is the heat capacity. Equation 5.1 is then simplified especially when expressed in the normalized coordinates for the temperature ($\hat{T}$) and the applied fluence ($\hat{F}$):

$$\hat{T} + \hat{F} = 1, \tag{5.2}$$

where $\hat{T} \equiv \frac{T - T_{th}^0}{T_{th}^0 - T_0}$ and $\hat{F} \equiv \frac{F - F_{th}^0}{F_{th}^0 - F_0}$.

The boundary separating the M1 and R phase in the phase diagram (Fig. 5.4a) where both control parameters are active is now given by Eqn. 5.1. In the joule heating scenario, the absorbed photon energy density is evaluated based on $E_{abs} = F \cdot \gamma$, where the ratio γ is given by considering the material's optical absorbance *R* and the laser penetration depth. When the sample thickness (*d*) is smaller than the absorption depth, one simply arrives at $\gamma = R/d$. A slanted line – plotted with the thick black line – is derived for VO_2 in this regime (where heat capacity C_v is nearly a constant[54] near T_0). The joule heating scenario gives the threshold line a slope of γ/C_v. Away from this regime, one must consider the latent heat H_L, which sets the lower bound of the fluence threshold F_0, below which the temperature threshold remains at T_{th}^0 irrespective of the applied fluence.

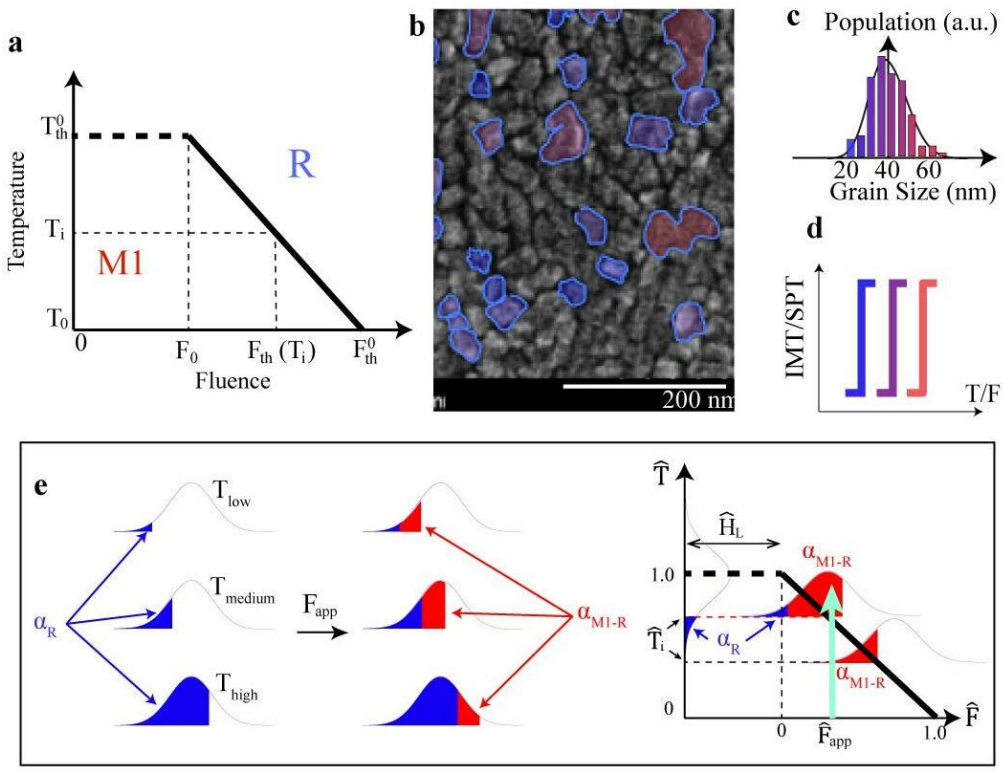

Figure 5.4. The effective medium theory for 1st-order phase transition mediated by the temperature and the optical fluence effects. **a**. The two-dimensional (2D) phase diagram separating the M1 and the R phases. The slanted threshold line (in thick black color) has a slope of γ/C_v given by equating the optical energy absorbed to the temperature rise. The horizontal dash line originated from F_0 to 0 is given by the crystalline latent heat. Within this regime, the deposited energy does not lead to a suppression of temperature threshold T_{th}. **b**. SEM image of VO_2 polycrystalline thin film where the small grains in blue have a lower transition temperature than the large grains in red due to strain effect caused by compressive surface tension. **c**. The size distribution of nanocrystalline grains retrieved from SEM image. The color code reflects the size effect in the transition temperatures over different grain sizes. The local transition curves are given in panel **d**. **e**. The weighting of three volume fractions changes at different initial temperatures but excited with the same fluence.

This joule heating scenario for the late stage PIPT can be tested experimentally. But before carrying out such measurements, one must consider that in practical setting the transition curves will be broadened by the lattice strain that inviably exist as discussed earlier. We define a clean case by experimenting on the small crystalline grains. The small sample size allows the strain to fully relax upon heating and withholding single-phase before and after transition with a sharp transition curve, as discussed earlier. Nonetheless, the experiments would typically be carried out employing a large ensemble of such small-grained samples, forming a polycrystalline VO_2 film, which one can prepare via pulsed laser deposition[55]. Figure Fig. 5.4b give the scanning electron microscope (SEM) image of the samples we typically used. Based on the SEM image, the crystalline grain volume fraction distribution $P(s_g)$ is extracted and fitted with a Gaussian distribution; see panel c. In this case, we determine the mean gran size $\overline{s_g}$ to be 45 nm with a standard deviation σ_{sg} of 11 nm.

The transition threshold within each sample grain is determined by crystalline stress set by the surface tension. Such an effect is found in thermally induced phase transition. The sign of the shift is given depending on the stress is compressive (down-shift) or tensile (upshift) compared to the bulk system; see Fig. 5.1a. We can assume such dispersion exists also for late-stage PIPT under the joule heating scenario. In such case, we can construct the unified transition curve based on the common probability function $P(s_g)$ established here:

$$\Im(x) = \int_0^\infty P(s_g)\Theta\left(x - x_{th}(s_g)\right) ds_g, \tag{5.3}$$

where x expresses either the temperature or the applied fluence. With $P(s_g)$ being depicted as a Gaussian, $\Im(x)$ is broadened into an error function. The distribution function can be defined as a universal probability function in the normalized coordinates:

$$P\left(\hat{F}-1\right)=P\left(\hat{T}-1\right)=P\left(\frac{s_g}{\overline{s_g}}-1\right). \tag{5.4}$$

This expression simplifies the calculation for EMT considering the dispersion of the samples. In particular, one asks in a generalized case when the temperature T_i is tuned away from the reference point (T_0) and a laser fluence F_{app} is applied, what would be the volume faction in the entire ensemble that could undergo phase transition, when varying strain field exists in each individual grain. Septically, by applying Eqn. 5.4 one can evaluate three types of distributions: (i) the volume fraction pre-excited into the R phase $\alpha_R^0(T_i)$, (ii) the volume fraction undergoing M1 to R transition $\alpha_{M1-R}^0\left(T_i,F_{app}\right)$, and (iii) the volume fraction remaining in the M1 state $\alpha_{M1}^0=1-\alpha_R^0-\alpha_{M1-R}^0$.

This evaluation is easily carried in the normalized coordinates:

$$\alpha_R^0(T_i)=\int_0^{\hat{T}_i}P\left(\hat{T}-1\right)d\,\hat{T}$$

$$\alpha_{M1-R}^0\left(T_i,F_{app}\right)=\int_{\hat{T}_i}^{\hat{T}_i+\hat{F}_{app}}P\left(\hat{T}-1\right)d\,\hat{T} \tag{5.5}$$

5.5.2 Cooperativity between Thermally Induced and Late-stage Photo-Induced Phase Transition.

We are now ready to carry out key experiments attesting the assumption behind the EMT, which is crucial for us to address some open questions raised by the earlier PIPT studies. First, we investigate the interplays between the IMT and SPT to validate whether the cooperativity between the two would be verified in the late stage of evolution in PIPT. The experiments are conducted

by measuring the structural and optical differential transmittance changes as we tune the laser fluence across the transition threshold. Here, the SPT is gauged via the normalized change in the intensity of the symmetry-breaking diffraction peak $(30\bar{2})_{M1}$, or $\Delta\hat{I}(30\bar{2})_{M1}$, reflecting the population in the M1 phase. The transition onto the metallic phase is evaluated via the increase of the optical differential transmittance, or $\Delta\hat{I}_{OP-TR}$. To ensure thermal equilibrium in these results, the data points are collected at a late stage (t = 500 ps). The respectively determined transition curves $\Im_{SPT}(F)$ and $\Im_{IMT}(F)$ are presented in Fig. 5.5a. The two curves agree exceptionally well, signifying the two transition channels are tightly coupled at the late stage of PIPT.

5.5.3 The Validity of the Joule-heating Description for Late-stage PIPT

The validity of using the joule-heating scenario for describing the late-stage PIPT process is tested by uniting the thermally induced and photo-induced phase transitions using the unified EMT given by Eqn. 5.2. We conducted experiments based on IMT using the optical probe. The respectively obtained transition curves $\Im_{IMT}(T)$ and $\Im_{IMT}(F)$ are plotted in Fig. 5.6b. Here, we align the two curves together by applying a scaling factor η in the horizontal axis of $\Im_{IMT}(F)$. The agreement between the two indicates transition curve broadening, as characterized by the respective Gaussian sigma σ_T and σ_F are introduced by the same effect, namely the impacts from inhomogeneous crystalline lattice strain apply to thermally and photo-induced phase transitions invariably. We determine in the case here σ_T= 6.8 K and σ_F= 1.8 mJ/cm^2, which gives the scaling factor $\eta = \frac{\sigma_T}{\sigma_F} =$ 3.78 to carry out the collapse. We point out that governed by joule heating the slope for the 2D threshold line is connected to the conversion efficiency (γ) of laser into heat through the relationship: $\eta = {}^{\gamma}/_{C_v}$. Hence, data collapse offers a different way for calibrating the optical

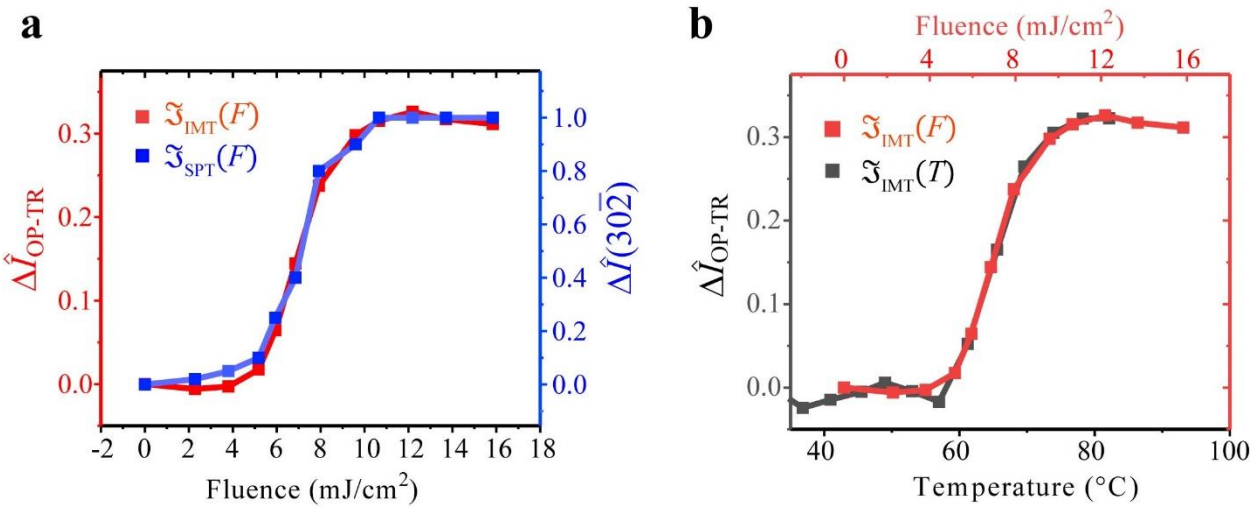

Figure 5.5. Transition curves for VO_2 IMT and SPT mediated by varying specimen temperature or applied laser fluence. a. The transition curve for IMT as characterized by optical differential transmittance in the PIPT experiments along with the transition curve for SPT obtained via tracking the intensity at the symmetry-breaking lattice reflection $(30\bar{2})_{M1}$ characteristic of M1 phase. These results are obtained at the late stage (t = 500 ps) to ensure thermal equilibrium. The coincidence of the results indicates the strong cooperativity between the two transitions. **b**. Correlation between the transition curves obtained independently via varying the control parameters: the temperature and the applied laser fluences. The two transition curves can collapse into one by aligning them with the respective transition thresholds and adjusting the fluence-dependent curve with a scale factor 3.78.

absorbance. Specifically, the scaling factor is given by as described in Fig. 5.5a as. Here, we can give $\gamma = 1.13 \times 10^7$ using the well determined $C_v = 3.35 \times 10^6$ given by Ref. [54]. Meanwhile, an independent estimate by the transfer matrix using the optical constants of VO_2 at the excitation wavelength 800 nm[56] gives γ to be 1.38×10^6. The two values are indeed close. Based on this, we might conclude, in addition to other evidences, the joule-heating scenario is a valid description for the late-stage evolution of PIPT.

5.5.4 Repetition Rate Dependence and the Evidence of Nonthermal Dynamics at Early Stage.

Backed by the success of EMT for capturing the late-stage evolution of PIPT, we can now address more controversial issues reported in early experiments regarding reconciling varying PIPT dynamics carried out using different pump-probe repetition rates (f_{rep}). Our controlled experiments were conducted at a fixed fluence F = 6.1 mJ/cm^2 while f_{rep} is tuned from the 200 Hz up to 1479 Hz. Importantly, the temperature response data $[\Im_{IMT}(T)]$ reported in Fig. 5.5 for thermal transition can be employed here as a calibration to track the initial temperature of the system at different f_{rep}. Indeed, we see, as shown in Fig. 5.6, when the repetition rate increases, a rise in negative-time optical transmittance is visible above 500 Hz. This, according to $\Im_{IMT}(T)$ reported earlier, shows the steady-state temperature of the specimen has been raised to cause an increase in the pre-excited R state volume fraction α_R^0 (in small grains, or the blue region in Fig. 5.4 b and c). This is a result of residual heat as over an increased rate there is not enough time for the sample to cool down to room temperature before the next pump's arrival[57].

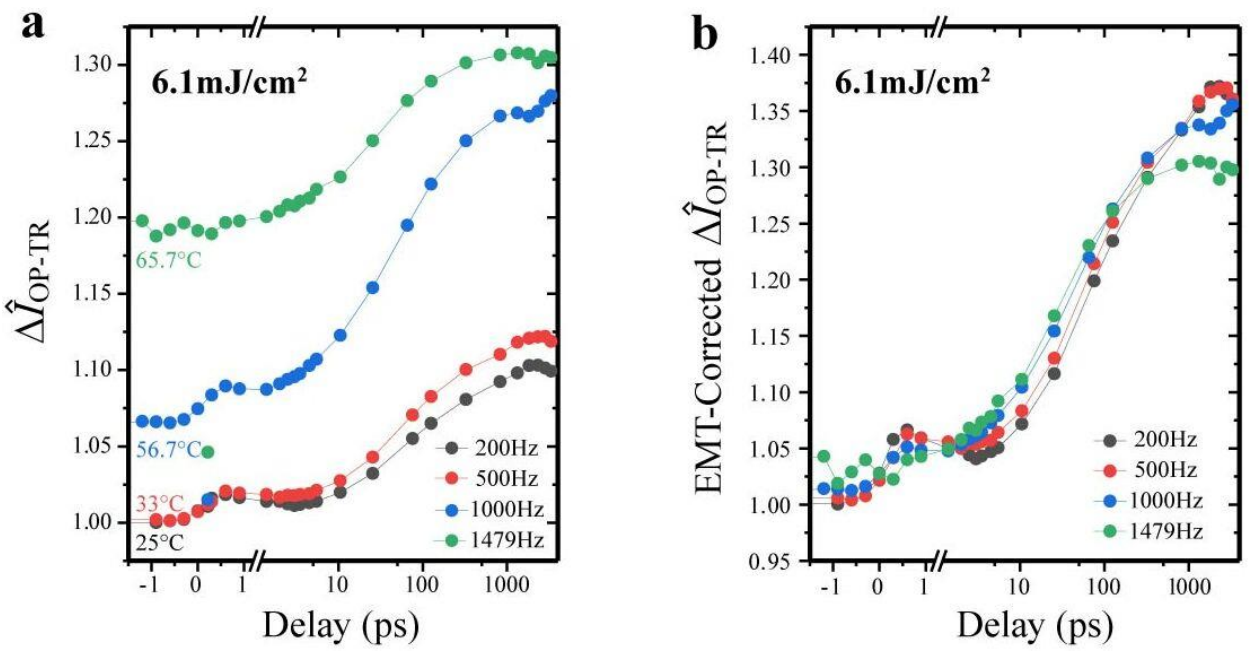

Figure 5.6. The repetition-rate dependent dynamics. a. shows the raw data of the transmittance change after VO_2 being excited by 6.1mJ/cm^2 laser at different repetition. **b**. shows the dynamics after normalized by the volume fraction of the sample went through phase transition.

The residual heating effect causes the transition dynamics to differ greatly as shown in Fig. 5.6a. The estimates of initial state temperature at different f_{rep} are given based on the temperature response data (Fig. 5.5). However, for data at 500 Hz, the shift in negative-time transmittance is un-detectable. To estimate its initial temperature, Newton's law of cooling is applied using the known temperature values at 200 Hz, 1 kHz, and 1.48 kHz, with the time window between pump pulses serving as the cooling time. In Fig. 5.6b, we show the dynamics after normalization by applying the volume fraction α_{M1-R}^{0} determined based on EMT. After the normalization process, in range between 10 to 500ps, the dynamics are the same even for different repetition rates. The success in restoring the nonequilibrium PIPT results owes largely to the success of evaluating the active regions to undergo a phase transition with EMT. We however note that at the highest f_{rep} some common features seen at lower f_{rep} cannot be reproduced, suggesting evidence of irreversible effects other than the residual heating may be present.

The results present here not only validate EMT for evaluating the active population based on the dynamics at the late-time near-equilibrium regime but also demonstrates that the IMT dynamics over the non-equilibrium timescale driven by the same laser fluence are ubiquitous and show no size dependence. This is in sharp contrast to a thermal transition. The loss in the correlation to the crystalline strain field at the early stage of evolution laid the foundation for studying nonequilibrium dynamics that are governed by a different physical mechanism. We fully expect, with the entropic effect not yet enforced by thermalization, the key ingredients that unite the SPT and IMT may be missing. As a result, we might expect the SPT and IMT to deviate from each other, establishing respective transition thresholds. Such topics will be explored in Chapter 6.

REFERENCES

REFERENCES

[1] A. Rúa, F.E. Fernández, and N. Sepúlveda, "Bending in VO_2-coated microcantilevers suitable for thermally activated actuators," J Appl Phys **107**(7), (2010).

[2] J.D. Ryckman, K.A. Hallman, R.E. Marvel, R.F. Haglund, and S.M. Weiss, "Ultra-compact silicon photonic devices reconfigured by an optically induced semiconductor-to-metal transition," Opt Express **21**(9), 10753–10763 (2013).

[3] M.R.M. Hashemi, S.-H. Yang, T. Wang, N. Sepúlveda, and M. Jarrahi, "Electronically-controlled beam-steering through vanadium dioxide metasurfaces," Sci Rep **6**(1), 35439 (2016).

[4] Y. Cui, Y. Ke, C. Liu, Z. Chen, N. Wang, L. Zhang, Y. Zhou, S. Wang, Y. Gao, and Y. Long, "Thermochromic VO_2 for energy-efficient smart windows," Joule **2**(9), 1707–1746 (2018).

[5] L.A. Ladd, and W. Paul, "Optical and transport properties of high quality crystals of V_2O_4 near the metallic transition temperature," Solid State Commun **7**(4), 425–428 (1969).

[6] F.J. Morin, "Oxides which show a metal-to-insulator transition at the Neel temperature," Phys Rev Lett **3**(1), 34 (1959).

[7] K. Kosuge, "The phase transition in VO_2," J Physical Soc Japan **22**(2), 551–557 (1967).

[8] Z. Tao, T.-R.T. Han, S.D. Mahanti, P.M. Duxbury, F. Yuan, C.-Y. Ruan, K. Wang, and J. Wu, "Decoupling of structural and electronic phase transitions in VO_2," Phys Rev Lett **109**(16), 166406 (2012).

[9] Z. Tao, F. Zhou, T.-R.T. Han, D. Torres, T. Wang, N. Sepulveda, K. Chang, M. Young, R.R. Lunt, and C.-Y. Ruan, "The nature of photoinduced phase transition and metastable states in vanadium dioxide," Sci Rep **6**(1), 38514 (2016).

[10] A. Sood, X. Shen, Y. Shi, S. Kumar, S.J. Park, M. Zajac, Y. Sun, L.-Q. Chen, S. Ramanathan, and X. Wang, "Universal phase dynamics in VO_2 switches revealed by ultrafast operando diffraction," Science (1979) **373**(6552), 352–355 (2021).

[11] G.A. de la Peña Muñoz, A.A. Correa, S. Yang, O. Delaire, Y. Huang, A.S. Johnson, T. Katayama, V. Krapivin, E. Pastor, and D.A. Reis, "Ultrafast lattice disordering can be accelerated by electronic collisional forces," Nat Phys **19**(10), 1489–1494 (2023).

[12] S. Wall, S. Yang, L. Vidas, M. Chollet, J.M. Glownia, M. Kozina, T. Katayama, T. Henighan, M. Jiang, and T.A. Miller, "Ultrafast disordering of vanadium dimers in photoexcited VO_2," Science (1979) **362**(6414), 572–576 (2018).

[13] J. Li, L. Wu, S. Yang, X. Jin, W. Wang, J. Tao, L. Boatner, M. Babzien, M. Fedurin, and M. Palmer, "Direct Detection of VV Atom Dimerization and Rotation Dynamic Pathways upon Ultrafast Photoexcitation in VO_2," Phys Rev X **12**(2), 021032 (2022).

[14] S. Wall, D. Wegkamp, L. Foglia, K. Appavoo, J. Nag, R.F. Haglund Jr, J. Stähler, and M. Wolf, "Ultrafast changes in lattice symmetry probed by coherent phonons," Nat Commun **3**(1), 721 (2012).

[15] L. Vidas, D. Schick, E. Martínez, D. Perez-Salinas, A. Ramos-Álvarez, S. Cichy, S. Batlle-Porro, A.S. Johnson, K.A. Hallman, and R.F. Haglund Jr, "Does V O 2 Host a Transient Monoclinic Metallic Phase?," Phys Rev X **10**(3), 031047 (2020).

[16] V.R. Morrison, R.P. Chatelain, K.L. Tiwari, A. Hendaoui, A. Bruhács, M. Chaker, and B.J. Siwick, "A photoinduced metal-like phase of monoclinic VO_2 revealed by ultrafast electron diffraction," Science (1979) **346**(6208), 445–448 (2014).

[17] M.R. Otto, L.P. René de Cotret, D.A. Valverde-Chavez, K.L. Tiwari, N. Émond, M. Chaker, D.G. Cooke, and B.J. Siwick, "How optical excitation controls the structure and properties of vanadium dioxide," Proceedings of the National Academy of Sciences **116**(2), 450–455 (2019).

[18] T.L. Cocker, L. V Titova, S. Fourmaux, G. Holloway, H.-C. Bandulet, D. Brassard, J.-C. Kieffer, M.A. El Khakani, and F.A. Hegmann, "Phase diagram of the ultrafast photoinduced insulator-metal transition in vanadium dioxide," Phys Rev B **85**(15), 155120 (2012).

[19] A.S. Johnson, D. Perez-Salinas, K.M. Siddiqui, S. Kim, S. Choi, K. Volckaert, P.E. Majchrzak, S. Ulstrup, N. Agarwal, and K. Hallman, "Ultrafast X-ray imaging of the light-induced phase transition in VO_2," Nat Phys **19**(2), 215–220 (2023).

[20] C. Xu, C. Jin, Z. Chen, Q. Lu, Y. Cheng, B. Zhang, F. Qi, J. Chen, X. Yin, and G. Wang, "Transient dynamics of the phase transition in VO_2 revealed by mega-electron-volt ultrafast electron diffraction," Nat Commun **14**(1), 1265 (2023).

[21] X. Sun, S. Sun, and C.-Y. Ruan, "Toward nonthermal control of excited quantum materials: framework and investigations by ultrafast electron scattering and imaging," C R Phys **22**(S2), 1–59 (2021).

[22] B.S. Mun, K. Chen, Y. Leem, C. Dejoie, N. Tamura, M. Kunz, Z. Liu, M.E. Grass, C. Park, and J. Yoon, "Observation of insulating–insulating monoclinic structural transition in macro-sized VO_2 single crystals," Physica Status Solidi (RRL)–Rapid Research Letters **5**(3), 107–109 (2011).

[23] Z. Tao, T.-R.T. Han, S.D. Mahanti, P.M. Duxbury, F. Yuan, C.-Y. Ruan, K. Wang, and J. Wu, "Decoupling of structural and electronic phase transitions in VO_2," Phys Rev Lett **109**(16), 166406 (2012).

[24] C.N.R. Rao, "Transition metal oxides," Annu Rev Phys Chem **40**(1), 291–326 (1989).

[25] A. Sawa, “Resistive switching in transition metal oxides,” Materials Today **11**(6), 28–36 (2008).

[26] P.A. Cox, *Transition Metal Oxides: An Introduction to Their Electronic Structure and Properties* (Oxford university press, 2010).

[27] J. Cao, Y. Gu, W. Fan, L.-Q. Chen, D.F. Ogletree, K. Chen, N. Tamura, M. Kunz, C. Barrett, and J. Seidel, “Extended mapping and exploration of the vanadium dioxide stress-temperature phase diagram,” Nano Lett **10**(7), 2667–2673 (2010).

[28] J. Cao, E. Ertekin, V. Srinivasan, W. Fan, S. Huang, H. Zheng, J.W.L. Yim, D.R. Khanal, D.F. Ogletree, and J.C. Grossman, “Strain engineering and one-dimensional organization of metal–insulator domains in single-crystal vanadium dioxide beams,” Nat Nanotechnol **4**(11), 732–737 (2009).

[29] J. Wei, Z. Wang, W. Chen, and D.H. Cobden, “New aspects of the metal–insulator transition in single-domain vanadium dioxide nanobeams,” Nat Nanotechnol **4**(7), 420–424 (2009).

[30] D.B. McWhan, M. Marezio, J.P. Remeika, and P.D. Dernier, “X-ray diffraction study of metallic VO_2,” Phys Rev B **10**(2), 490 (1974).

[31] A. Zylbersztejn, and N.F. Mott, “Metal-insulator transition in vanadium dioxide,” Phys Rev B **11**(11), 4383 (1975).

[32] J.-P. Pouget, “Basic aspects of the metal–insulator transition in vanadium dioxide VO_2: a critical review,” C R Phys **22**(1), 37–87 (2021).

[33] J.M. Longo, P. Kierkegaard, C.J. Ballhausen, U. Ragnarsson, S.E. Rasmussen, E. Sunde, and N.A. Sørensen, “A refinement of the structure of VO_2,” Acta Chem. Scand **24**(2), 420–426 (1970).

[34] J.B. Goodenough, “The two components of the crystallographic transition in VO_2,” J Solid State Chem **3**(4), 490–500 (1971).

[35] N.B. Aetukuri, A.X. Gray, M. Drouard, M. Cossale, L. Gao, A.H. Reid, R. Kukreja, H. Ohldag, C.A. Jenkins, and E. Arenholz, “Control of the metal–insulator transition in vanadium dioxide by modifying orbital occupancy,” Nat Phys **9**(10), 661–666 (2013).

[36] H.-W. Liu, W.-H. Liu, Z.-J. Suo, Z. Wang, J.-W. Luo, S.-S. Li, and L.-W. Wang, “Unifying the order and disorder dynamics in photoexcited VO_2,” Proceedings of the National Academy of Sciences **119**(28), e2122534119 (2022).

[37] R.M. Wentzcovitch, W.W. Schulz, and P.B. Allen, “VO_2: Peierls or Mott-Hubbard? A view from band theory,” Phys Rev Lett **72**(21), 3389 (1994).

[38] C. Weber, D.D. O'Regan, N.D.M. Hine, M.C. Payne, G. Kotliar, and P.B. Littlewood, "Vanadium dioxide: A Peierls-Mott insulator stable against disorder," Phys Rev Lett **108**(25), 256402 (2012).

[39] A. Liebsch, H. Ishida, and G. Bihlmayer, "Coulomb correlations and orbital polarization in the metal-insulator transition of VO_2," Phys Rev B **71**(8), 085109 (2005).

[40] V. Eyert, "The metal-insulator transitions of VO_2: A band theoretical approach," Ann Phys **514**(9), 650–704 (2002).

[41] W. Paul, "The present position of theory and experiment for VO_2," Mater Res Bull **5**(8), 691–702 (1970).

[42] C.J. Hearn, "Phonon softening and the metal-insulator transition in VO_2," Journal of Physics C: Solid State Physics **5**(12), 1317 (1972).

[43] J.D. Budai, J. Hong, M.E. Manley, E.D. Specht, C.W. Li, J.Z. Tischler, D.L. Abernathy, A.H. Said, B.M. Leu, and L.A. Boatner, "Metallization of vanadium dioxide driven by large phonon entropy," Nature **515**(7528), 535–539 (2014).

[44] N. Mott, *Metal-Insulator Transitions* (CRC Press, 2004).

[45] M. Imada, A. Fujimori, and Y. Tokura, "Metal-insulator transitions," Rev Mod Phys **70**(4), 1039 (1998).

[46] P. Jin, and S.T.S. Tanemura, "Relationship between transition temperature and x in V1-xWxO2 films deposited by dual-target magnetron sputtering," Jpn J Appl Phys **34**(5R), 2459 (1995).

[47] T.J. Hanlon, J.A. Coath, and M.A. Richardson, "Molybdenum-doped vanadium dioxide coatings on glass produced by the aqueous sol–gel method," Thin Solid Films **436**(2), 269–272 (2003).

[48] M. Marezio, D.B. McWhan, J.P. Remeika, and P.D. Dernier, "Structural Aspects of the Metal-Insulator Transitions in Cr-Doped VO_2," Phys Rev B **5**(7), 2541 (1972).

[49] F. Beteille, and J. Livage, "Optical switching in VO_2 thin films," J Solgel Sci Technol **13**, 915–921 (1998).

[50] J.H. Park, J.M. Coy, T.S. Kasirga, C. Huang, Z. Fei, S. Hunter, and D.H. Cobden, "Measurement of a solid-state triple point at the metal–insulator transition in VO_2," Nature **500**(7463), 431–434 (2013).

[51] M.F. Becker, A.B. Buckman, R.M. Walser, T. Lépine, P. Georges, and A. Brun, "Femtosecond laser excitation of the semiconductor-metal phase transition in VO_2," Appl Phys Lett **65**(12), 1507–1509 (1994).

[52] L. Vidas, D. Schick, E. Martínez, D. Perez-Salinas, A. Ramos-Álvarez, S. Cichy, S. Batlle-Porro, A.S. Johnson, K.A. Hallman, and R.F. Haglund Jr, "Does VO_2 Host a Transient Monoclinic Metallic Phase?," Phys Rev X **10**(3), 031047 (2020).

[53] X. He, N. Punpongjareorn, W. Liang, Y. Lin, C. Chen, A.J. Jacobson, and D.-S. Yang, "Photoinduced strain release and phase transition dynamics of solid-supported ultrathin vanadium dioxide," Sci Rep **7**(1), 10045 (2017).

[54] C.N. Berglund, and H.J. Guggenheim, "Electronic Properties of VO_2 near the Semiconductor-Metal Transition," Physical Review **185**(3), 1022 (1969).

[55] A. Rúa, F.E. Fernández, and N. Sepúlveda, "Bending in VO_2-coated microcantilevers suitable for thermally activated actuators," J Appl Phys **107**(7), (2010).

[56] H.W. Verleur, A.S. Barker Jr, and C.N. Berglund, "Optical properties of VO_2 between 0.25 and 5 eV," Physical Review **172**(3), 788 (1968).

[57] C. Giannetti, M. Capone, D. Fausti, M. Fabrizio, F. Parmigiani, and D. Mihailovic, "Ultrafast optical spectroscopy of strongly correlated materials and high-temperature superconductors: a non-equilibrium approach," Adv Phys **65**(2), 58–238 (2016).

Chapter 6

Nonequilibrium Physics of VO_2 Phase Transition

6.1 Introduction

In Chapter 5, I have discussed how the PIPT manifests at the late stage that can be conveniently united with the thermally induced phase transition for VO_2. Along this line, we have confirmed the cooperativity between the IMT and SPT are well maintained in the establishment of a thermal phase. Such conclusions form the basis for effective medium theory (EMT). The success EMT to explain our repetition-rate-dependent results then leave dynamics at earlier stages that do not fall under EMT as nonthermal. Among the unresolved issues, the most debated one is whether the transient or even long-lived monoclinic metallic (*mM*) phase[1–4], does appear in the process. While its presence in systems with energy and particle flows is widely reported[5–9], the persistence of *mM* lasting into the thermalized stage has been a topic of open discussion. However, the issue might be ill-posed without clarifying what *mM* phase stands for. Normally, for the equilibrium states, the symmetry group of a crystalline phase mainly concerns the preservation of atomic positions within a unit cell under symmetry operation. However, in nonequilibrium states, it is possible to maintain the average lattice parameters that define the crystalline motif for the underpinning lattice while the system undergoes structural phase transition, with the notable example of CDW formation. In such cases, one defines the structure phase transition based on order parameter given by the local distortion before and after the transition.

Here, we will take this view for the most general scenario describing the nonequilibrium VO_2 structure phase transition. It should now be evident that due to the inherent inhomogeneous

development during PIPT, obtaining the local atomic distortions form an evolving VO_2 system is not always easy. For this reason, the local atomic routes towards VO_2 phase transition remains a topic of ongoing debate, with multiple pathways proposed in the literature. Through analysis of the diffraction intensity change in reflection mode, Baum et al. suggested that VO_2 undergoes a de-dimerization process within 1 ps, followed by de-twisting over the subsequent 10 ps, and finally experiences unit cell relaxation for more than 200 ps[10]. In contrast, Li et al. presented a different atomic pathway based on their UED experiment, in which VO_2 undergoes both de-dimerization and de-twisting concurrently within the first 4 ps, followed predominantly by de-dimerization up to 800 ps[11]. Furthermore, Xu et al. conducted experiment via MeV UED and proposed yet another atomic pathway[4], concluding that the loss of twisting and dimerization occurs entirely within the first 200 fs, with unit cell relaxation taking place at 5 ps.

As in the studying of thermodynamical phase transition in bulk VO_2 samples, a challenging aspect to interpret local structural changes from the scattering probes is the local variations of transition thresholds leading to the phase coexistence at different regions and an extended transition curve at the transition threshold [4,11–14]. While most experiments focus on the diffraction peak intensity or position changes, which provide information on the averaged atomic movement across the entire sample region, recent X-ray diffraction studies[15,16], leveraging the high beam brightness from free-electron-laser-generated X-ray, have indicated that even though the final state exhibits an R structure on average, the local atomic pathways of vanadium atoms may differ significantly from the average behavior. These findings suggest that the PIPT process in VO_2 may involve more complex and heterogeneous[14] atomic motions at the local scale, which are not captured by the averaged structural information.

One key hanging question among these latest studies lies in how the electronic property will then correlate with the heterogeneous atomic motions at the local scale. In this chapter, I will delve into our approach to study nonequilibrium dynamics of VO_2 phase transition. Our approach includes more controlled study following the nonequilibrium dynamics starting from the incubational subthreshold regime to the highly excited regime that manifests in different physical mechanisms. Importantly, to piece together the physics of electronic transition and the atomic motions at the local scale, we put together a simultaneous dual-probe approach uniting the UED and ultrafast optical measurements in the electron microscope platform.

6.2. Multi-Messenger Investigations of VO_2 Phase Transition

Here we will describe the experimental setups and intricate details regarding the unification of ultrafast electron diffraction and optical differential transmittance measurements carried out to probe the ultrafast nonequilibrium dynamics of VO_2 phase transitions.

6.2.1 Dual-Probe Experiment Setup

Our experimental setup is designed to perform in-situ measurements to correlate the atomic movement and material's electronic responses. As the atomic movements may be complex and subtle, requiring specific arrangements to probe with high speed and precision, simultaneous structure and optical measurements at the same speed and high precision have not been accomplished thus far. To achieve that, a dual-probe detection system is constructed in the MSU generation-I ultrafast electron microscope (UEM-I), as shown in Fig. 6.1, where we recently upgraded its condenser RF-optics control to reach 50 fs resolution in carrying out UED (see Ch. 4) that matches the typical resolution of the optical probe (also of 50 fs considering the pump-

probe wavefront mismatch). Here, an 800 nm, 30 fs probe laser beam was employed to conduct the ultrafast optical differential transmissivity (OP-TR) measurements. The setup thus enables the tracking of the IMT process along side with structural characterizations carried out by UED.

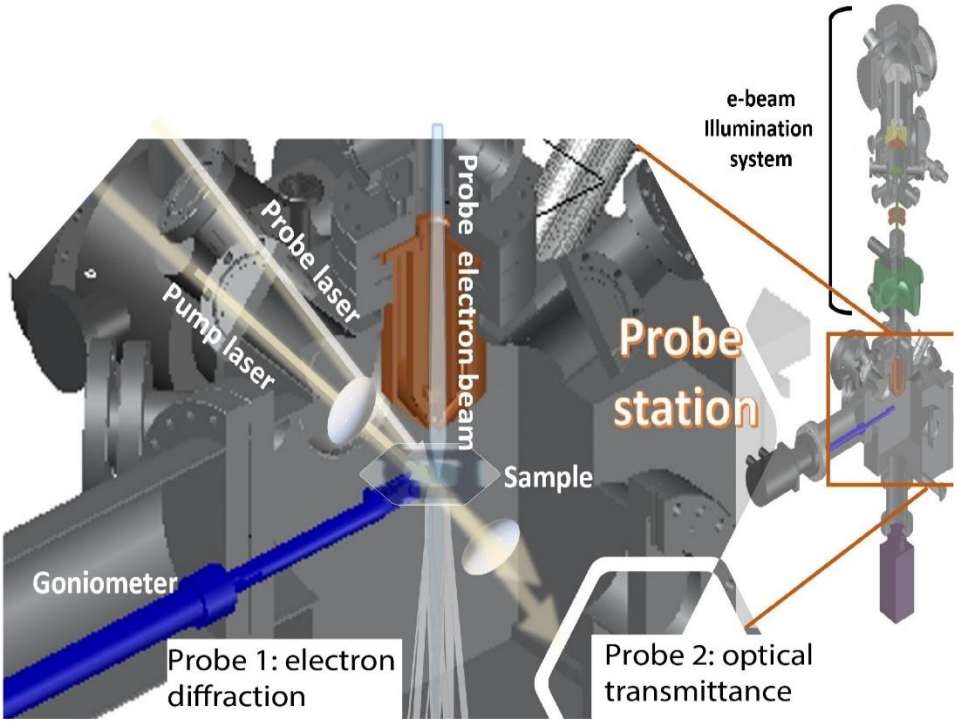

Figure 6.1. The due-probe setup in the generation-I ultrafast electron microscope system at MSU. The dual-probe setup is used to track simultaneously the light-induced changes in the structure and the optical conductivity through measuring the electron diffraction and optical transmittance signals through the thin-film specimens.

To ensure the coincidence, first the beam paths of the optical probe were adjusted such that the arrival time difference between the optical probe and the electron probe was within 150 fs. The remaining arrival time difference was compensated guided by correlating the optical and structural responses in a consistent way over a broad range of fluences. Typically, at a relatively high fluence

the signatures for simultaneous structural and optical changes can be identified clearly within 50 fs resolution. The probe beam fluence was reduced to less than 10 μJ/cm^2 to avoid any probe-induced changes to the system. To minimize the residue heating on the sample, the experiment was conducted at 200Hz repetition rate.

6.2.2. Information Channels from the Structural Probe

Below, I describe the information channels offered by UED data to obtain the corresponding local atomic and the average crystalline motif changes. Our UED experiments were conducted using 60 keV electron pulses optimized to a relatively high coherence length to resolve the fine features presented in the powder diffraction of our VO_2 samples given Fig. 6.2. From the symmetry-breaking perspective, the local anion movements as characterized by $\delta\theta$, δr that couple to thermal M1-to-R phase transition, may be regarded as the *order parameters* to discern in the diffraction pattern. Specifically, the local structural distortions lead to a doubling of the unit cell vector along the $\boldsymbol{c}_R$ axis, resulting in a new set of reflections that can be identified within the rutile Brillouin zone. These peaks can be identified by the "odd" integer number index along a_{M1} (which is the axial direction in M1). For example, in the powder diffraction (Fig. 6.1), reflections $(30\bar{2})_{M1}$, $(12\bar{2})_{M1}$ and $(31\bar{3})_{M1}$ are such symmetry-breaking peaks. On the other hand, to track the more subtle effect of the anion movement in the basal plane, we rely on reflections with high index number along $\boldsymbol{a}_R$ and $\boldsymbol{b}_R$ and a low index number along $\boldsymbol{c}_R$. However, this proves to be more difficult for powder diffractions, as such peaks, not symmetry-breaking in nature, typically lie very near high intensity reflections of the rutile lattice. Reflection $(012)_{M1}$is one such Bragg peak located very near the rutile $(002)_R$ and largely indistinguishable in prior work. Our effort in improving the resolution in the current study enables resolving such subtle reflections; see Fig. 6.1. The

usefulness of including $(012)_{M1}$ along with other symmetry-breaking reflections in our analyses is the near orthogonality of the two informative channels: the transverse displacement ($\delta\theta$) and longitudinal displacement (δr) of the zigzag chain encoded de-pairing in $(012)_{M1}$ and $(30\bar{2})_{M1}$. This near orthogonality is shown in the conversion between the intensity changes ($\Delta\hat{I}(012)_{M1}$, $\Delta\hat{I}(30\bar{2})_{M1}$) and the distortions (δθ, δr), given in Fig. 6.3. Specially, given $\Delta\hat{I}(30\bar{2})_{M1}$ exclusively depends on δr, one can figure out the paring distance change based on $\Delta\hat{I}(30\bar{2})_{M1}$ alone. By combining high-fidelity information from $\Delta\hat{I}(012)_{M1}$ and $\Delta\hat{I}(30\bar{2})_{M1}$, the twisting angle variation can be retrieved with confidence; see Appendix I for details.

Meanwhile, to retrieve the evolution of the crystalline lattice parameters, we reply on the time-dependent shift in the relative positions of Bragg reflections at $\mathbf{G_{hkl}}$ given by:

$$\mathbf{G_{hkl}} = h\mathbf{b_1} + k\mathbf{b_2} + l\mathbf{b_3}. \tag{6.1}$$

The rearrange of the crystalline lattice unit vectors $\{\boldsymbol{a_i}\}$, where i=1,2,3, are given by following the corresponding shift in $\mathbf{G_{hkl}}$ based on the reciprocal relationship:

$$\mathbf{b_i} = 2\pi\left(\frac{\mathbf{a_j}\times\mathbf{a_k}}{\mathbf{a_i}\cdot(\mathbf{a_j}\times\mathbf{a_k})}\right)\varepsilon_{ijk}. \tag{6.2}$$

More details regarding how the lattice constants are retrieved based on UED are given in Appendix I.

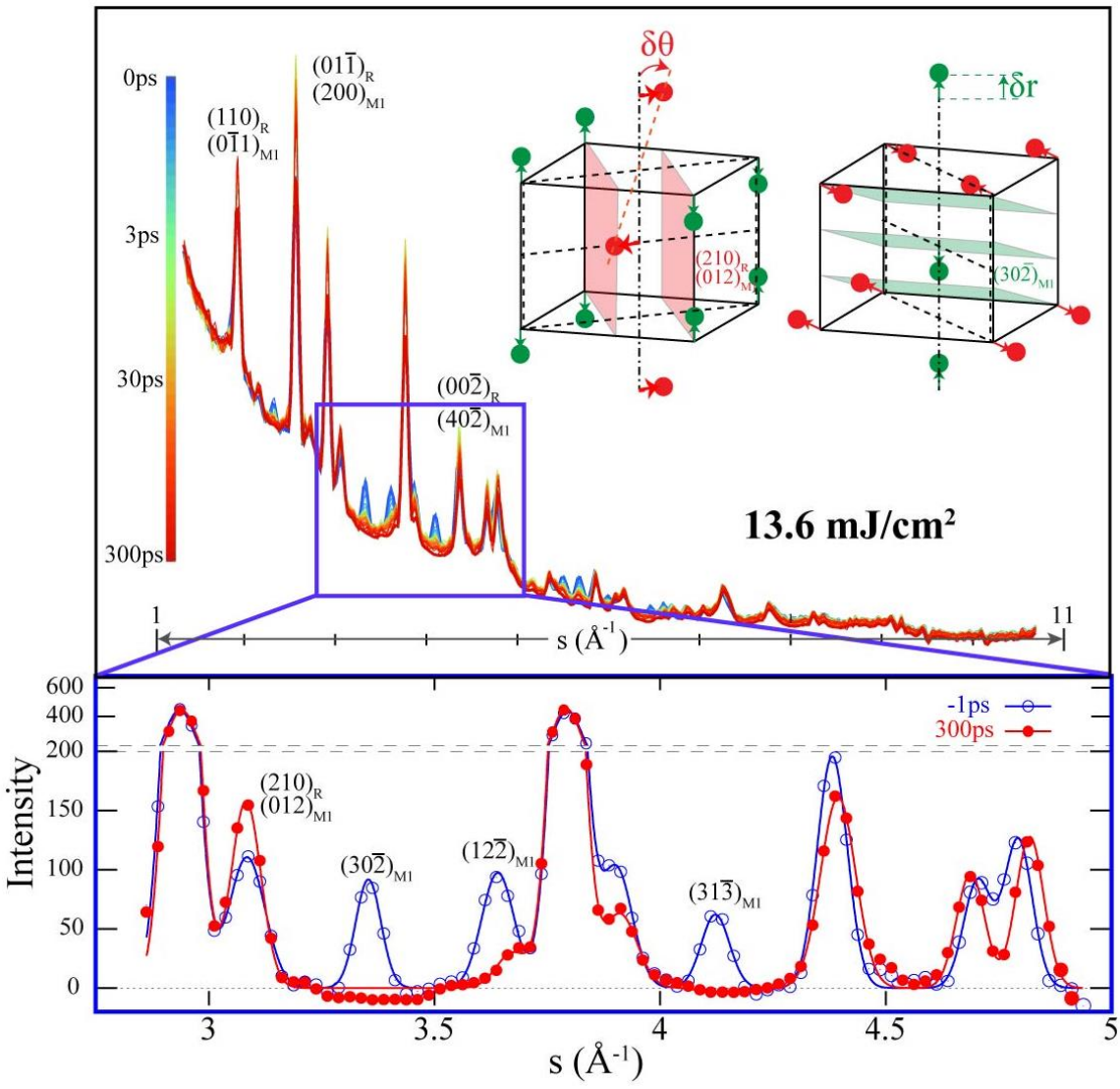

Figure 6.2. Structure dynamics of VO_2 probed by ultrafast electron diffraction. Top panel shows diffraction pattern for VO_2 after excited by 13.6mJ/cm^2 laser at first 300ps. The bottom panel shows the background removed view zoomed in for region with most obvious intensity change. the inserted panel shows two lattice plans, where their corresponding diffraction peaks, $(012)_{M1}$ exclusively tracks atoms movement in the basal plane, and peak $(30\bar{2})_{M1}$ mostly tracks atoms movement in the pairing direction.

The data presented in Fig. 6.3 show the notable intensity changes at the "symmetry-breaking" reflections. Noticeably, here phase transformation, as given by the normalized intensity change at t = 2.5 ns using the negative-time (t = -1 ps) intensity as the reference, the normalized intensity $\hat{\mathrm{I}}(012)_{M1}$ increases from 1 to 1.527 whereas $\hat{I}(012)_{M1}$ decreases from 1 to 0. These changes align well with the results from the thermally induced M1-to-R phase transition as reported in Fig. 5.5

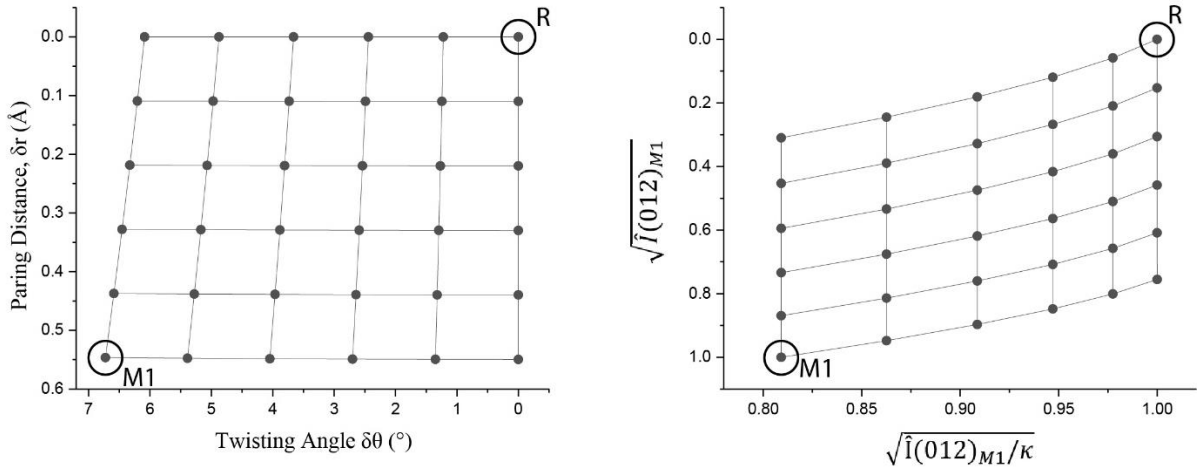

Figure 6.3. Retrieval of local structure from ultrafast diffraction signals. Right panel shows peak strength for $(012)_{M1}$ and $(30\bar{2})_{M1}$ calculated from given order parameter in the left panel. The diffraction intensity is plotted with normalization, where $\kappa = 1.527$ from the (012) peak intensity changes at phase transition.

6.2.3 Information Channels from the Optical Probe

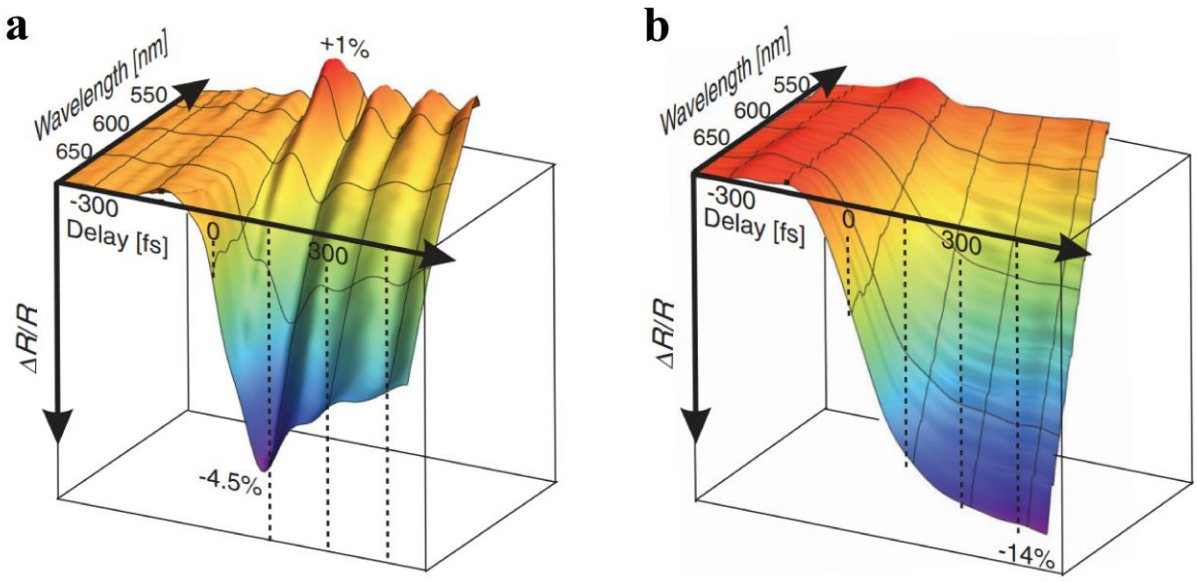

Figure 6.4. Ultrafast optical measurements on VO_2. a. Reflectivity changes from 500nm to 700nm after weak laser perturbation and **b**. After laser induced phase transition. Adapted from Ref[17].

Ultrafast optical techniques have been employed as a primary probe for the transient electronic structure changes in the studies of VO_2[18,19]. Here, we apply the 800 nm near-infrared probe with phonon energy of 1.55eV to investigate IMT. Early results show a correlation between VO_2 IMT and the disappearance of a distinct peak between 0.8 eV and 1.1 eV[20]. This reduction of ≈1eV peak was attributed to the unsplitting of the $d_{//}$ band around the Fermi level[20–22]. As such, it is expected that the transmissivity changes probed by a mid-to near-infrared wavelength probe could better reveal the changes in the free-carrier density associated with $d_{//}$ -band closing[20]. Conversely, shorter wavelengths probe the transition of electrons between the O-2p and V-3dπ states, which exhibit little change during the phase transition. This picture was corroborated in ultrafast

reflectivity measurements[17], which is reproduced here in Fig. 6.4, where an increase in the probing wavelength from 500 nm to 700 nm resulted in not only a larger change in reflectivity but also the disappearance of the signatures for phonon oscillations. This indicates that the intensity changes at even longer wavelengths, such as 800 nm (employed here), may serve as a more sensitive probe to characterize transient band-edge dynamics relevant to IMT than the shorter wavelength probes.

6.3. Signatures of Nonequilibrium Electron Dynamics and Corresponding Structural Changes

The dual-probe ultrafast measurements focus on the transient state evolution from the ultrashort timescale to the intermediate timescales, which are ubiquitous across different crystalline grains. Such dynamics, as revealed in our repetition-rate-dependent investigation, show several distinct features in the optical conductivity (Fig. 5.6), rendering the IMT process in the nonequilibrium regime differs in a significant way from those carried at the thermalized stage. The distinct features include a short-lived state with transient metallicity dominated by the hot carriers, created upon photoexcitation in largely untransformed (namely M1) region by inter-band transition (from $d_{//}$ band to delocalized orbitals). The hot carrier state would decay rapidly given the sub-ps electron-hole recombination generally expected within the insulating ground state. Second, the dynamics at the intermediate times (up to several hundred ps) give the linear log-time response, which is a signature of metallic domain growth, Such dynamics would eventually lead to a transformation of the entire M1 grain into the R state, in population α_{M1-R} selected by EMF. Interestingly, the linear log-time behavior is an indication of universal dynamics in the percolation of the metallic puddles, subject to the dimensionality of the active system. Finally, between the rapidly relaxing hot carriers

and the formation of R domains, the optical conductivity is substained by an intriguing intermediate metallic state, characterized by its much larger decay time typically several ps or longer. Such dynamics is associated with polaron formation, which is not surprising as small polaron effects have been well discussed in the transport studies across transition-metal oxide materials[23]. Here, the enhanced optical conductivity reflects how an activated polaron can delocalize driven under nonequilibrium condition – a topic will be further discussed below. The general assignments of the three dynamical channels are given schematically over three distinct timescales of evolution, as presented in Fig. 6.5.

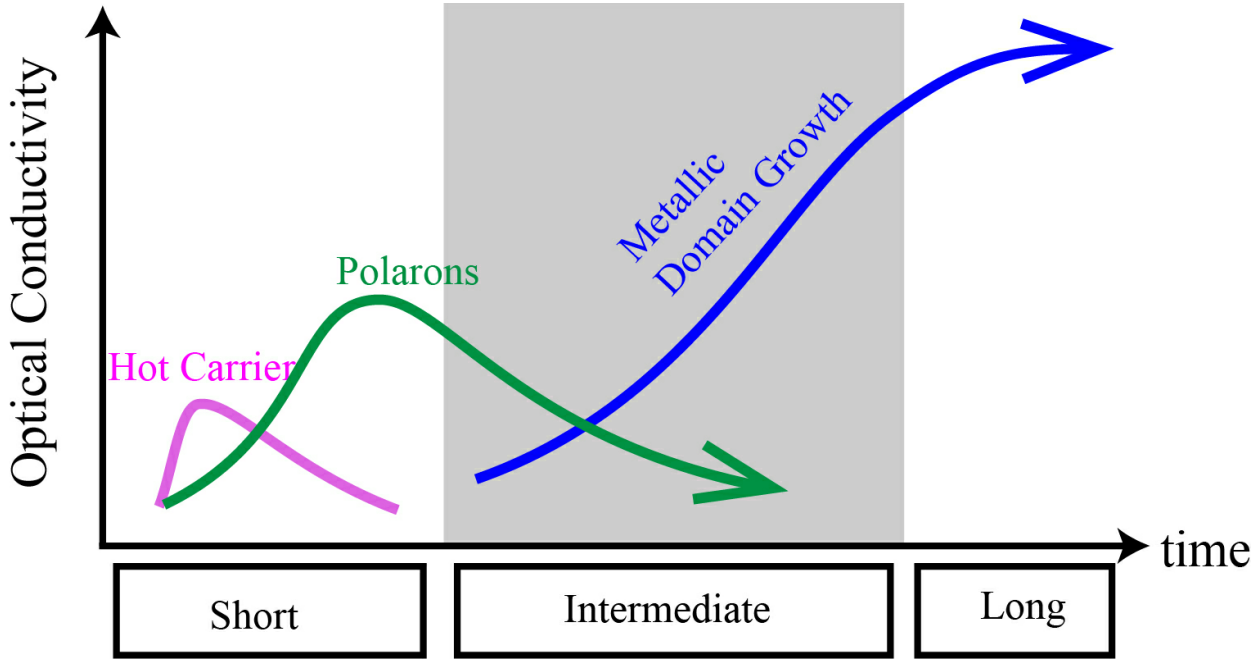

Figure 6.5. The main active dynamical channels contribute to the general dynamics at the nonequilibrium timescales.

6.3.1 Correlation Between Optical and Diffraction Data

Here, with the dual probe, we follow such general features at the nonequilibrium timescales over a broad range of laser fluences. We confine the f_{rep} to 200 Hz to avoid residual heating effect. The results depicted in Fig. 6.6 build on the optical conductivity to show the general trend of evolution. Based on the characteristic timescales for distinguishing the three dynamical channels, we outline their most active regions by the color codes. Notably, the hot carriers are shown as the most dominant channel at low fluences when the system over the short timescale remains largely in the insulating ground state. Its relative contribution wanes as the fluence increases. On the other hand, the formation of polarons, which coexist with the hot carriers initially, will persist into longer timescales. This is shown in the green colored region with continuing growth of such contribution to the optical conductivity as the fluence increases. Finally, the metallic domains, distinguished by their linear log-time growth process, is the most distinguishable channel of growth. Formation of metallic puddle is not instantaneous, marked by a varying onset time. Notably, upon increasing in fluence, the onset time moves to an earlier timescale as the dynamics pick up speed.

It is essential to point out, as argued on the grounds of EMT, the general nature of such ultrafast dynamics is independent of the strain field being present. Since the strong cooperativity between IMT and SPT and their distinctive joint transition threshold subject to tuning under stress are the hallmarks of thermally induced phase transition, we expect a new organizing principle emerges here at the ultrashort and intermediate times. The non-joule heating characteristic is most evident by the observation of a distinct “density dependence”, namely a clear cut-off in fluence that makes the system as being an insulator or a conductor, even before the embryonic R domain is introduced. A clear-cut fluence based on the differential transmissivity development trend, e.g. the differential transmissivity switches from being negative to positive, can be spotted at $F_C \sim$ 4.5

mJ/cm^2. We note, give the large scale shift in conductivity (up to serval orders of magnitude) in the fully developed R phase, which corresponds in totality a 33% change, the few percentage variation witnessed at the transient times is a significant IMT switching to drive an optical device performance; see Refs.[24] and[25] for examples.

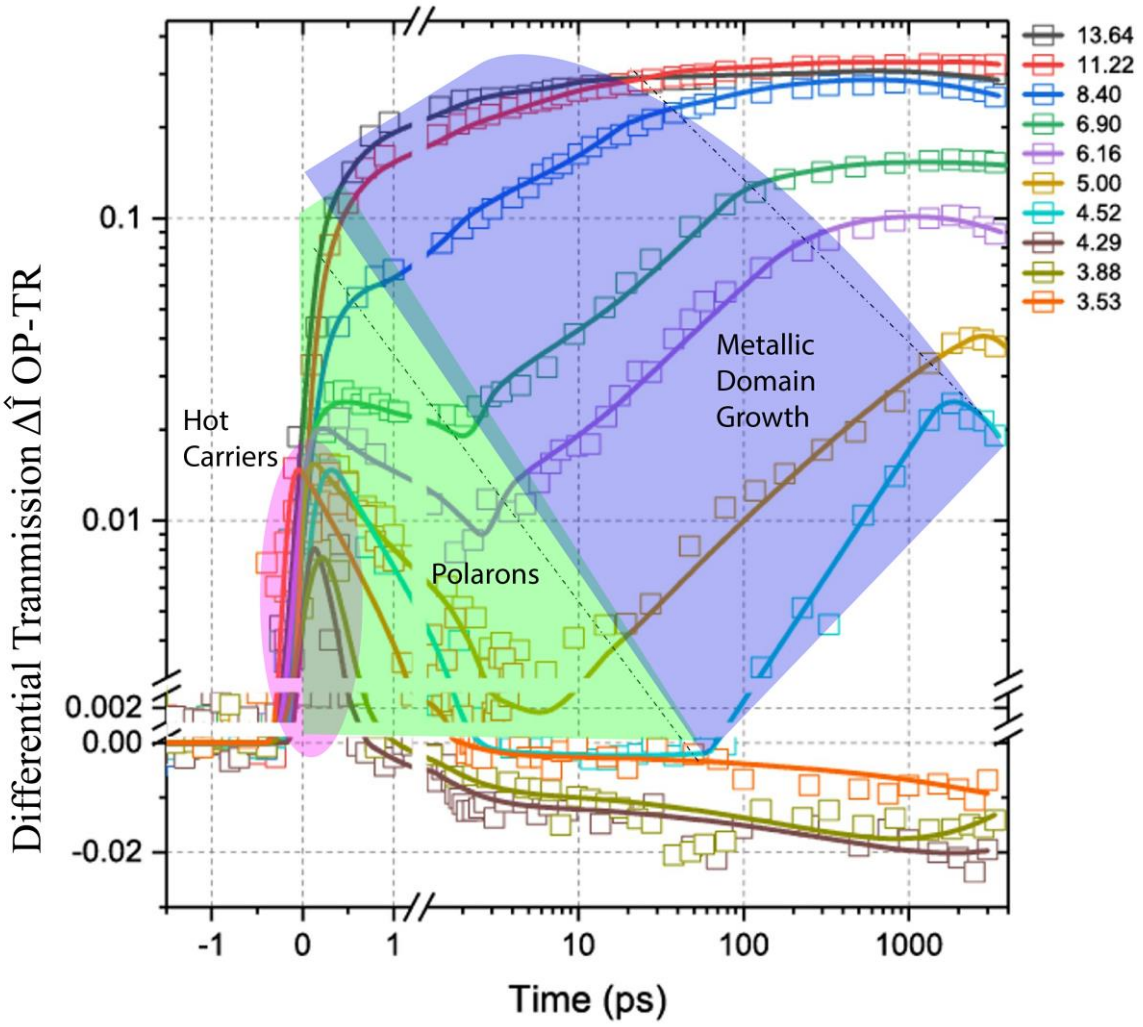

Figure 6.6. Fluence-dependent optical differential transmittance dynamics. The three main dynamical channels given by the hot carriers, polaron formation, and the metallic domain growth are identified based on their characteristic dynamical signatures in different colors.

We must turn to the corresponding structural changes as identified by UED to corroborate our understanding of the elementary optical responses represented by the three dynamical channels. This is especially important for the assignment of the intervening polaronic state underpinned by the dressed photoexcited hole populations. Additionally, the growth of the rutile metallic domain across the system, permitted under the stress regulation should be detected by UED. The impact on the structure dynamics by hot carriers remain an intriguing subject for correlated electron materials.

We first present the results given by the two order-parameter-informing reflections $(012)_{M1}$ and $\Delta\hat{I}(30\bar{2})_{M1}$, as shown in Fig. 6.6 as an exemplary case. The data ae plotted in normalized intensity changes $\Delta\hat{I}(012)_{M1}$, $\Delta\hat{I}(30\bar{2})_{M1}$, which directly inform the dynamics of $\delta\theta$, δr (see Fig. 6.2) that are driven under the applied fluence of 6.1 mJ/cm^2. By assuming linear response, the despairing and detwisting are correlated with the gap dynamics – especially intensity signal from $\Delta\hat{I}(30\bar{2})_{M1}$ are relevant to the splitting of $d_{//}$ band. Such phenomenon is typically driven by the competition between on-site Coulomb energy and the itineracy altered with the V-V bond distance changes mediated by the strong d-electron-lattice interaction. Meanwhile, from change in $\Delta\hat{I}(012)_{M1}$ the impact from the shifting alignment between the O-2p and V-3d orbitals informed by the twisting angle can be evaluated.

The respective effects are tracked here based on the comparing the two structural modalities, give by $\Delta\hat{I}(012)_{M1}$, $\Delta\hat{I}(30\bar{2})_{M1}$ with the observed optical conductivity given by $\Delta\hat{I}_{OP-TR}$. A high level of positive correlation between a specific structure dynamics and optical conductivity would infer whether the $d_{//}$-band unsplitting or the V-O hybridization is more directly responsible for inducing ultrafast IMT. We designate the dynamics pertaining to hot carriers, polarons, and metallic domains as channels A, B, and C. The comparison is carried out by fitting the data with

the three channels described by the dynamical models to capture the respective relaxation times given by:

$$A(t) = e^{\frac{-t}{\tau_1}}\Theta(t),$$

$$B(t) = \frac{\tau_3}{\tau_2-\tau_3}(e^{-\frac{t}{\tau_1}} - e^{-\frac{t}{\tau_2}}), \tag{6.3}$$

$$C(t) = c_0\left(\frac{t-t_{onset}}{\tau_4} + 1\right)^{d/2}\Theta(t - t_{onset}),$$

where the three channels are combined with individual weighing factor α, β, γ :

$$\Delta\hat{I}(hkl)_{M1} = [\alpha\, A(t) + \beta B(t) \; + \gamma C(t)]. \tag{6.4}$$

to compare with the results.

The trend of the fluence dependence in the optical signals contributed by the 3 channels are evaluated via fitting. We find, based on fitting the results in Fig. 6.7 given for the general survey, there is almost no variation regarding the hot carrier relaxation time τ_1 = 1 ps (here the rise time of hot carriers are within the resolution limit of 50 fs). Similarly, the polaron formation and relaxation timescales are generally determined to be τ_2 = 0.3 ps and τ_3=8.6 ps, for fluence between F_c and F_{th}. Meanwhile, the characteristic time scale for the metallic domain growth (τ_4) given by channel C varies significantly. Here, we define c_0 as the initial domain size and t_{onset} as the incubation time for the growth with exponent $d/2$, where d is the dimensionality for the domain growth. These modelled dynamics are convoluted with the response function, modeled as a Gaussian with FWHM of 50 fs, to take into account the finite resolution of the probe. It is intriguing to point out the dynamics associated with the domain growth throughout $F > F_c$ are well captured with an exponent ½. This suggests the domain growth follows universal dynamics with d=1. The only relevant length scale is given by the correlation length $\xi = \sqrt{D(t - t_{onset})}$, where D is the diffusion constant[26].

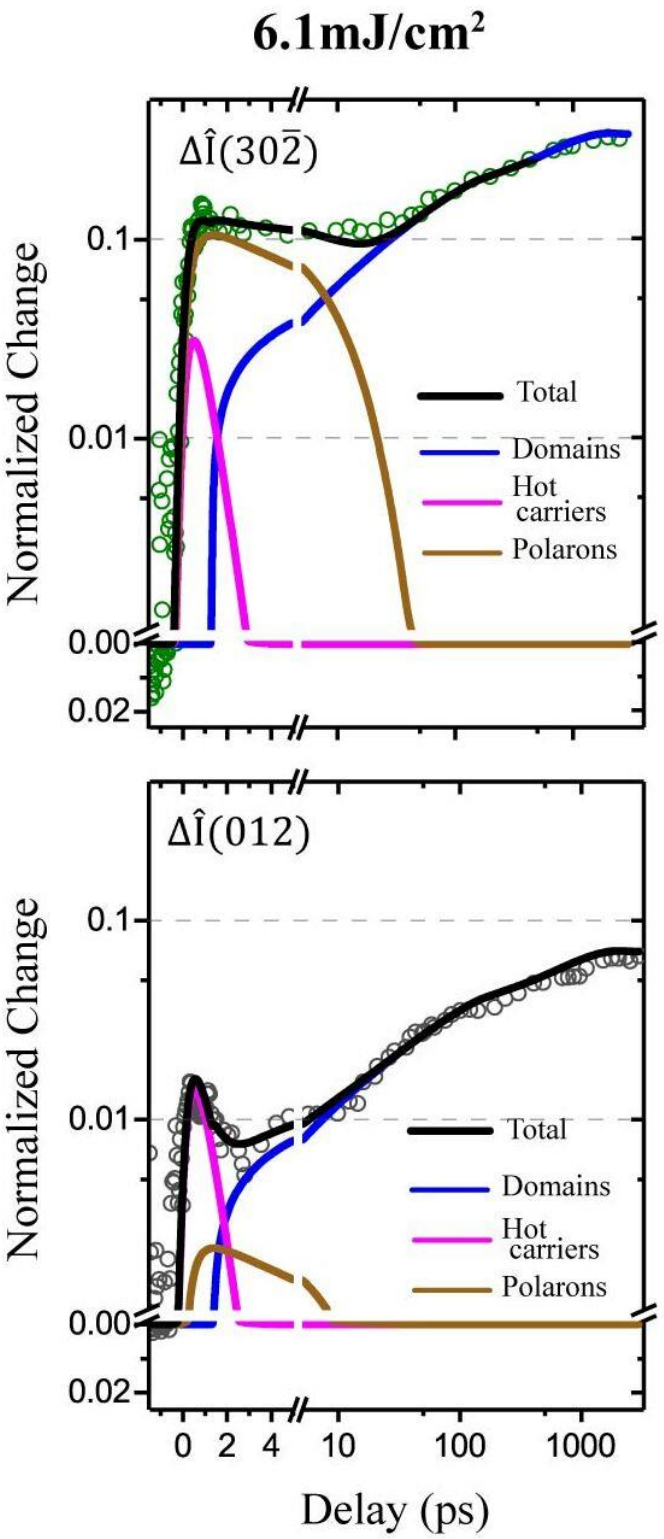

Figure 6.7. The three-component fitting carried out for diffraction signals from $(30\bar{2})$ and (012) reflections obtained with UED.

Based on the retrieved timescales given by fitting the optical data, we can now identify the respective channel contributions in the structure dynamics along the two order parameters. The results are presented in Fig. 6.7 where the distinct difference in the values for α, β and γ retrieved from the UED are detected. Interestingly, we identify the basal plane dynamics, as informed exclusively by $\Delta\hat{I}(012)_{M1}$, are sensitive to the hot carrier dynamics, whereas little change can be observed over the axial dynamics given by $\Delta\hat{I}(30\bar{2})_{M1}$. This distinction is intriguing given the large photon energy (1.55 eV) for such excitation. A rational explanation can be rendered by arguing that the 1.55 eV optical excitation could already access the unoccupied hybridized V3d-O2p anti-bonding orbitals impacting the twisting angle. Yet, the larger level of sensitivity shown in the axial V-V distance change implies the hot carrier generation does relatively little to alter the $d_{//}$-electron-lattice coupling. Instead, the main effect is seen in the polaron formation directed along $\Delta\hat{I}(30\bar{2})_{M1}$, but not along $\Delta\hat{I}(012)_{M1}$. These complementary responses from the two order parameters thus point to the polaronic effect, caused by charge screening of the photo-excited d-holes, is carried out by the $d_{//}$-band electrons that shifts the local $d_{//}$-electron-phonon interaction. Over a longer time, the metallic puddles are formed and couple to both detwisting and despairing channels.

To evaluate the relative contributions to the metallicity, the relative α, β and γ values are compared. We find the ratios of γ between the optical and the two structural channels remain constant across all fluences above F_{th}. Furthermore, the agreement between the two structure channels and the optical signal from the intermediate period to the eventual R phase are excellent after applying the scaling factor, given by the γ ratio. This confirms that the local metallic puddles already exhibit the thermal R phase characteristics as they percolate into larger and larger domains. However, a different scaling factor needs to be applied to the shorter timescale to match the optical

data to $\Delta\hat{I}(30\bar{2})_{M1}$, which is dominated by polaronic state. No good match between the optical data and $\Delta\hat{I}(012)_{M1}$ can be carried out on the short timescale. The excellent agreements during these two stages of evolution can be found by applying the same two scaling factors values across all applied fluences above F_c; the detailed results are given in Appendix II. The remarkable agreement between the optical signal and the UED data over the two stages of evolution across a broad range of fluences is a strong indication that distinct but different phases are developed at the short and longer time periods.

6.3.2 Ultrafast IMT: the Formation of Monoclinic Metallic State

We present the case for ultrafast IMT accompanied by structural transformation from the M1 to the polaronic state. Such dynamics is best depicted in the higher fluence regime, given in Fig. 6.8, where we present the optical transmissivity data along with the two structural modalities. WE note the different scaling factors applied to match the optical data between the two structure modalities, and in the long and short times, At these two high fluences, the agreement between $\Delta\hat{I}(30\bar{2})_{M1}$and differential optical transmissivity is particularly noteworthy. We note the $\Delta\hat{I}(30\bar{2})_{M1}$ caries exclusively the depairing dynamics, whereas $\Delta\hat{I}(012)_{M1}$is informative of the detwisting with a limited sensitivity to depairing, It is thus evident that as one pushes the fluence pass F_{th}, a new nonthermal IMT route is well established at short time, by the system achieving degeneracy in the V-V bond order, leaving the zigzag features largely untouched. It is important to point out that twisting alone is sufficient to maintain the lattice doubling characteristic, sustaining the larger monoclinic unit cell. Hence, we may ascribe the new transient monoclinic state with unpaired zigzag sublattices has obtained the metallic state status and may be legitimately referred to as the monoclinic metallic state.

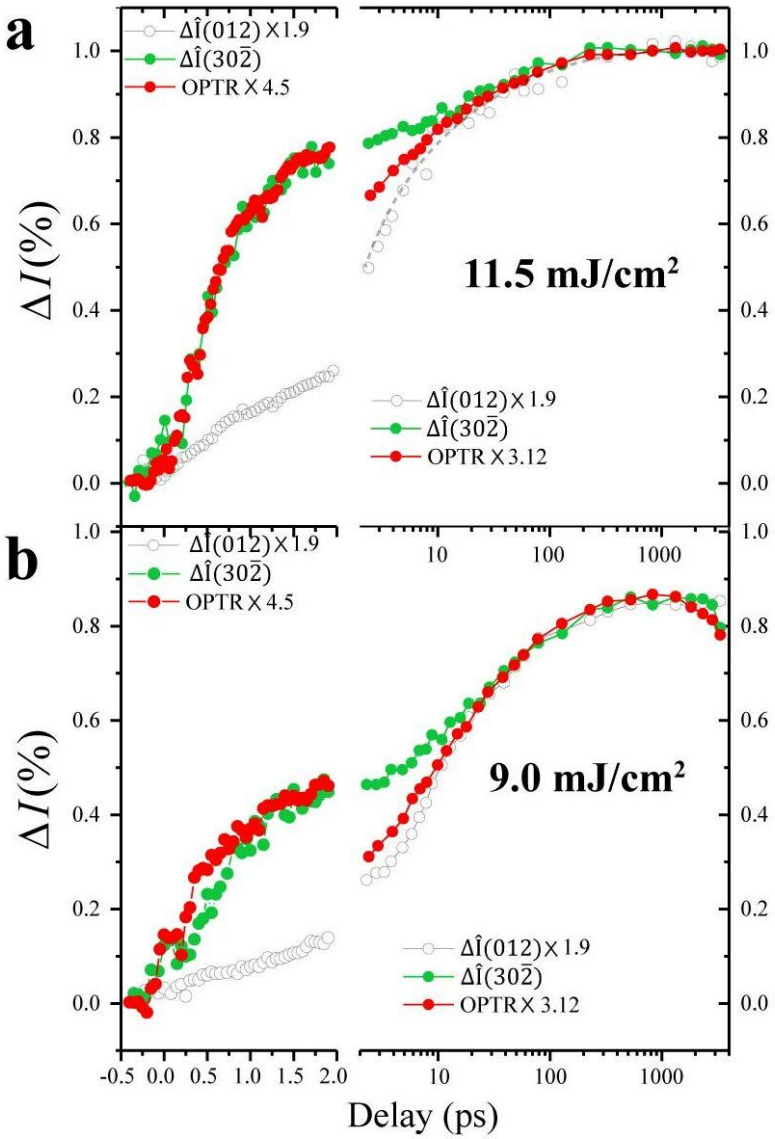

Figure 6.8. Direct comparison of the dual-probe results at two different fluences. **a**. The dynamics obtained at F=11.5 mJ/cm^2. The plot is organized to highlight changes over the short and the long timescales that are separated by the matching factors to correlate the $\Delta\hat{I}(012)_{M1}$, and the optical differential transmittance signals to $\Delta\hat{I}(30\bar{2})_{M1}$. Notably, a larger factor is needed for the matching of optical data at the short timescale. Given the disparity between two diffraction data, no attempt to match the short time data from $\Delta\hat{I}(012)_{M1}$ and $\Delta\hat{I}(30\bar{2})_{M1}$. **b**. Similar dynamics presented for F=9.0 mJ/cm^2 without changing the matching factors.

We now corroborate this observation by analyzing the mean lattice parameters using the information from the position of the main Bragg reflections. The results are given in Fig. 6.9 based on the dynamics obtained under the fluence of 13.64 mJ/cm^2. Following the protocol given in Sec. 6.2.1, we retrieve the lattice constants at 1.7 ps, 450 ps, and 2.5 ns. Here, we compare the transient lattice motif with the static unit cell structure for M1 and R phases, which are depicted using the black dashed box and the red dashed box respectively. The unit cell distances are given for the $\mathbf{c}_R$ and $\mathbf{b}_R$ directions; the change in *a* is not shown given the twofold degeneracy in the unit cell length along the $\mathbf{a}_R$ and $\mathbf{b}_R$ directions for both M1 and R structures. We take the assumption that this degeneracy within the basal plane will not be broken during PIPT in our analyses and we report the lattice evolution for unit cell lengths along $\mathbf{c}_R$ and $\mathbf{b}_R$ directions. The lattice constants for M1 and R states are marked using the data reported for the bulk single-crystal M1[27] and R[28] systems. They serve as valuable reference points given the scope of lattice strain variation, informed by the scale of transition curve broadening, is no more than 0.4%. We note that the near equilibrium structure at the very late stage (t= 2.5 ns) does develop a very similar crystalline motif as that of the thermal R phase treated based on the percentage change from the initial state taken as with the canonical M1 motif; see the data at 2.5 ns where PIPT result give nearly identical *a*, and *c* compared to the quoted lattice constants for R phase. It is interesting to point out that even at a fluence as high as 13.64 mJ/cm^2, the unit cell does not significantly deviate from the initial crystalline motif (M1) as late as 450 ps – a timescale where the local structures based on the intensity data points are fully relaxed into those characteristic of the R phase, namely untwisted and unpaired. From structure dynamics perspective, the symmetry recovery proceeds at much faster pace at the local level than those occurring to reduce the crystalline motif to the symmetric phase.

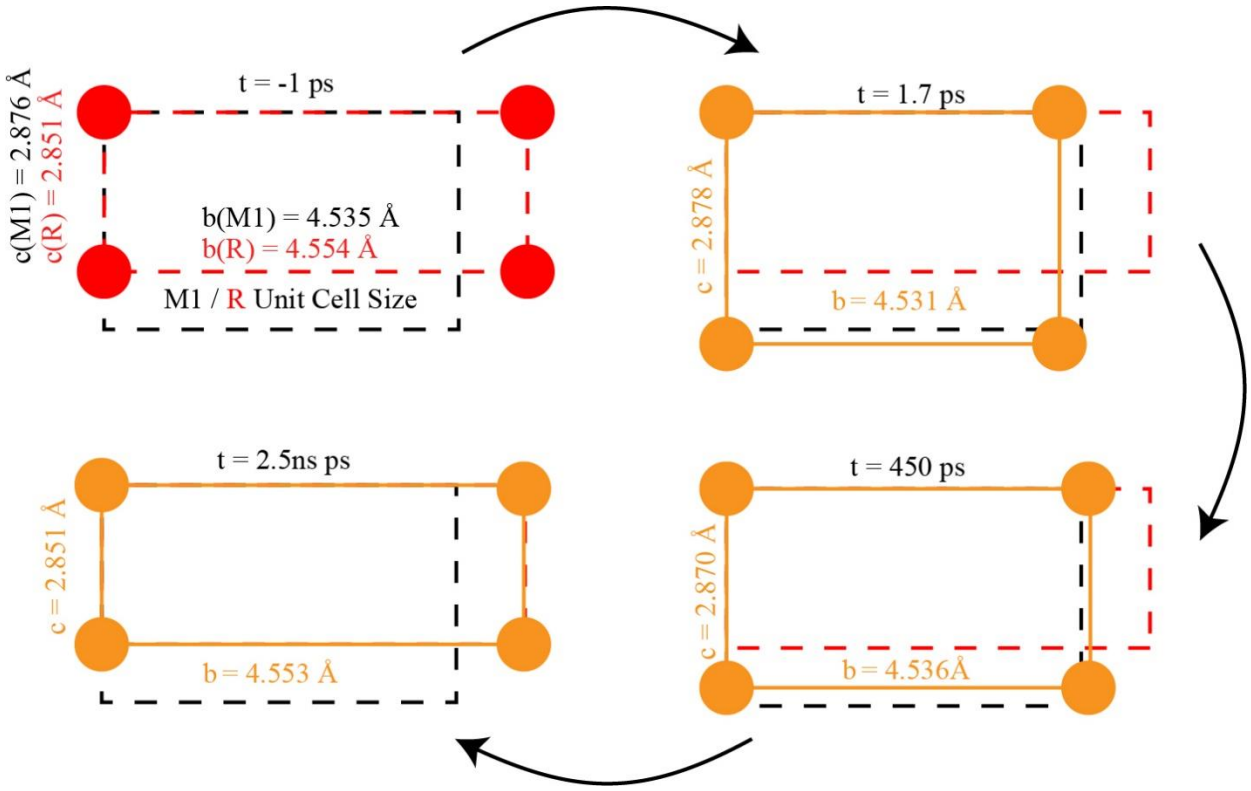

Figure 6.9 VO_2's unit cell motif changes at selected time after excited by 13.64mJ/cm^2 laser.

6.4. The Evolutionary Nature of VO_2 Phase Transition

Based on the structure analyses provided above, we may confidently proclaim indeed the establishment of the long thought-after monoclinic metallic state, serving as the doorway state for ultrafast nonthermal IMT. As the dynamics described in the nonequilibrium regime is ubiquitous, as opposed to the thermally mediated regime subject to the regulation by local strain, the result indicates a transformation of the underlying physics from the nonequilibrium to the equilibrium regimes. Such transformation carries the key to understanding the fundamentally competing physical mechanisms at play but are obscured in the thermal transition where larger fluctuations in the lattice field may obscured the interaction-mediated driving force behind the phase transition.

We are now trying to reconcile how the entire system evolves from the nonequilibrium to the equilibrium regimes. As pointed out earlier, during the nonequilibrium transition, all the untransformed region – not restricted to the just portion (α^{0}_{M1-R}) ruled by EMT, can be propelled into a new metallic state. Nonetheless, there is a natural selection step, where the effect of local strain kicks in, to decide which population will continue to make its way towards R and which will not. The basic idea behind this is schematically depicted in Fig. 6.10, where all three local phases: M1, *mM* and R are depicted, differentiated by the colors: blue, purple, and red. Irrespective of the grain size, upon photoexcitation, the *mM* state quickly developed around the photo-doped regions. Structurally speaking, the *mM* state is an intermediate phase between the canonical M1 and R phases with all of its sublattice chains depaired while maintaining the twisting. Interestingly, this reminds us another intermediate phase M2, where 50% of its sublattice is similar to *mM*, while the other 50% has the opposite fully detwisted structure but maintaining the dimerization with even larger pairing distance [29]. The M2 phase is a prototypical Mott insulator.

The evolutionary process for these competing states can be described by their respective population dynamics, irrespective of fluence applied, the dominant mM caries the metallicity initially must be either eventually be absorbed back to the background M1 lattice or be superseded by the thermal metallic R puddle formation as such new phase gains weight from the percolation process. This natural selection must take place at the intermediate stage where there is a complex coexistence of the two local states. Several pieces of information come together to illustrate this by examining the ensemble averaged differential optical signals, specially by looking back at the dynamics from the standpoint of thermal phases by evaluating the transient populations of the three active states. Taking the results from Fig. 6.8a, as an example, the entire system here under the fluence of 11. 6 mJ/cm^2 (>> F_{th}) will eventually be transformed into the R phase, but at the ultrafast

period (t <1 ps) it is entirely in the *mM* state. We can gauge the population dynamics of the two transient states *mM* and R, denoted by $\alpha_R^*(t)$ and $\alpha_{mM}^*(t)$. Under our experiment condition, α_{mM}^* start as 1, namely all the initial population of M1 are promoted into *mM* state under this relatively high fluence. However, even at this full occupancy, the level of optical conductivity gained from de-pairing all sub-lattice chains is ~ 65% of what can be accomplished in a thermal phase transition, where both $\delta\theta$ and δr are fully relaxed – which is not insignificant considering the orders of magnitude changes represented by thermally mediated switching. The transition from *mM* to metallic R phase starts off by gaining de-twisting in the *mM* state, reflected in the $\Delta\hat{I}(012)_{M1}$ (gray symbols). The data shows the three dynamical channels merge into one over the timescale of ~ 10-15 ps. From 2-10 ps, the system is in a state of complex coexistence. After 15 ps, the entire dynamics can be characterized by thermal nucleation growth.

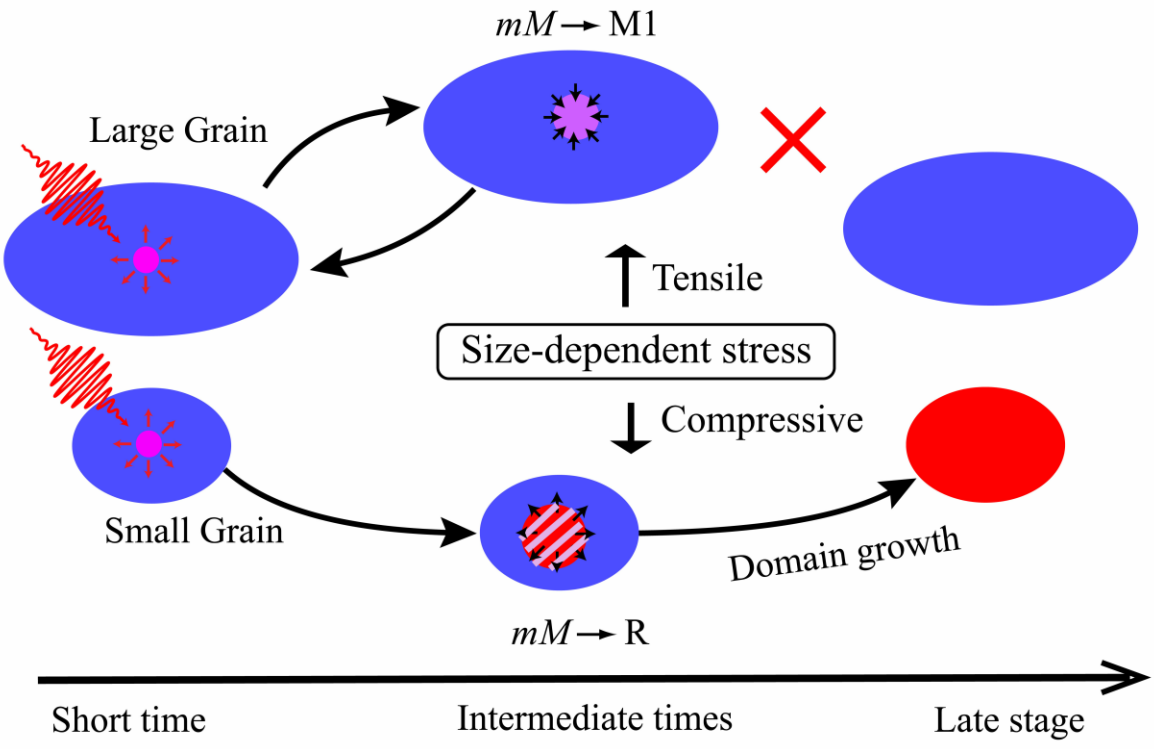

Figure 6.10. The evolutionary process of insulator-metal transition going from the nonequilibrium to the equilibrium regimes.

Based on the population dynamics, we can apply the concept of EMT into the nonequilibrium regime. This time, via tracking the active $\alpha_{mM}^{*}(t)$ – the population of mM state at the short time, and $\alpha_{R}^{*}(t)$ – the population f the metallic R puddles at the intermediate times. One could track the initial population of *mM* based on $\Delta I(30\bar{2})_{M1}$ at *t*=700 fs, as shown in Fig. 6.11, which nearly linearly increases with fluence in terms of $(F - F_c)$ as given in upper panel of Fig. 6.11. The trend terminates at 11.2 mJ/cm^2, which is an indication that *mM* state now occupies the entire untransformed region, i.e. $\alpha_{mM}^{0} = 1$. Based on this, we could now determine the effective fraction $\alpha_{mM}^{0}(F)$ to be proportional to *F* before reaching saturation and apply it to normalize the changes obtained from $\Delta\hat{I}(012)_{M1}$ and $\Delta\hat{I}(30\bar{2})_{M1}$ to obtain the local structures as a function of *F*. Here, the *mM* initial population can be set by following the density dependence. For forming the *mM* state, each photodoped impurity should give a cross-section area for its impact, which is the local polaron size, of order a^2. This sets the volume fraction of the polaron pocket $\alpha_{mM}^{0} = n_d p a^2$, with p being the correlation length of the polaron along the zigzag chain and n_d is the doping density. Given the crystalline domain exhibits the one-dimensional power-law growth, it is reasonable to assume dynamics at different chains are uncorrelated; hence, we take *a* to be the basal plane unit cell size. By setting α_{mM}^{0}=1 at *F* = 11.2 mJ/cm^2, we obtain *p* = 18 Å (covering 13 vanadium atoms along the V-V chain) based on the $n_d = 0.249\ \frac{photon}{nm^3}$ given by the saturation fluence. Similar argument can be given to the R-state population, based on the nucleation growth.

The lower panel of Fig. 6.11 presents the local structures after applying the transient EMT. The analyses, carried out by assuming the same *p* = 18 Å across all fluences above F_c, give the polaronic local structure a universally large twisting angle ($\delta\theta$ > 5 degree) whereas its pairing distance rapidly decreases as the fluence increases. This would suggest a reduction in the gap size, or an increase in optical conductivity, takes place as fluence increases. Alternatively, one may also

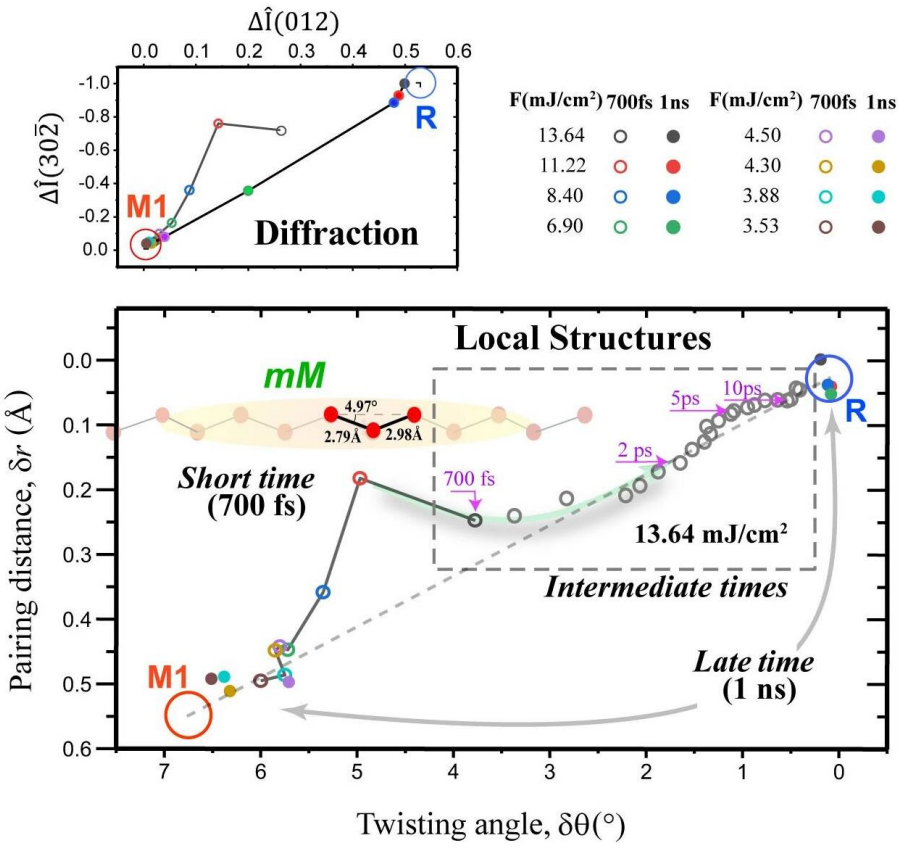

Figure 6.11. Fluence-dependent structure evolution. The upper panel shows the mean normalized intensity changes along the two key dynamical channels $\Delta\hat{I}(012)_{M1}$ and $\Delta\hat{I}(30\bar{2})_{M1}$, which yield the information about the local structures characterized $\delta\theta$ and δr pertaining to the two V-V zigzag sublattices in VO_2 under various fluences. The lower panel presents the results of the local state structures characterized by ($\delta\theta$, δr) after considering the effective medium fraction given for the initial polaronic state at the short time (t=700 fs) and that of the thermal state at the late stage (t=1ns). Here, the distinct local structure obtained following an ultrafast IMT may be referred to a transient *mM* state, which cannot be classified by any of the thermal phases in the equilibrium phase diagram of VO_2. The data presented in the inset show structure evolution in the intermediate timescale, going from *mM* structure into the thermal R structure. Meanwhile, the fluence-dependent results also show clear bi-stability between the thermal R and M1 phases at the late stage.

assume a reduced gap size characteristic of the conductive mM is retained within each polaronic pocket, namely the polaronic state starts out fully unpaired. Then one would conclude polaron correlation length p increases with fluence. That is, the localized state becomes more extended as the system becomes increasingly metallic overall.

Now we examine the evolutionary process going from the *mM* state to the thermal R state at the intermediate time. The results are presented as the inset in Fig. 6.11, given for F = 13.6 mJ/cm^2. Since we know that at this fluence, the *mM* state has filled the entire space initially, the dynamics depicts the transformation process of the local structures, as shown in grey circles. We draw the diagonal line representing the cooperative pathway, namely de-pairing and de-twisting dynamics taken simultaneously, in the thermal transition as a reference path. We find that at this heightened fluence regime, the *mM* can quickly relax into the thermodynamic path in just 2 ps, largely by reducing the twisting angle. Interestingly, this corresponds in the dynamics corresponding to timescale where all three dynamical channels merge into one as the thermodynamic effect starts to take shape. However, we do point out that at lower fluences, as given in Fig. 6.7, this transformation could take a significantly longer time as the fluence is reduced.

Now we examine the evolutionary process going from the *mM* state to the thermal R state at the intermediate time. The results are presented as the inset in Fig. 6.11, given for F = 13.6 mJ/cm^2. Since we know that at this fluence, the initial mM state has filled the entire lattice, the dynamics represent the evolution of the local structure, as shown in grey circles. We draw the diagonal line representing the cooperative pathway between de-pairing and de-twisting dynamics expected in the thermally induced M1 → R transition as a reference path. We find that at this high heightened limit, the mM initial state relaxes into the thermodynamic path in just 2 ps, largely by

reducing the twisting angle. Interestingly, this corresponds in the dynamics corresponding to timescale where all three dynamical channels merge into one as the thermodynamic effect starts to take shape. However, we do point out that at lower fluences, as given in Fig. 6.7, this transformation could take a significantly longer time as the fluence is reduced.

We now attempt to analyze the physics behind the nonthermal and thermal routes of transitions. The results presented so far may lead us to confront with two irreconcilable realities in terms of what is really behind the insulator-metal phase transition in VO_2 at the short and longer timescales. The key to unpacking this perplexity lies in the fluence-dependent data sets that give information about the competing nature of the two driving forces active at different spatial and temporal scales. The results identifying the different organizing principles at two distinct thresholds are given in Fig. 6.12. Here, first we take a closer look at the shift of the optical conductivity around Fc. Above Fc, we have taken the view the positive differential optical conductivity is given by the extended polaronic state. It is instrumental to mention that our data, see e.g. Fig. 6.11, also show that right below F_c the lattice settles in similar local polaronic features, i.e. dimerized away from M1 with large twisting angle, but to a much lesser degree overall compared to ones at $F > F_c$.

It is reasonably to believe that the increased "negative" differential transmissivity as applied fluence approaches F_c from below is physically not compatible with having more conductive channel as would be expected from introducing any sort of polaronic pocket that must come with an increased free carrier density at the outset. It is more likely that the optical excitation has led the system to a state of mass enhancement, which can be reconciled with a Mott transition. The basic picture of a Mott transition is described in Fig. 6.12c, where below Fc the system is described as a Mott insulator whereas above it a novel or bad metal state – a notation often

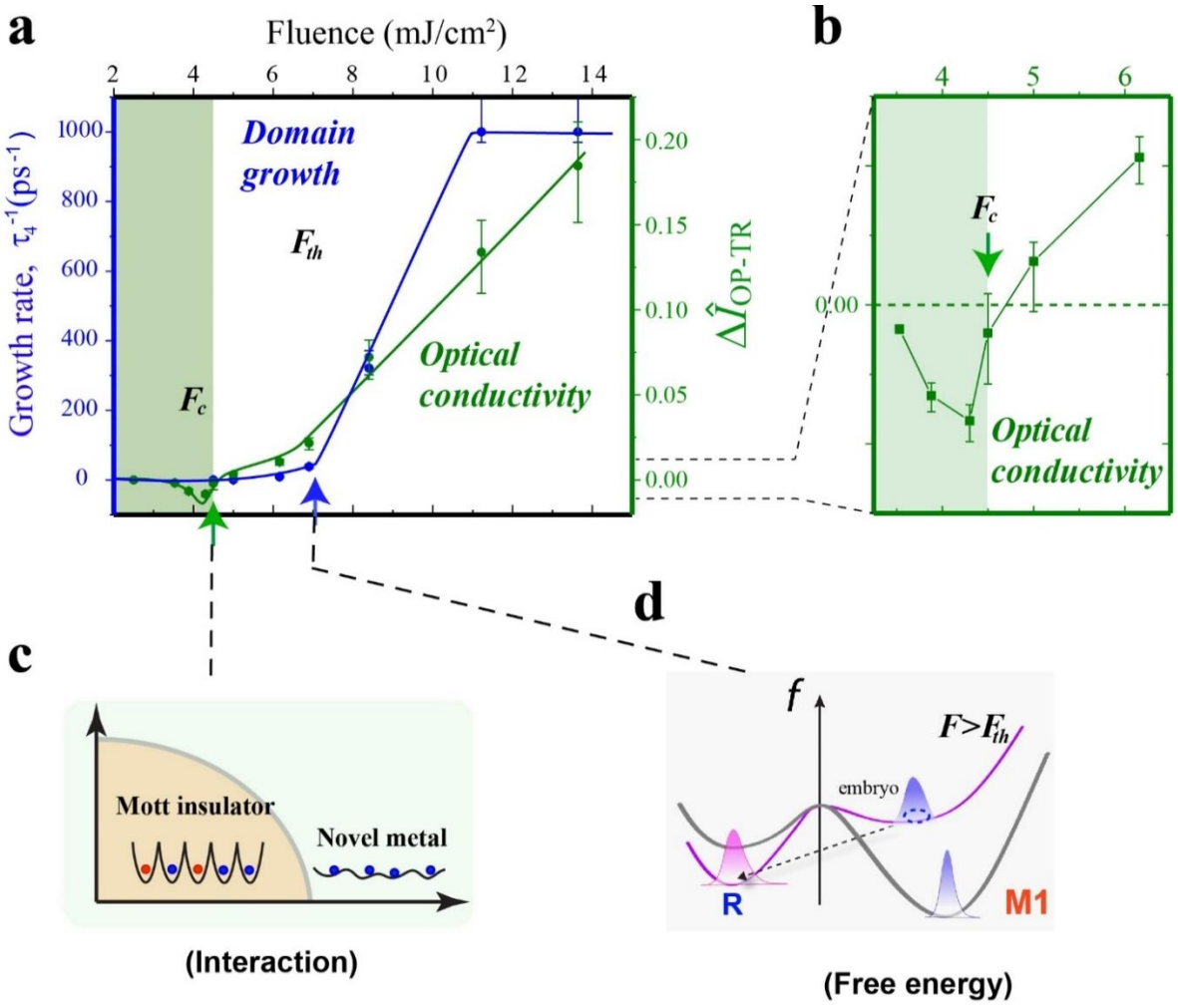

Figure 6.12. Dynamical responses accentuate the two thresholds underpinning the VO_2 phase transition. a. Data from the early-stage ac conductivity identify the insulator-to-metal switching at the critical point $F_c \approx 4.5$ mJ/cm^2. Meanwhile, the significant pick-up in the rate of domain growth speed near $F_{th} \approx 7$ mJ/cm^2 accentuates a different organizing principle becomes more active in the thermodynamical regime of transformation. Panel **b** gives an enlarged view of the ac conductivity change near F_c. **c**. Interaction-driven dynamics at short time indicated by the switching behavior near F_c. **d**. The thermal equilibrium cooperative phase transition and longtime dynamics in PIPT is governed by the change in free energy.

subscribed to the thermal R state. The conclusion that precludes the Peierls origin is consistent with the strong *d*-electron-phonon coupling being nonessential for establishing F_c, argued based on its non-subjectivity to the strain effect. That said, the strong d-band electron-phonon coupling should be behind the creation of polaron upon photo-doping. Yet, it may be instrumental to point out that small polaron localizes at the atomic site with strong lattice distortion is frequently identified in transition-metal oxide (TMO)[30], whereas a large polaron spreads over many lattice sites as evidenced here could be signature of a relatively weakly localized hole in metallic VO_2[31]. The phase-dependence in the polaron mass and transport properties is an interesting consequence of the phase transition rather than the cause for it.

Turning to the subject of how a photo-doped system eventually gains itineracy and becomes a thermal state, we examine how the transformation into the metallic puddle occurs around F_{th},. Fig. 6.12a presents the results in terms of the nucleation velocity characterized by the inverse time $1/\tau_4$ or the diffusion constant; see Sec. 6.3. In this regime, as we expect the transition to follow the dynamical route of 1st-order phase transition, the relevant timescale is regulated by the nucleation barrier. In this case, set by the local interfacial strain energy, the thermal fluctuations play a role in renormalizing the local free-energy landscape. It is expected that at F_{th}, the optical excitation quenches the thermodynamic free energy landscape into favoring R phase, in which the insulating ground state is temporally retained as a false ground state separated from the new global minimum as depicted in Fig. 6.12d. The nucleation barrier deters the embryonic metallic puddles from growing into a larger domain, but a higher level of excitation will facilitate the system to obtain a critical domain size and gain speed on nucleating the metallic puddles into larger and larger domains, fulfilling the thermodynamic cooperative phase transition over the entire grain. In this regime, the metallic state entropy gain plays a key role in lowering the free energy. It is thus

reasonable to assume that the thermodynamic force active at the large scale can overwhelm the local interaction mediated IMT and take over as the main driving mechanism in the thermodynamic regime.

6.5. Summary

Summing up, our dual-probe setup via the combination of ultrafast optical transmittance and UED provides an informative platform for critically evaluating the physics behind perplexing nonequilibrium many-body phenomenology behind photo-induced phase transition. Specifically in our studies of VO_2 phase transition, the rich correlated datasets paint a picture of a multiple-pronged process with the underlying physics evolving with the increased spatiotemporal scales of the active systems. The multi-message results allow us to develop new insight for addressing the open questions raised in recent ultrafast measurements.

First of all, concerning the cooperativity, or its lack thereof in PIPT, we have demonstrated the late-stage PIPT evolution not only is driven by the near-infrared excitation is tightly integrated with the thermally induced phase transition, but also shares the same sensitivity to the lattice strain and is governed by the same cooperativity as one uses to describe the thermal phases of VO_2. The thermal phenomenology of PIPT at the late stage is well calibrated against the joule heating mechanism by way of the dual-control effective medium theory. It is in the shared high sensitivity to the lattice strain effect in IMT and SPT where we see the role of Peierls physics and strong d-electron-phonon coupling as crucial. A key piece of information that supports this is the system universally converges back to the thermal phases and regaining the sharp first-order nature of the transition at the late stage irrespective of the early state nonequilibrium evolution that may in duce

a different path for IMT. As results show, thermal fluctuations act as a unifier to drive the system back to the familiar thermal phases no matter where the nonequilibrium system started from.

However, at the same time, the results unfold at the short time scales reveal an entirely different organizing principle. Not only the nonequilibrium phenomenology itself show no dependence on the local strain profile, but the dynamics are also ubiquitous under a new control parameter around a new critical point that is Mott transition in nature, substantially below the threshold identified for thermally mediated transition. Most intriguingly, we can link the new ultrafast photo-excited metallic state to the long thought-after monoclinic metallic state, primarily based on its retention of monoclinic crystalline motif long after the transition. The more striking result lies in its unique manifestation of unpaired V-V sublattice and yet fully retaining the zigzag features. Meanwhile, we eliminated the possibility of the existence of a long-lasting metallic monoclinic phase across a broad range of fluences. In the long-time limit (i.e., $t > 300$ ps), the IMT and SPT always happen together.

REFERENCES

REFERENCES

[1] V.R. Morrison, R.P. Chatelain, K.L. Tiwari, A. Hendaoui, A. Bruhács, M. Chaker, and B.J. Siwick, "A photoinduced metal-like phase of monoclinic VO_2 revealed by ultrafast electron diffraction," Science (1979) **346**(6208), 445–448 (2014).

[2] M.R. Otto, L.P. René de Cotret, D.A. Valverde-Chavez, K.L. Tiwari, N. Émond, M. Chaker, D.G. Cooke, and B.J. Siwick, "How optical excitation controls the structure and properties of vanadium dioxide," Proceedings of the National Academy of Sciences **116**(2), 450–455 (2019).

[3] L. Vidas, D. Schick, E. Martínez, D. Perez-Salinas, A. Ramos-Álvarez, S. Cichy, S. Batlle-Porro, A.S. Johnson, K.A. Hallman, and R.F. Haglund Jr, "Does VO_2 Host a Transient Monoclinic Metallic Phase?," Phys Rev X **10**(3), 031047 (2020).

[4] C. Xu, C. Jin, Z. Chen, Q. Lu, Y. Cheng, B. Zhang, F. Qi, J. Chen, X. Yin, and G. Wang, "Transient dynamics of the phase transition in VO_2 revealed by mega-electron-volt ultrafast electron diffraction," Nat Commun **14**(1), 1265 (2023).

[5] C. Chen, R. Wang, L. Shang, and C. Guo, "Gate-field-induced phase transitions in VO_2: Monoclinic metal phase separation and switchable infrared reflections," Appl Phys Lett **93**(17), (2008).

[6] Z. Tao, T.-R.T. Han, S.D. Mahanti, P.M. Duxbury, F. Yuan, C.-Y. Ruan, K. Wang, and J. Wu, "Decoupling of structural and electronic phase transitions in VO_2," Phys Rev Lett **109**(16), 166406 (2012).

[7] W.-P. Hsieh, M. Trigo, D.A. Reis, G. Andrea Artioli, L. Malavasi, and W.L. Mao, "Evidence for photo-induced monoclinic metallic VO_2 under high pressure," Appl Phys Lett **104**(2), (2014).

[8] J. Laverock, V. Jovic, A.A. Zakharov, Y.R. Niu, S. Kittiwatanakul, B. Westhenry, J.W. Lu, S.A. Wolf, and K.E. Smith, "Observation of Weakened V—V Dimers in the Monoclinic Metallic Phase of Strained VO_2," Phys Rev Lett **121**(25), 256403 (2018).

[9] A. Sood, X. Shen, Y. Shi, S. Kumar, S.J. Park, M. Zajac, Y. Sun, L.-Q. Chen, S. Ramanathan, and X. Wang, "Universal phase dynamics in VO_2 switches revealed by ultrafast operando diffraction," Science (1979) **373**(6552), 352–355 (2021).

[10] P. Baum, D.-S. Yang, and A.H. Zewail, "4D visualization of transitional structures in phase transformations by electron diffraction," Science (1979) **318**(5851), 788–792 (2007).

[11] J. Li, L. Wu, S. Yang, X. Jin, W. Wang, J. Tao, L. Boatner, M. Babzien, M. Fedurin, and M. Palmer, "Direct Detection of VV Atom Dimerization and Rotation Dynamic Pathways upon Ultrafast Photoexcitation in VO_2," Phys Rev X **12**(2), 021032 (2022).

[12] T.L. Cocker, L. V Titova, S. Fourmaux, G. Holloway, H.-C. Bandulet, D. Brassard, J.-C. Kieffer, M.A. El Khakani, and F.A. Hegmann, "Phase diagram of the ultrafast photoinduced insulator-metal transition in vanadium dioxide," Phys Rev B **85**(15), 155120 (2012).

[13] Z. Tao, F. Zhou, T.-R.T. Han, D. Torres, T. Wang, N. Sepulveda, K. Chang, M. Young, R.R. Lunt, and C.-Y. Ruan, "The nature of photoinduced phase transition and metastable states in vanadium dioxide," Sci Rep **6**(1), 38514 (2016).

[14] A.S. Johnson, D. Perez-Salinas, K.M. Siddiqui, S. Kim, S. Choi, K. Volckaert, P.E. Majchrzak, S. Ulstrup, N. Agarwal, and K. Hallman, "Ultrafast X-ray imaging of the light-induced phase transition in VO_2," Nat Phys **19**(2), 215–220 (2023).

[15] S. Wall, S. Yang, L. Vidas, M. Chollet, J.M. Glownia, M. Kozina, T. Katayama, T. Henighan, M. Jiang, and T.A. Miller, "Ultrafast disordering of vanadium dimers in photoexcited VO_2," Science (1979) **362**(6414), 572–576 (2018).

[16] G.A. de la Peña Muñoz, A.A. Correa, S. Yang, O. Delaire, Y. Huang, A.S. Johnson, T. Katayama, V. Krapivin, E. Pastor, and D.A. Reis, "Ultrafast lattice disordering can be accelerated by electronic collisional forces," Nat Phys **19**(10), 1489–1494 (2023).

[17] S. Wall, D. Wegkamp, L. Foglia, K. Appavoo, J. Nag, R.F. Haglund Jr, J. Stähler, and M. Wolf, "Ultrafast changes in lattice symmetry probed by coherent phonons," Nat Commun **3**(1), 721 (2012).

[18] C. Giannetti, M. Capone, D. Fausti, M. Fabrizio, F. Parmigiani, and D. Mihailovic, "Ultrafast optical spectroscopy of strongly correlated materials and high-temperature superconductors: a non-equilibrium approach," Adv Phys **65**(2), 58–238 (2016).

[19] R.D. Averitt, and A.J. Taylor, "Ultrafast optical and far-infrared quasiparticle dynamics in correlated electron materials," Journal of Physics: Condensed Matter **14**(50), R1357 (2002).

[20] H.W. Verleur, A.S. Barker Jr, and C.N. Berglund, "Optical properties of VO_2 between 0.25 and 5 eV," Physical Review **172**(3), 788 (1968).

[21] C. Lamsal, and N.M. Ravindra, "Optical properties of vanadium oxides-an analysis," J Mater Sci **48**, 6341–6351 (2013).

[22] S. Wall, L. Foglia, D. Wegkamp, K. Appavoo, J. Nag, R.F. Haglund Jr, J. Stähler, and M. Wolf, "Tracking the evolution of electronic and structural properties of VO_2 during the ultrafast photoinduced insulator-metal transition," Phys Rev B **87**(11), 115126 (2013).

[23] X.-Q. Li, and Y. Arakawa, "Anharmonic decay of confined optical phonons in quantum dots," Phys Rev B **57**(19), 12285 (1998).

[24] K.A. Hallman, K.J. Miller, A. Baydin, S.M. Weiss, and R.F. Haglund, "Sub-picosecond response time of a hybrid VO_2: silicon waveguide at 1550 nm," Adv Opt Mater **9**(4), 2001721 (2021).

[25] K. Liu, S. Lee, S. Yang, O. Delaire, and J. Wu, "Recent progresses on physics and applications of vanadium dioxide," Materials Today **21**(8), 875–896 (2018).

[26] U.C. Täuber, *Critical Dynamics: A Field Theory Approach to Equilibrium and Non-Equilibrium Scaling Behavior* (Cambridge University Press, 2014).

[27] J.M. Longo, P. Kierkegaard, C.J. Ballhausen, U. Ragnarsson, S.E. Rasmussen, E. Sunde, and N.A. Sørensen, "A refinement of the structure of VO2," Acta Chem. Scand **24**(2), 420–426 (1970).

[28] D.B. McWhan, M. Marezio, J.P. Remeika, and P.D. Dernier, "X-ray diffraction study of metallic VO_2," Phys Rev B **10**(2), 490 (1974).

[29] J.-P. Pouget, "Basic aspects of the metal–insulator transition in vanadium dioxide VO_2: a critical review," C R Phys **22**(1), 37–87 (2021).

[30] Z. Yang, C. Ko, and S. Ramanathan, "Oxide electronics utilizing ultrafast metal-insulator transitions," Annu Rev Mater Res **41**, 337–367 (2011).

[31] K.E. Kweon, and G.S. Hwang, "Structural phase-dependent hole localization and transport in bismuth vanadate," Phys Rev B **87**(20), 205202 (2013).

Appendix A. Structure Determination

The diffraction data tracks the structural changes of the sample. The intensity I of a Bragg spot (hkl), which is proportional to the square of the structure factor $F(hkl)$, is determined by the position (xyz) of all atoms within the unit cell:

$$F(hkl) = \sum_j f_j \exp[-2\pi i * (hkl) \cdot (xyz)], \quad \text{(A.1)}$$

$$I(hkl) \propto |F(hkl)|^2, \quad \text{(A.2)}$$

where f_j is the atomic scattering factor. In the M1 structure, the dimerization of V-V pairs doubles the unit cell and creates a superstructure that does not exist in the rutile structure. This is indicated in the diffraction pattern by the presence of extra diffraction peaks that track these superstructures. To account for all the observed diffraction peaks, the individual atom positions for both M1 and R structures are given in fractional coordinates in the M1 unit cell in Table A.1, where the atomic positions of the rutile structure are converted into coordinates based on the M1 unit cell. It should be noted that the conventional R unit cell only contains half of the atoms shown in Table A.1; the extras are provided for direct comparison with the M1 structure.

The diffraction intensity is then can be written as:

$$I(khl) \propto |F(hkl)|^2 \propto \left|f_V \cos\left(2\pi * (hx + ky + lz)\right) + 2f_O \cos\left(2\pi * (hx + ky + lz)\right)\right|^2 \quad \text{(A.3)}$$

where the imaginary part of the structure factor is cancelled out due to the inversion symmetry.

From Eq. A.1 and A.3, it is evident that any change in the atomic position, regardless of the manner, will result in a change in the diffraction pattern intensity in the case of PIPT. However, it is important to note that if the change in atomic positions breaks the P21/c space group symmetry for the M1 structure, additional diffraction peaks will appear(in the case the new space group have a lower symmetry) or some of the existing peak will disappear(for the case of a higher symmetry

	M1 Structure			R Structure		
	x	y	z	x	y	z
V	**0.23947**	**0.97894**	**0.02646**	0.25	1	0
V	0.76053	0.47894	0.47354	0.75	0.5	0.5
V	0.76053	0.02106	0.97354	0.75	0	1
V	0.23947	0.52106	0.52646	0.25	0.5	0.5
O-1	**0.10616**	**0.21185**	**0.20859**	0.1	0.2	0.2
O-1	0.89384	0.78815	0.79141	0.9	0.8	0.8
O-1	0.10616	0.28815	0.70859	0.1	0.3	0.7
O-1	0.89384	0.71185	0.29141	0.9	0.7	0.3
O-2	**0.40051**	**0.70258**	**0.29884**	0.4	0.7	0.3
O-2	0.59949	0.20258	0.20116	0.6	0.2	0.2
O-2	0.40051	0.79742	0.79884	0.4	0.8	0.8
O-2	0.59949	0.29742	0.70116	0.6	0.3	0.7

Table A.1 Atomic coordinates of the monoclinic M1 and rutile R phase. The atom position in the highlighted in bold is used to calculate the structure factor of M1 phase VO_2.

space group). This phenomenon has not yet been discovered. Thus, in the PIPT process, the change in diffraction intensity from atomic movements that maintain the P21/c space group is given by:

$$\frac{\Delta I(hkl)}{I(hkl)} \propto f_V \tan\left(2\pi * (hx_0 + ky_0 + lz_0)\right) * (h\Delta x + k\Delta y + l\Delta z)$$

$$+ f_{O-1} \tan\left(2\pi * (hx_1 + ky_1 + lz_1)\right) * (0.3837 * h\Delta x + 0.5627 * k\Delta y + 0.3246 * l\Delta z) \quad \text{(A.4)}$$

$$+ f_{O-2} \tan\left(2\pi * (hx_2 + ky_2 + lz_2)\right) * (0.0484 * h\Delta x + 0.1225 k\Delta y + 0.0438 l\Delta z),$$

where the initial positions can be found in the highlighted part of Table A.1. In PIPT, the absorption of laser energy will increase the random movement of atoms, which is known as the Debye-Waller effect. It has been shown that the Debye-Waller effect on diffraction intensity change is two orders of magnitude smaller compared to the change induced by the atomic position change and is thus ignored in our calculations.

Equation A.4 provides the formula for diffraction intensity change for any given diffraction peak. The unit cell size change, on the other hand, is determined by the diffraction peak position change. In thermal equilibrium, the M1 structure has (a_{M1}, b_{M1}, c_{M1}) = (5.752, 4.526, 5.383) Å and angle between a_{M1} and c_{M1} = 122.62 degrees. However, given the actual adjustment of the lattice during phase transition is not major we can map this M1 structure's unit cell to the orthogonal R unit cell. In that case, we have $(a_R, b_R, c_R)^{M1}$ = (4.526, 4.533, 2.692) Å in comparison to the R structure, which has $(a_R, b_R, c_R)^{R}$ = (4.554, 4.554, 2.851) Å. Here, the superscript indicates the structure of the system, and the subscript denotes the choice of unit cell basis. The lattice plane distance is then given by:

$$d(hkl)^R = \left(\frac{h}{a^2} + \frac{k}{b^2} + \frac{l}{c^2}\right)^R \quad \text{(A.5)}$$

The diffraction data can be understood from Eq. A.4 and A.5 to track both the local distortion and the global unit cell change.

The vanadium and oxygen atoms' coordinates used to simulate the diffraction pattern are chosen based on two constraints: 1) The oxygen atoms move along with the vanadium atoms. 2) The distortion along b_{M1} and c_{M1} is the same. These two constraints allow us to preserve the P21/c space group symmetry.

The fractional coordinates of the M1 state VO_2 in Table A.1 can be rewritten as in Table A2, where the remaining atoms' locations are set to maintain the P21/c symmetry. In this case, the regular M1 state has $\alpha = \beta = 1$, and the regular R structure (without considering the change in unit cell size) has $\alpha = \beta = 0$. For the case where VO_2 undergoes full de-twisting yet the dimerization length remains the same, we have $\alpha = 2.26852$ and $\beta = 0$. On the other hand, the case of fully de-dimerized VO_2 with the twisting angle maintained gives $\alpha = -1.26852$ and $\beta = 1$.

	a_{M1}	b_{M1}	c_{M1}
V	*0.25 - α*0.01053*	*1 - β*0.02106*	*β*0.02646*
O1	*0.1 + α*0.00616*	*0.2 + β*0.01185*	*0.2 + β*0.00859*
O2	*0.4 + α*0.00051*	*0.7 + β*0.00285*	*0.3 + β*-0.00116*

Table A.2. Fractional coordinates of M1 state VO_2

The values for α and β at a given twisting angle and dimerization length can be calculated via simple trigonometry. A 6 x 6 map for the diffraction pattern is simulated for different twisting angles and dimerization lengths, as shown in Figure 6.2 in the main text. It can be seen that a clear one-to-one relationship exists, which allows mapping the diffraction intensity into the structural order parameter. Incidentally, the robustness of our simulation is seen in the correct prediction of the (012) peak intensity increases to 153% (κ value in Fig. 6.2) at phase transition.

The unit cell size change can be calculated via any three peak position changes using Eq. A.5. Here, we choose to use peaks $(110)_R$, $(01\bar{1})_R$ and $(00\bar{2})_R$ to calculate the unit cell size change. These three peaks are chosen due to their isolation from other peaks, and there are no other peaks with any significant contribution within the *s* range of these three peaks.

Appendix B. Dual Probe Measured Dynamics Across Broad Fluence

The simultaneously measured dynamics for $\Delta\hat{I}(012)_{M1}$, $\Delta\hat{I}(30\bar{2})_{M1}$, and the optical differential transmittance are plotted in Fig. A2.1. At the late time, for all fluences at $F > F_c$, the same ratio used in Fig. 6.8 can be employed to match the amplitude. At this stage, the phase transition has progressed into the cooperative region, and the remaining dynamics involve only the metallic domain growth; thus, the amplitude change is solely determined by the volume fraction $\alpha_{M1\rightarrow R}$. For $F < F_c$, the optical differential transmittance decreases after laser excitation, indicating a reduction in metallicity. From a structure perspective, $\Delta\hat{I}(30\bar{2})_{M1}$ has small value, yet $\Delta\hat{I}(012)_{M1}$ is 0. This suggests the long-time structural change below F_c is primarily concentrated along the c_R axis.

At the short time, for all fluences at $F > F_c$, a different ratio is required to match the change between $\Delta\hat{I}(012)_{M1}$, $\Delta\hat{I}(30\bar{2})_{M1}$, and the optical differential transmittance, which is attributed to the co-existence of hot carrier and polaron dynamics in the system. At F = 13.64 mJ/cm^2, the three dynamics converge into the same curve much faster than at other fluences, which is due to the excessive thermal energy accelerating the metallic domain growth.

$F = F_c$ = 4.5 mJ/cm^2 represents a special case where the behavior is a mixture of the dynamics both below and above F_c. This is most evident from the response of the optical

differential transmittance dynamic, where at t = 10ps, the differential optical transmittance is below 0, yet at t > 100ps, there is a rise in differential optical transmittance indicating a growth in the metallic domain. This is likely due to the fluence being too close to the F_c, where the fluctuation of laser causes dynamics above and below the critical fluence mixed together.

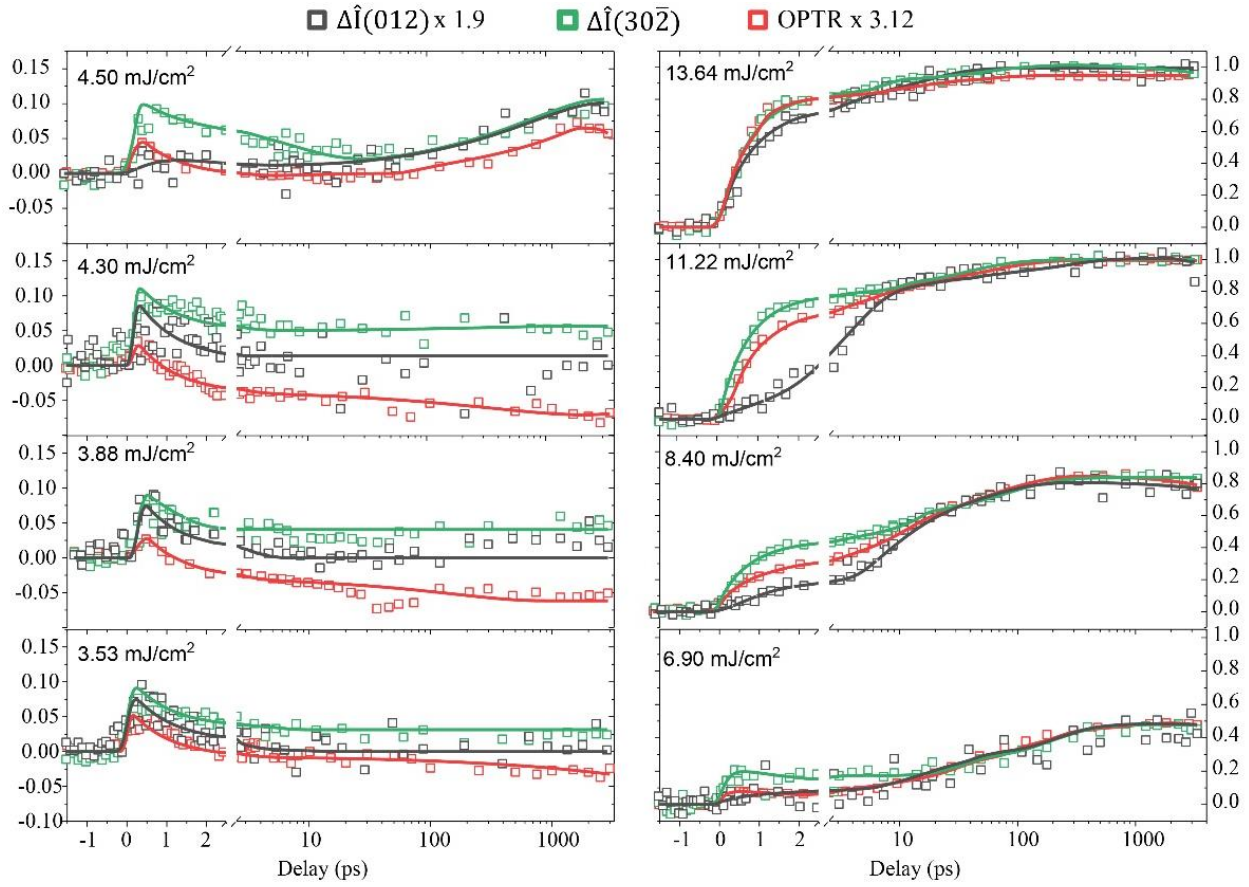

Figure B.1 Dynamics at different fluence.

Chapter 7: Summary

In this dissertation, I have presented my research on instrument development and the applications of ultrafast optical and structural probes to investigate the photoinduced phase transitions (PIPT) in strongly correlated materials, with a particular focus on VO_2.Whereas ultrafast electron diffraction and microscopy techniques have been under active development in this laboratory for many years, my participation to the on-going projects geared towards enabling multi-messenger probes. In this regard, I have developed the dual-probe system, uniting the ultrafast electron scattering and ultrafast optical techniques under the existing generation-I ultrafast electron microscope platform. This technical development is discussed in Chapter 3 and Chapter 4 of the thesis, involving setting up the new optical beamline and more importantly in better tuning the RF optics system such that the dual-probe system can achieve the same temporal resolution to make the correlated investigation more relevant. In Chapter 4, I gave a detailed account of the RF technology to achieve that. In particular, the merit of the phase space manipulation under a precision-controlled RF optical system is presented, By implementing a cascade RF control scheme with a two-level PID feedback system, we significantly reduced timing jitter and phase noise. The master feedback loop, PID-0, compensates for long-term phase drift over the entire RF circuit, while the nested loop, PID-1, suppresses high frequency noise using a digital phase-locked loop. This synergistic design reduced the integrated RMS phase noise to 0.0053°, enabling a temporal resolution of ~50 fs while maintaining high beam brightness. Experiments on 1T-$TaSe_2$ validated the improved performance, revealing coherent phonon dynamics with a signal-to-noise ratio sufficient to discern multiple-order oscillations and resolve subtle structural changes at 10 fm length scales.

In Chapter 5 and Chapter 6, I presented my scientific inquiries into the photoinduced phase transition of VO_2 applying the newly developed dual-probe system and the upgraded high-precision RF controller. In Chapter 5, I provided an overview of the physics behind the IMT and SPT in VO_2, focusing on the equilibrium state evolutions I introduced an effective medium theory to isolate specimen temperature, pump repetition rate, and strain effects at the late stage of PIPT measurements. By applying this framework to our experimental data, we demonstrated the cooperativity between IMT and SPT to be maintained even for PIPT at long times, tracing its root to joule heating. Meanwhile, the effective medium theory successfully restored the nonequilibrium PIPT dynamics under different repetition rates by accounting for the coexisting metallic and insulating regions. Importantly, we showed that the nonequilibrium dynamics is ubiquitous across all specimen sizes, hence inviable under varying strain profile. This is in stark contrast with the thermally mediated phase transition that is strongly subject to the strain effect. The clear distinction between two types of phase transitions highlights the role of nonequilibrium physics and the evolutionary nature of PIPT phenomena.

Chapter 6 delved deeper into the nonequilibrium PIPT dynamics in VO_2 by employing the dual-probe setup. We identified three distinct dynamical channels: hot carrier relaxation, polaron formation, and metallic domain growth. By tracking the evolution of the vanadium dimer chain order parameters, we discovered a new monoclinic metallic state at the ultrafast timescale. This state is characterized by a largely developed optical conductivity increases while retaining the monoclinic unite cell motif and can be induced by photodoping above a critical fluence of ~4.5 mJ/cm^2, which is significantly below the thermodynamic phase transition threshold of ~7 mJ/cm^2. The ultrafast metallization is accompanied by the polaron formation, which reduces the pairing of vanadium dimer chains without significant changes in the basal plane. Our findings suggest the

physics driving this ultrafast IMT is distinct from the Peierls mechanism or strong electron-phonon coupling that governs the thermodynamic transition. Instead, the photodoping and Mott physics play a dominant role to bring in the unique monoclinic metallic state in the nonequilibrium regime.

The results presented in this dissertation help advance both the instrumentation for ultrafast electron scattering and the fundamental understanding of nonequilibrium phase transitions in strongly correlated materials. The discovery of the photoinduced monoclinic metallic state in VO_2 highlights the power of the dual-probe approach to illustrate the structural identify of the hidden states of matter that are not accessible under equilibrium conditions. The improved spatiotemporal resolution and the methodology developed here should open new avenues for investigating the ultrafast dynamics in a wide range of quantum materials exhibiting exotic phase transitions.